Nonlinear effects of exciton polaritons applied in neuromorphic networks

Rafał Mirek

Institute of Experimental Physics

Faculty of Physics

University of Warsaw

Supervised by
dr hab. Barbara Piętka, prof. UW

Warsaw, 2022

Abstract

Neuromorphic networks are increasingly applied in all areas that require work with large amounts of data. In recent years, optical neural networks have been intensively developed as they can potentially replace their electronic counterparts, thanks to better energy efficiency and higher speed. Photonic systems are excellent for data transmission, but they possess weak interactions, which directly translates into high energy costs for creating nonlinear operations. Exciton polaritons, as particles having a low effective mass and strong nonlinear interactions, are an ideal platform for creating neural networks.

The subject of this dissertation is the nonlinear effects observed in exciton polaritons, investigated for their use in artificial neural networks. The main goal was to use the observed nonlinearities to create a neural network. As part of the work, semimagnetic exciton polaritons with unique magnetic properties observed in a magnetic field were examined spectroscopically.

The work focuses on nonlinear spin effects enhanced in the polariton condensate. The occupation of spin states below and above the condensation threshold in the external magnetic field was investigated. The possibilities of controlling the spin polarization of condensate by means of an external field and an excitation laser were discussed. The obtained results allowed us to prove the existence of a synthetic magnetic field resulting from the presence of disordered photonic potential on the sample. Ultimately, it was possible to estimate the magnitude of polariton-polariton interactions in the studied system.

Then, the influence of the photonic potential was discussed. Various shapes of the potentials leading to both the localization of the polaritons and their flow were considered. Two experimental configurations consisting of two condensates in an inhomogeneous potential were used to create a nonlinear response. Moreover, it has been shown that the existence of a localizing potential can lead to a reduction of the energy needed to create a nonlinear system.

The next part is devoted to nonlinear phase effects. First, the creation and annihilation of quantum half-vortices was investigated. Their properties and stability in an external magnetic field are discussed. Next, we focus on the phase effects resulting from polariton-polariton interactions. The relative change of the polaritons phase was investigated with the changing number of particles.

A nonlinear response was also obtained using time-delayed effects. For this purpose, a feedback loop was used. In addition to obtaining nonlinear emission, the condensate lifetime was estimated, and the lower limit of the exciton reservoir lifetime was obtained.

Ultimately, two opto-electronic neural networks were created and used to recognize handwritten numbers and perform speech recognizing task. Then, a fully optical XOR logic gate of high energy efficiency based on nonlinear exciton polariton emission is presented.

Streszczenie

Sieci neuromorficzne znajdują coraz szersze zastosowanie we wszystkich dziedzinach wymagających pracy na dużej liczbie danych. W ostatnich latach intensywnie rozwijane są optyczne sieci neuronowe, które potencjalnie mogą zastąpić ich elektroniczne odpowiedniki dzięki lepszej wydajności energetycznej oraz większej prędkości. Układy fotoniczne znakomicie nadają się do transmisji danych, ale posiadają słabe oddziaływania, co sprowadza się do dużych kosztów energetycznych na stworzenie nieliniowych operacji. Polarytony ekscytonowe jako cząstki posiadające małą masę efektywną oraz silne oddziaływania nieliniowe stanowią idealną platformę do tworzenia sieci neuronowych.

Przedmiotem niniejszej rozprawy są efekty nieliniowe obserwowane w polarytonach ekscytonowych badane pod kątem wykorzystania w sztucznych sieciach neuronowych. Głównym celem było wykorzystanie obserwowanych nieliniowości do stworzenia sieci neuronowej. W ramach pracy badano spektroskopowo półmagnetyczne polarytony ekscytonowe wyróżniające się unikalnymi własnościami magnetycznymi obserwowanymi w polu magnetycznym.

W pracy skupiono się na nieliniowych efektach spinowych wzmocnionych przy udziale kondensatu polarytonowego. Sprawdzono spinowe obsadzenie stanów poniżej i powyżej progu kondensacji w zewnętrznym polu magnetycznym. Przedyskutowano możliwości kontroli polaryzacji spinowej kondensatu przy pomocy zewnętrznego pola i lasera pobudzającego. Otrzymane wyniki pozwoliły udowodnić istnienie sztucznego pola magnetycznego będącego wynikiem obecności niejednorodnego potencjału fotonicznego na próbce. Ostatecznie udało się oszacować wielkości oddziaływań polaryton-polaryton w badanym układzie.

Następnie przedyskutowano wpływ potencjału fotonicznego na emisję z pobudzanych laserem miejsc, Rozpatrzono różne kształty potencjału prowadzące zarówno do lokalizacji polarytonów jak i do ich przepływu. Wykorzystano dwie konfiguracje eksperymentalne złożone z dwóch kondensatów w niejednorodnym potencjale do stworzenia nieliniowej odpowiedzi. Ponadto pokazano, że istnienie potencjału wiążącego może prowadzić do obniżenia energii potrzebnej na stworzenie nieliniowego układu.

W kolejna część została poświęcona nieliniowym efektom fazowym. W pierwszej kolejności zbadano kreację i anihilację półwirów kwantowych. Przedyskutowano ich własności i stabilność w zewnętrznym polu magnetycznym. Następnie skupiono się na efektach fazowych wynikających z oddziaływań polaryton-polaryton. Badano względną zmianę fazy polarytonów przy zmieniającej się liczbie cząstek w układzie.

Nieliniową odpowiedź uzyskano również wykorzystując efekty opóźnione w czasie. W tym celu wykorzystano pętlę sprzężenia zwrotnego. Oprócz otrzymania nieliniowej emisji oszacowano czas życia kondensatu i uzyskano dolny limit czasu życia rezerwuaru ekscytonowego.

Ostatecznie stworzono dwie opto-elektroniczne sieci neuronowe, które wykorzystano do rozpoznawania ręcznie pisanych cyfr oraz mowy. Następnie zaprezentowano w pełni optyczną bramkę logiczną XOR opartą na nieliniowej emisji polarytonów.

Acknowledgments

During one of the faculty Christmas Eve events, I received wishes that I would never lose my joy in what I was doing. I would like to thank everyone who made this wish possible.

First of all, I would like to thank prof. Barbara Piętka, my supervisor. I cannot describe the gratitude for all that I have received over the years. You had a huge impact on my development since the first day in the laboratory at Hoża Street. The vast majority of what I have achieved is due to you. I really appreciate the long hours spent on discussions.

I would like to thank prof. Jacek Szczytko for a very clear explanation of the semimagnetic semiconductors and numerous discussions on scientific topics and more. I am constantly impressed by your drive and fascination in science. Thank you for the huge positive energy that you brought every day.

I am very grateful to prof. Michał Matuszewski and Dr. Andrzej Opala for their invaluable theoretical support. It was a pleasure to exchange so many emails with an unimaginable number of conversations and results.

I would like to thank prof. Wojciech Pacuski and Dr. Bartłomiej Seredyński for growing samples that are unique on a global scale. Some of your microcavities were so important to me that I will remember their names for the rest of my life.

I would especially like to thank Mateusz, with whom I spent the most time on this crazy journey. I hold you in highest regard for your kindness, patience, and professionalism. I will really miss working with you.

I would like to thank Kasia, Magda and Bartek for many fruitful discussions during the studies. I will always have fond memories of long discussions about physics and life in general.

I am also thankful to my friends for countless hours of patiently listening to my thoughts about solid state and polariton physics.

I would like to thank my family and friends for supporting me in my research career and taking care of me whenever possible.

Finally, I would like to thank my wife for her great support and help during all the difficult times.

Pracę dedykuję Rodzicom.
Rafał Mirek

Contents

Chapter 1

Strong light-matter coupling in semiconductor microcavities

In this chapter, we describe the basic properties of exciton polaritons and polariton condensate. The first two sections are dedicated to photons confined in semiconductor microcavities and excitons trapped in semiconductor quantum wells. We briefly discuss the properties of these two entities with an emphasis on those used in future chapters.

In the next section, we review the properties of exciton polaritons with particular attention to those derived from their building components. We show a theoretical description of this system and discuss the outcome resulting from the presented equations.

The fourth section is devoted to the semimagnetic semiconductors. We briefly explain the method of creating these materials, focus on their properties and we compare them with nonmagnetic systems.

In the last section, we consider the polariton condensate. We show a brief history of Bose-Einstein condensation and point out the differences between atomic and polariton condensates. Finally, we explain the nonequillibrity of the polariton condensate in the context of a nonresonant excitation of semiconductor heterostructures.

1.1 Photon in semiconductor microcavity

The distributed Bragg reflector (DBR) is a periodic structure consisting of two materials with different refractive indices. They are alternately arranged in layers with precisely defined refractive indices and carefully selected thicknesses. The reflective properties of such a structure result from interference of waves reflected from successive material boundaries. For each layer, the optical thickness can be defined which is the product of the refractive index and the thickness of the layer. The optical thickness of each layer is adjusted so that they are all equal and the equation (1.1) is satisfied

$$n_a L_a = n_b L_b = \frac{\lambda_0}{4}. \tag{1.1}$$

Here, n_a and n_b are the refractive indices of the layers a and b, and L_a, and L_b describe their thickness. Photons of wavelength close to λ_0 interfere constructively.

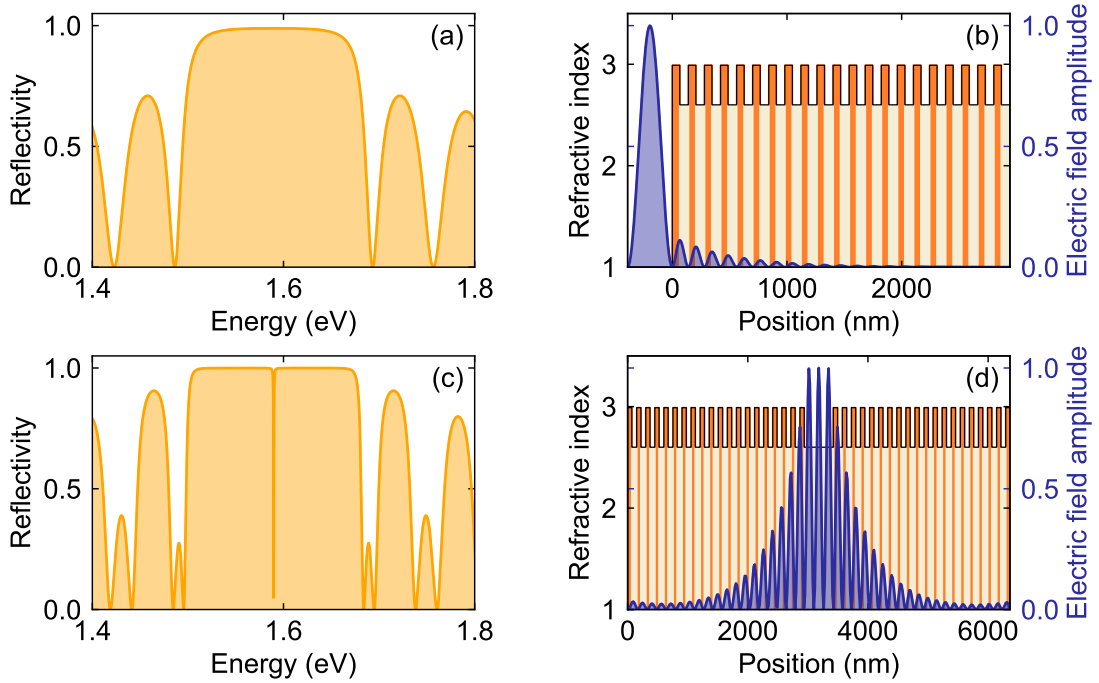

Figure 1.1: **Distributed Bragg reflector and microcavity.** Reflectivity spectrum for the (a) distributed Bragg reflector made of 21 CdTe/$Cd_{0.82}Zn_{0.08}Mg_{0.1}$Te pairs and (c) microcavity sandwiched between two distributed Bragg reflectors made of 20 CdTe/$Cd_{0.82}Zn_{0.08}Mg_{0.1}$Te pairs each. Refractive index profile and normalized electric field amplitude for a (b) distributed Bragg reflector and (d) microcavity.

This results in almost full reflection at this wavelength. The greater the number of layers and the greater the difference between the refractive index values, the greater the reflectance. Figure 1.1(a) shows the calculated reflectivity spectra for the distributed Bragg reflector made of 21 CdTe/$Cd_{0.82}Zn_{0.08}Mg_{0.1}$Te pairs at normal incidence. The structure was designed for a wavelength λ_0=780 nm. In the spectra, we observe a wide region (stop band) of high reflectance (above 99%). Outside the stop band, the reflectivity decreases and has an oscillating character with specific energies for which the light completely penetrates the structure. The width of the stop band increases with the ratio between the refractive indices (here n_a=2.99 and n_b=2.60). The profile of refractive indices in the considered structure is presented in Figure 1.1(b). The purple line corresponds to the normalized electric field amplitude of the light at λ=780 nm. Clearly, the penetration of light through the structure is very limited.

Introducing a defect layer into a distributed Bragg reflector results in the formation of a microcavity. For the thickness of the defect layer L_C given by equation (1.2) the whole structure confines photons with a wavelength λ_C/N where N is an integer.

$$L_C = \frac{N\lambda_C}{2n_C} \tag{1.2}$$

The typical reflectivity spectrum for a microcavity is presented in Figure 1.1(c). The calculations were performed for a cavity sandwiched between 20 and 20 periods and centered at λ_C = 780 nm. At this wavelength, the resonance mode of the

cavity is observed. The electric field profile [Figure 1.1(d)] shows strong confinement between the DBRs. Typical semiconductor microcavities, because of the high accuracy required, are grown using the Molecular Beam Epitaxy (MBE) technique.

The dispersion of the photon confined in a microcavity can be described as:

$$E_{ph}(\mathbf{k}) = \frac{\hbar c \mathbf{k}}{n} = \frac{\hbar c}{n}\sqrt{k_x^2 + k_y^2 + \left(\frac{2\pi}{L_C}\right)^2} = \frac{\hbar c}{n}\sqrt{k_\parallel^2 + \left(\frac{2\pi}{L_C}\right)^2}, \tag{1.3}$$

where L_C is the cavity length. Interestingly, a dispersion of a photon confined in a microcavity is parabolic because of the spatial confinement in the growth direction. For a small wave vectors equation (1.3) can be expanded in the Taylor series and written as

$$E_{ph}(k) = \frac{\hbar c}{n}\left(\frac{2\pi}{L_{cav}} + \frac{k_\parallel^2 L_{cav}}{4\pi}\right) = E_0 + \frac{\hbar^2 k_\parallel^2}{2m_{ph}^*}. \tag{1.4}$$

As a result, the photon trapped in the microcavity can be described as a particle with an effective mass m_{ph} and quadratic dispersion in the range of small wave vectors.

1.2 Quantum well exciton

The excitation of an electron from a valence band to a conduction band in a semiconductor material results in the formation of a hole in the valence band. The exciton is the bound state of the hole and the electron resulting from the Coulomb interaction between them. A structure that confines an exciton in one direction is called a quantum well. It is a thin semiconductor layer sandwiched between two barriers, i.e. semiconductors with a larger band gap. The example of a quantum well made of CdMgTe and CdTe materials is presented in Figure 1.2(a). Typically, the width of the material with the smaller band gap is 10-20 nm.

The excitons considered in the thesis are described by the Wannier-Mott model [1]. In this model, the exciton is a hydrogen-like quasiparticle in which an electron orbits around a heavier hole [Figure 1.2(b)]. The binding energy of the Wannier-Mott exciton is quite weak, typically much smaller than the thermal energy at

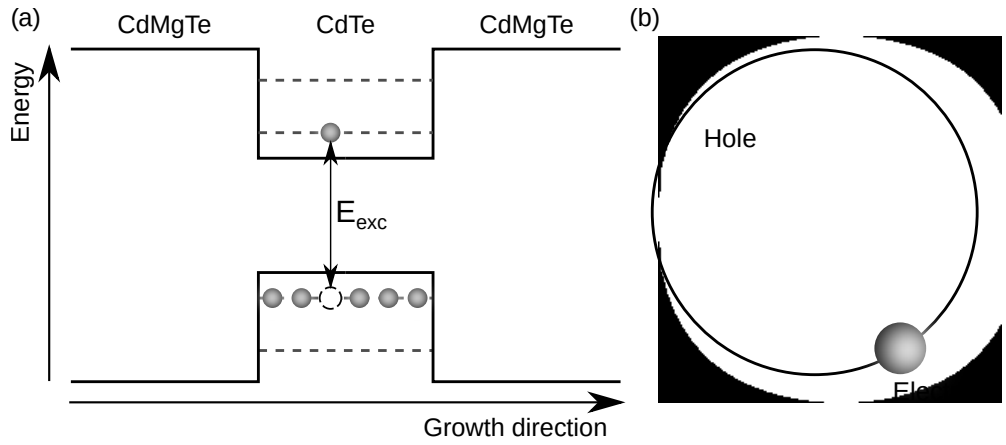

Figure 1.2: **Exciton in a quantum well.** (a) Scheme of the CdMgTe/CdTe/CdMgTe quantum well. (b) Wannier-Mott exciton as an analog of a hydrogen atom.

room temperature. The Bohr radius is about three orders of magnitude larger than the radius of the hydrogen atom. The dispersion relation of the excitons is given by

$$E_{exc}\left(\mathbf{k}\right) = E_g + E_0 + \frac{\hbar^2 \mathbf{k}^2}{2m^*}, \tag{1.5}$$

where E_g is an energy gap, E_0 is the sum of the interaction energy between the electron and the hole and the energy resulting from the limitation of exciton motion in one direction and m^* is the effective mass of the exciton related to the effective mass of the electron m_e and hole m_h:

$$m^* = m_e + m_h. \tag{1.6}$$

For excitons confined in the quantum well, the wave vector present in the dispersion relation can be decomposed into two components: k_z following the growth direction, and $k_\parallel$ parallel to the plane of the grown layers. Excitons confined in a quantum well have a parabolic dispersion in a $k_\parallel$ domain:

$$E_{exc}(\mathbf{k}_\parallel) = E_g + E_0 + \frac{\hbar^2 {\mathbf{k}_\parallel}^2}{2m^*}. \tag{1.7}$$

However, due to the large enough effective mass, in the examined range of wave vectors (up to $10\,\mu\mathrm{m}^{-1}$) there is no change in exciton energy with increasing $k_\parallel$, which allows one to approximate exciton energy in a quantum well by a constant value.

Excitons are fourfold degenerate with respect to the spin projection in the direction defined by the magnetic field. The selection rules do not allow for the coupling with light of excitons with spin projection $S_z = \pm 2$. Because of their optical inactivity, they are called dark excitons. Bright excitons with spin projection $S_z = \pm 1$ couple with photons and form polaritons with two spin projections $S_z = \pm 1$. The spin properties of polaritons are directly related to the polarization of the emitted light. States having opposite spin projections are observed in opposite circular polarizations, and their occupancy is proportional to the emission intensity.

1.3 Exciton polaritons

Inserting the quantum well into the microcavity in the anti-node of the electric field allows for the observation of the strong light-matter coupling. The interaction of excitons with photons in microcavity can be described by a system of two coupled oscillators:

$$\hat{H} = \begin{pmatrix} E_{ph} + i\hbar\gamma_{ph} & \frac{\Omega}{2} \\ \frac{\Omega}{2} & E_{exc} + i\hbar\gamma_{exc} \end{pmatrix} \tag{1.8}$$

with E_{ph} and E_{exc} describing the energy of the bare photon and exciton, γ_{ph} and γ_{exc} denoting the damping rates of the photon and exciton, and Ω representing the coupling strength.

The eigenvalues of this Hamiltonian are as follows:

$$E_{LP,UP} = \frac{E_{ph} + E_{exc} + i\hbar\left(\gamma_{ph} + \gamma_{exc}\right) \pm \sqrt{\left(E_{ph} - E_{exc}\right)^2 + \left(i\hbar\left(\gamma_{ph} - \gamma_{exc}\right)\right)^2 + (\hbar\Omega)^2}}{2} \tag{1.9}$$

The coupling strength depends in the first order on the exciton oscillator strength f_{osc}, the number of quantum wells N_{QW}, and the cavity length. If we take into account cavity and quantum well dampings, the resulting expression will also depend on γ_{exc} and γ_{ph} [2]:

$$\Omega \propto \frac{N_{QW} f_{osc}}{L_{cav}} - \frac{1}{4}\left(\gamma_{exc} - \gamma_{ph}\right)^2. \tag{1.10}$$

When the losses are negligible, the system is in a strong coupling regime [3], and the eigenstates of the considered system are exciton polaritons, which are a linear combination of exciton and photon. The dispersion relation of polaritons strongly depends on the exciton-photon detuning δ, or the energy difference between the uncoupled photon and exciton modes at the zero wave vector:

$$\delta = E_{ph}(0) - E_{exc}(0). \tag{1.11}$$

Depending on the detuning, exciton polaritons can have different photonic and excitonic components. The excitonic $\left(\left|\chi(k_\parallel)\right|^2\right)$ and photonic $\left(\left|C(k_\parallel)\right|^2\right)$ content in the polariton can be described by the Hopfield coefficients [4]:

$$\left|\chi(k_\parallel)\right|^2 = \frac{1}{2}\left(1 + \frac{E_{exc}(k_\parallel) - E_{ph}(k_\parallel)}{\sqrt{(E_{exc}(k_\parallel) - E_{ph}(k_\parallel))^2 + (\hbar\Omega)^2}}\right), \tag{1.12}$$

$$\left|C(k_\parallel)\right|^2 = \frac{1}{2}\left(1 - \frac{E_{exc}(k_\parallel) - E_{ph}(k_\parallel)}{\sqrt{(E_{exc}(k_\parallel) - E_{ph}(k_\parallel))^2 + (\hbar\Omega)^2}}\right). \tag{1.13}$$

The calculated polariton dispersion at different detunings is presented in Figure 1.3. We plot the energy for different angles of emission (θ) that are directly connected to the wave vectors following the equation:

$$k_\parallel = \frac{E_{ph}}{\hbar c}\sin\theta. \tag{1.14}$$

In each panel, the dashed lines show the energies of the uncoupled exciton and photon modes. Continuous lines correspond to energies of strongly coupled modes. For each detuning, an anticrossing of the lower and upper polariton branches is observed, which is a fundamental signature of a strong coupling. Different detunings are realized here by keeping the exciton energy constant and changing the photon energy. In practice, it is achieved by growing a quantum well in the wedged microcavity. The shape of the dispersion, and thus the properties of the polaritons, changes significantly along with detuning. At positive detuning, the lower (upper) polariton has a dispersion shape similar to that of the exciton (photon). In fact, these modes also have dominant excitonic and photonic components, respectively. With decreasing detuning, the effective mass of the lower polariton decreases. At zero detuning the photonic and excitonic content in the lower (and upper) polariton are the same at zero wave vector. With an increasing wave vector, the lower

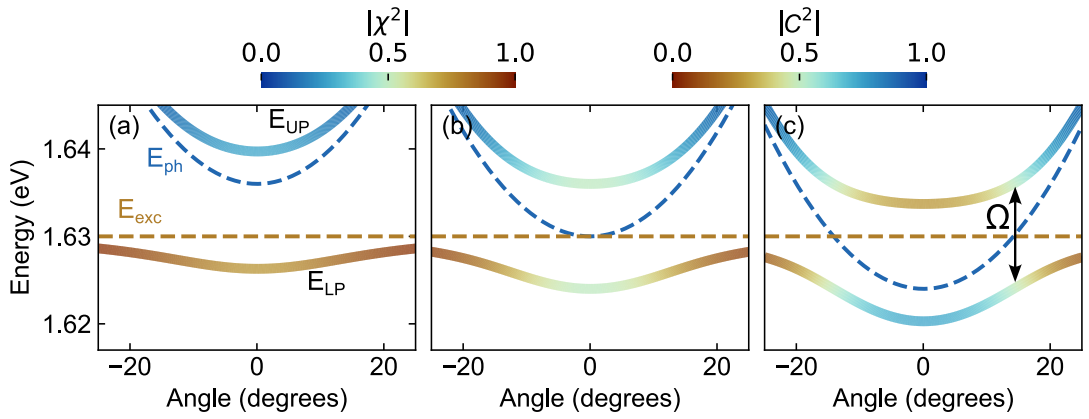

Figure 1.3: **Exciton polaritons dispersion.** Dispersion relations of exciton polaritons at (a) positive, (b) zero, (c) negative detuning as a function of angle (proportional to wave vector). Dashed lines corresponds to the bare exciton and photon energies. Colorbars show color scales describing Hopfield coefficients along the polariton branches.

polariton becomes more excitonic and the upper polariton becomes more photonic. At zero detuning, the coupling strength can be obtained from the energy difference between the lower and upper polariton at zero wave vector. At the negative detuning, the bare exciton energy crosses twice the photon energy. Again, at the wave vectors where the uncoupled modes cross, the energy difference between the lower and upper polariton defines the coupling strength. Between these two wave vectors, the photonic component is dominant in the lower polariton.

The content of a photon, or exciton, in polariton critically affects the properties. Due to the photon contribution, exciton polaritons have a very small effective mass, on the order of 10^{-4}-10^{-5} of free electron mass. Because of the excitonic component, they interact with each other and are sensitive to the external magnetic field. Another very important feature, which polaritons inherit from excitons, is the total angular momentum, which is the sum of the orbital and spin momentum of an electron and a hole.

Excitons can interact with each other in terms of Coulomb exchange [5]. To describe the exciton-exciton interactions, one has to take into account the spin of the electron ($\pm 1/2$) and the hole ($\pm 3/2$). To simplify, we consider only heavy holes. The energy of two interacting excitons depends on the kinetic energy of both exci-

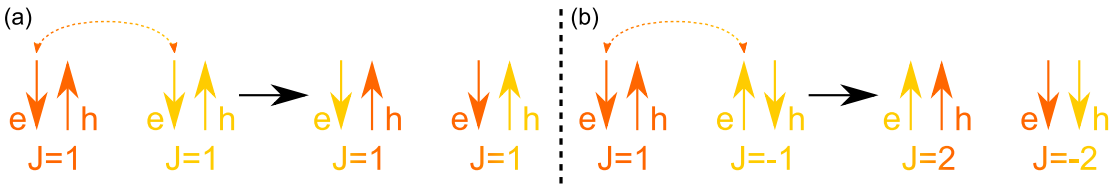

Figure 1.4: **Spin dependent exchange interactions of excitons.** Electron-electron exchange interactions between excitons with (a) parallel (b) opposite spins. Spins of the electron (e) and hole (h) belonging to the first (second) exciton before the exchange interaction are marked with the orange (yellow) color. The dashed arrows indicate the particles involved in the exchange. The black arrow signifies the transition from the state before to the state after the exchange interaction.

tons, the electron-hole exchange interaction in a single exciton, and the exchange interactions within two excitons. In the last term, one can distinguish electron-hole, electron-electron, and hole-hole exchange. The dominant contribution comes from the electron-electron and hole-hole exchange interactions. Spin-dependent interactions are presented schematically in Figure 1.4. As a result of interactions between excitons having parallel spins, we obtain two excitons with a total angular momentum (J) of 1. Note that this mechanism is true for both electron-electron and hole-hole exchange interactions. In the case of opposite spins of excitons, interactions result in the scattering to dark excitons with spin of electrons parallel to spin of holes. The presence of spin has a significant influence on polariton interactions. Polariton-polariton interactions for polaritons with parallel spins are strong and repulsive, whereas interactions between polaritons of the opposite spins are weaker and attractive [6, 7].

Polaritons have a short lifetime that ranges from a few to hundreds of picoseconds [8, 9], depending on the system. The presence of losses requires continuous pumping with an external laser. The polariton population is typically created in a nonresonant excitation depicted schematically in Figure 1.5. The energy of the laser is tuned to the first minimum on the high-energetic side of the reflectivity spectrum to maximize pumping efficiency. The laser creates free charge carriers that scatter with each other and with phonons and form an excitonic reservoir. The excitonic reservoir provides a gain for polaritons that occupy mainly the lower polariton at high wave vectors. The relaxation of the polaritons along the dispersion curve at this time is strongly dependent on the detuning. At negative detuning, the dispersion is very steep and the polariton energy changes dramatically with the wavevector. If the energy and momentum conservation principles make scattering with phonons very inefficient, polaritons accumulate in the bottleneck at high wave vectors. At positive detuning, this phenomenon does not occur and the occupation of the polariton branch is the strongest at minimum.

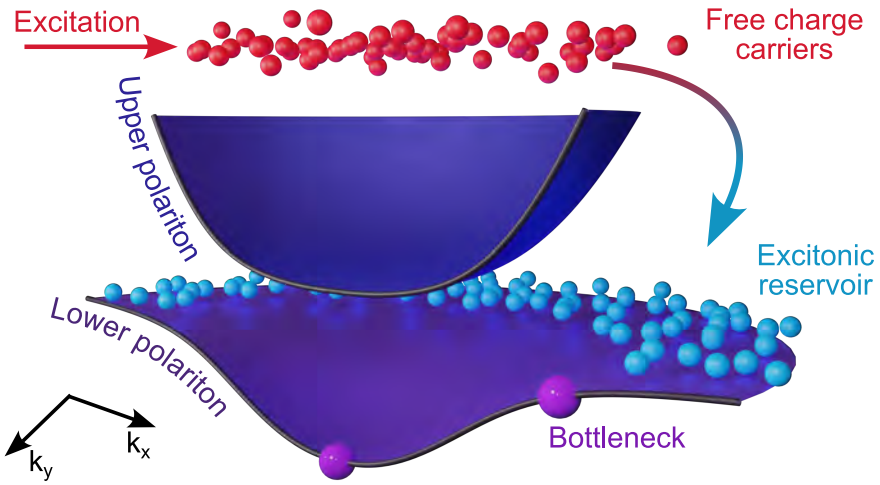

Figure 1.5: **The scheme of nonresonant excitation.** The laser initially creates free charge excitons (red balls), which scatter to lower energy states through the optical and acoustic phonons. As a result, the polariton branches (dark blue and violet curves) and the excitonic reservoir (light blue balls) are populated.

1.4 Semimagnetic semiconductors

Studies of polariton spin phenomena are richer in semimagnetic semiconductors, where the polariton spin components are pronounced in the external magnetic field. Semimagnetic semiconductors are obtained by random replacement of some cations in a semiconductor with transition metal ions having large spin. The main purpose of this procedure is to obtain a semiconductor material with strong magnetic properties. The presence of magnetic ions, even in a small amount, results in the appearance of the *s,p-d* exchange interactions. This leads to observations of phenomena such as the giant Faraday effect or the giant Zeeman effect. The history of semimagnetic semiconductors is rich and fruitful, with many successful experiments and many interesting effects. These systems are very graceful, easy to study, and reveal many interesting effects with spin in the lead. The first semiconductors with small amounts of magnetic ions in the structure have been used for studies of phonon transitions [10] and the influence of the crystalline field on the spin configuration of the transition metal ion [11, 12]. Later, the propagation of helicon waves in such structures has been investigated [13, 14]. Only measurements made in a magnetic field revealed their extraordinary properties. In narrow-gap semiconductors, giant spin splitting of Landau levels has been observed [15]. Studies of CdTe-based semiconductors revealed that *s,p-d* exchange interaction between magnetic ions and charge carriers allows for observation of magnetic effects not observed in nonmagnetic samples such as the giant Faraday effect [16, 17]. Most importantly, after the introduction of small amounts of magnetic ions, the material retains semiconductor properties such as band structure, transport properties, or magneto-optical properties [18]. In recent years, magnetic semiconductors have entered other branches of physics with impetus, appearing, among others, in quantum dots [19, 20] or placed in semiconductor microcavities [21].

In this thesis, CdTe-based semimagnetic semiconductors will be used for studies of spin-dependent interactions in exciton polaritons. In nonmagnetic samples, magnetic effects are usually subtle, difficult to detect, or hidden in linewidth. Studies of gallium arsenide based microcavities with nonmagnetic quantum wells have shown a diamagnetism as a dominant effect in an external magnetic field [22, 23] and the Zeeman splitting was comparable with the linewidth [24–27]. The use of semimagnetic semiconductors leads to the observation of completely new properties of excitonic polaritons. Strong coupling between excitons in a semimagnetic quantum well and photons results in the formation of exciton polaritons with unique spin properties in magnetic field, which will be presented in later chapters.

1.5 Nonequilibrium exciton polariton condensate

Exciton polaritons are bosonic particles that can undergo the transition to condensate. Bose-Einstein condensation (BEC) is a second-order phase transition that results in a macroscopic occupation of a single quantum state. In an ideal condensate, all particles have the same, lowest-energy state and can be described using one macroscopic wave function. Condensation was predicted in 1925 by Satyendra Nath Bose and Albert Einstein. The experimental realization of this idea was very challenging, mainly because of the very low temperature required. The first BEC

has been demonstrated 70 years later for Rubidium atoms at 170 nK. To achieve this, Doppler cooling and magnetic trapping were needed. To this day, experiments with atomic condensates are difficult to realize because of the technologies required to trap atoms and cool them to a sufficiently low temperature.

These problems can be easily overcome by using exciton polaritons, which have a very small effective mass. Condensation occurs when the de Broglie wavelength λ_{dB} of the particles is comparable to the mean distance between them. According to the equation (1.15), de Broglie wavelength increases with decreasing particle mass.

$$\lambda_{dB} = \sqrt{\frac{2\pi\hbar^2}{mk_BT}} \tag{1.15}$$

For this reason, the first exciton polariton condensate was observed at liquid helium [28] and a few years later at room temperature [29]. However, the polariton condensation mechanism is substantially different from the Bose-Einstein condensation observed in atoms. Unlike polariton systems, in an atomic physics it is more convenient to decrease the temperature than to increase the density of particles. Usually polaritons show transition to the condensate while increasing the density of these quasiparticles, which is achieved by increasing the excitation power of the laser. The polariton condensate is a nonequilibrium, driven-dissipative system, due to constant loss of particles (dissipation) and required constant replenishment (drive).

In the following chapters the properties of polariton condensate, namely nonlinear character of phase transition, nonlinear type of interactions between two condensates, both enhanced by spin effects in semimagnetic structures, will be used to construct neural network.

Chapter 2

Neuromorphic computing

Modern computers despite their tremendous performance on solving many problems have a huge problem with some tasks that are relatively easy for humans. Computers follow the von Neumann architecture, where the central processing unit (CPU) is physically separated from the memory. CPU consists of an arithmetic logic unit performing basic arithmetic operations and a control unit retrieving and processing the data from memory. Any arithmetic operation requires access to external memory, where program data and instructions are stored. This leads to a bottleneck that is especially visible when solving classification problems.

In this chapter, the importance of nonlinear data transformation is shown. We present the application of logic gates data to data classification problems. We introduce neural networks as architectures that perform efficient data classification. We consider optical neural networks as systems with the potential to operate better than electronics.

2.1 Data classification problems

Data classification problems can be divided into linearly separable and linearly inseparable. Linearly separable problem is defined as a problem that can be solved by using a linear function. In the two-dimensional plane, it can be represented graphically as two different classes that can be separated by a straight line, as in Figure 2.1(a). Here, the blue circles can be separated from the orange triangles using the linear function pictured as a red dashed line. However, there are more complex systems where a single linear function is not enough to classify the data with 100% accuracy. The linearly inseparable problem requires the use of more than one linear function to fully separate two classes. The example of a not linearly separable problem is presented in Figure 2.1(b). In this case, it is impossible to perform the linear classification with success.

Logic gates are common examples of simple classification problems for which the solution is well known. AND logic gate is an example of a linearly separable problem where a logical true and a logical false in a logic table can be distinguished through a linear function. It can be represented graphically in a two-dimensional input space as in Figure 2.2(a). Here, the blue and orange circles correspond to the low- and high-level logic output states, respectively. The exemplary linear function that separates low states from high states is marked with a red dashed line. In this case, the linear classification is performed with 100% efficiency. One

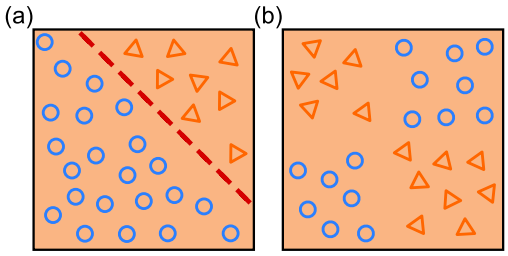

Figure 2.1: **Data classification problems.** Graphic representation of linearly (a) separable (b) inseparable problem. Blue circles and orange triangles describe two exemplary classes to be separated.

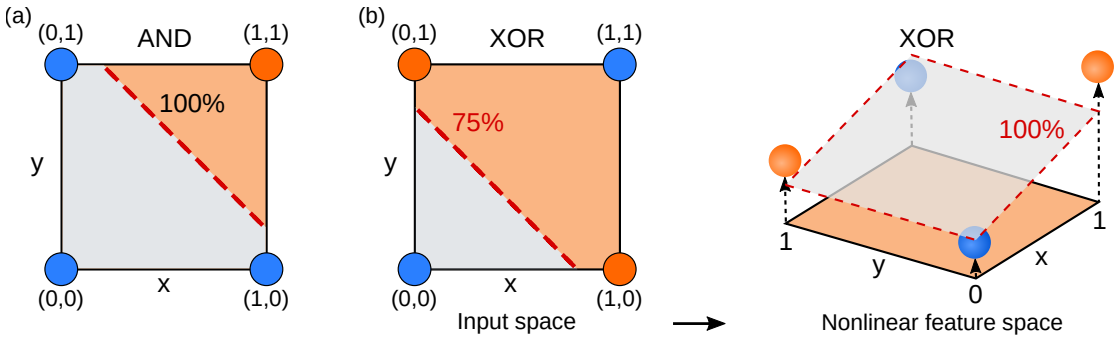

Figure 2.2: **Logic gates as a classification problems.** Implementation of a nonlinear function into XOR logic gate as a solution to data classification problem. a) Graphic representation of AND logic gate as a linearly separable problem b) Representation of XOR logic gate as a not linearly separable problem. The use of nonlinearities to separate classes in XOR logic gate. Blue and orange circles correspond to logic "0" and "1" states, respectively.

of the examples of a not linearly separable problem is an XOR gate, which in this representation has a logical true on the diagonal and a logical false on the antidiagonal elements of a logic table [Figure 2.2(b)]. Therefore, it is not possible to perform a simple linear separation of the data. The highest achievable efficiency for this task is 75%. To solve it with full efficiency, one needs to use a nonlinear function to separate the two classes, or nonlinearly transform the data before the linear classification process. The common method is to project the output into a higher-dimensional space using a nonlinear function. Then, the classification can be realized using a linear function (e.g., a plane in a three-dimensional space) that allows for discrimination of the results in an XOR gate.

2.2 Neural networks

The problem of von Neumann bottleneck does not apply to artificial neural networks that mimic the operations of biological neurons. A simplified biological neuron with the description of basic functions is illustrated in Figure 2.3(a). Neuron dendrites receive information in the form of electrical impulses. These data are weighted in synapses or connections between successive neurons. The input data are then summed and nonlinearly transformed in the nucleus. The processed data are then transferred through the axon to its terminals and then to other neurons. The mathematical model of a biological neuron [Figure 2.3(b)] referred to

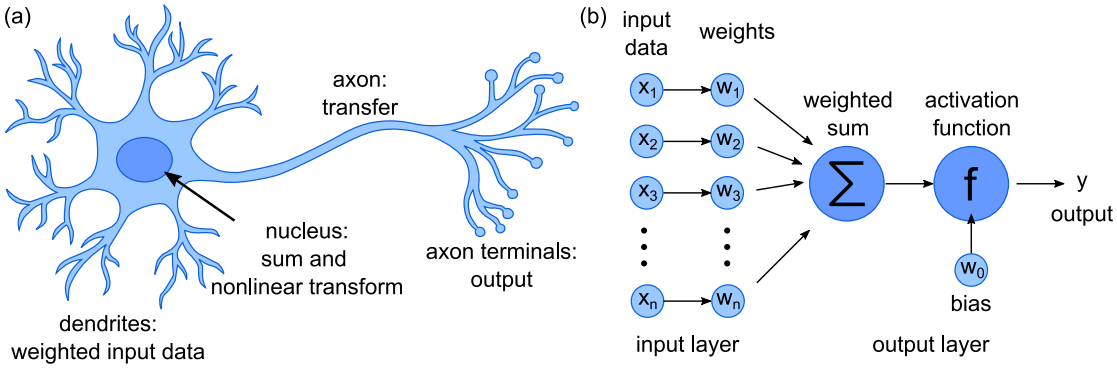

Figure 2.3: **Neuron and perceptron.** Scheme of the (a) biological and (b) artificial neuron. Input data is weighted, then summed, nonlinearly transformed and given as an output.

as a perceptron has been introduced by Walter Pitts and Warren McCulloch [30] and then modified by Frank Rosenblatt, Marvin Minsky, and Seymour Papert [31, 32]. The description of the perceptron follows the story explained for a biological neuron. The input data can be expressed as a vector $\mathbf{x}$:

$$\mathbf{x} = [1, x_1, x_2, \ldots, x_n] \tag{2.1}$$

Successive input values are assigned to the weights described in $\mathbf{w}$:

$$\mathbf{w}^{\mathrm{T}} = [w_0, w_1, w_2, \ldots, w_n]^{\mathrm{T}} \tag{2.2}$$

All weighted values are summed and given together with the bias as an argument of an activation function. Bias is an additional input value (equal to 1) with assigned weight (w_0). Its role is to modify the influence of the activation function on the input data. Activation function is a nonlinear function that transforms the input data into the output. Finally, the output of the perceptron can be expressed as in equation 2.3.

$$y = f(\mathbf{W}^{\mathrm{T}}\mathbf{x}) = f(w_0 + w_1x_1 + w_2x_2 + \ldots + w_nx_n) = f\left(w_0 + \sum_{j=1}^{n} w_jx_j\right) \tag{2.3}$$

The artificial neuron produces the output with a value that depends on whether or not the threshold has been exceeded. Thus, it can act as a linear classifier. For this purpose, a neuron must be trained to perform the classification correctly. The perceptron receives teaching data, which is a set of input data with labels that describe the classes. In the teaching process, the loss function is minimized by changing the weights. The loss function defines the difference between the output and label values and is usually given by the mean squared error (MSE) [33]:

$$MSE = \frac{1}{n}\sum_{i=1}^{n}\left(y^i - \hat{y^i}\right)^2 \tag{2.4}$$

where n is the number of teaching examples, y^i is the i-th output of the neuron, and $\hat{y^i}$ is the i-th expected value of the output.

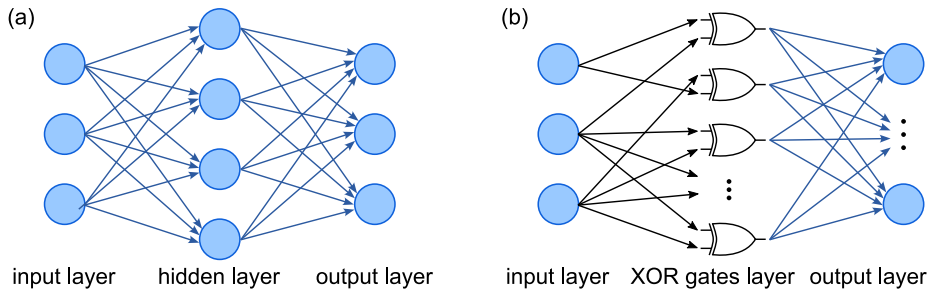

Figure 2.4: **Feed-forward neural networks.** Schemes of the (a) feed-forward (b) binarized neural network. Nodes of the network are illustrated with blue circles and connections with the arrows. The connections having weights are marked with the blue color.

It has been proven that a single perceptron can solve only linearly separable problems, such as the implementation of any linear logic gate [32]. However, it is impossible to simulate any nonlinear logic gate within a single perceptron.

This problem does not apply to artificial neural networks, which are architectures that mimic the neural networks present in biological systems. The basic scheme of the most widely used (feed-forward) neural network is presented in Figure 2.4. In this network, the input data are processed in one direction. The entire structure consists of three different layers. In the input layer, one or more nodes can be included, depending on the number of parameters that are taken into account in the model. Nodes forming a hidden layer contain activation functions that perform nonlinear transformations. It is worth mentioning that there are so-called deep neural networks that consist of more than one hidden layer in the structure. The last layer contains nodes, the number of which is equal to the number of classified classes. Layers are connected with themselves through the connections. These connections have weights that are adjusted in the teaching process. The teaching is analogous to the one presented for a perceptron. The teaching data set feeds the neural network to adjust the weights in each connection. When the weights are set, the accuracy of the network can be checked using an independent data set and comparing the predictions of the network with the labels.

Interestingly, hidden layer nodes can be replaced with logic gates. An exemplary scheme of the binarized neural network (BNN) based on XOR logic gates is presented in Figure 2.4(b). The presence of logic gates in a hidden layer has two crucial consequences. First, such a network requires the input data to be binarized. This is usually ensured by proper preparation of the input data and not using weights for connections between the input layer and the hidden layer. Second, it imposes the binary output of the hidden layer. The weights are adjusted for the connections between the hidden layer and the output layer. Again, the output layer consists of a number of nodes corresponding to the number of classes. The main advantage of the use of BNNs is a significant improvement in speed and energy efficiency [34, 35].

2.3 Optical neural networks

There is a growing need to process large amounts of data. In recent years, computing power demands have increased drastically. Over the past few years,

the computing performance has doubled every two months [36]. So far, electronic systems have fulfilled these requirements, mainly because of the continued decrease in the size of semiconductor chips. However, we are witnessing the break-down of Moore's law. The processor clock speeds are already saturated due to connections and heating problems [37]. These problems can potentially be solved by introducing photonic systems for computing. Photons are excellent medium for the communication of information and are characterized by low losses. These are the two essential properties that give the advantage of photonic systems over electronics. In recent years, optical neural networks started to compete with the electronic implementations. Recently reported optical neural networks use several different approaches, including Mach-Zehnder interferometers [38], micro-ring resonators [39, 40], diffractive deep optical networks [41, 42] or photonic recurrent neural networks [43].

However, in all the above realizations photons are interacting weakly and only in nonlinear media. In fact, nonlinear operations are the biggest issue in photonics. The main challenge of this thesis was to create a system with high efficiency of nonlinear interactions to reduce the cost of operation. For this purpose, we will show different exciton polariton systems providing large nonlinear response. These systems will be based on magnetic effects, localization phenomena and phase effects. We will show various sources of nonlinearities in exciton polariton platform and use them to create a neural network.

Chapter 3

Samples and experimental details

The Laboratory of Molecular Beam Epitaxy developed at the Faculty of Physics of University of Warsaw by Prof. Wojciech Pacuski is famous for semimagnetic structures. Microcavity samples with quantum wells containing manganese ions are particularly difficult to grow epitaxially, but this was achieved by the use of CdTe-based quaternary materials. In this thesis, we focused mainly on the semimagnetic sample (MC-S), which has been used to study the nonlinear phenomena in most experiments. To distinguish the effects caused by the presence of magnetic ions in the structure, we also used a non-magnetic sample (MC-N) with parameters similar to those of the semimagnetic sample. The third sample (MC-T) was used in experiments performed in a transmission configuration. The substrate was exfoliated from the sample using the lift-off process [44]. The detailed parameters that characterize the samples are presented in Table 3.1. The presented samples were grown using Molecular Beam Epitaxy (MBE) by Dr. Bartłomiej Seredyński and Prof. Wojciech Pacuski.

Table 3.1: Samples studied in this thesis and their basic parameters: number of top (N_{top}) and bottom (N_{bottom}) pairs creating distributed Bragg reflectors, made of material with higher n_{high} and lower n_{low} refractive index. N_{QW} corresponds to the number of quantum wells in the microcavity.

Sample	**MC-S**	**MC-N**	**MC-T**
Type	Semimagnetic	Nonmagnetic	Semimagnetic
N_{top}	16	21	20
N_{bottom}	19	22	20
n_{high} material	$Cd_{0.88}Zn_{0.03}Mg_{0.09}Te$	$Cd_{0.86}Zn_{0.04}Mg_{0.10}Te$	$Cd_{0.88}Zn_{0.04}Mg_{0.08}Te$
n_{low} material	$Cd_{0.35}Mg_{0.65}Te$	$Cd_{0.43}Mg_{0.57}Te$	$Cd_{0.52}Mg_{0.48}Te$
Cavity material	$Cd_{0.88}Zn_{0.03}Mg_{0.09}Te$	$Cd_{0.86}Zn_{0.04}Mg_{0.10}Te$	$Cd_{0.88}Zn_{0.04}Mg_{0.08}Te$
Cavity thickness	2λ/n (578.6 nm)	2λ/n (585.7 nm)	2λ/n (600 nm)
QW thickness	20 nm	20 nm	20 nm
N_{QW}	3×2	3×2	3×2
Mn content in QW	0.5%	0.0%	1.0%
Substrate	GaAs:Si (100)	GaAs:Si (100)	exfoliated

The most basic experimental setup and the basis for more complex experiments used in this thesis is presented in Figure 3.1(a). The laser was focused on a sample using the objective. The emission from the sample was collected by the same objective and directed toward a detector. The long pass filter (LP) cut the laser

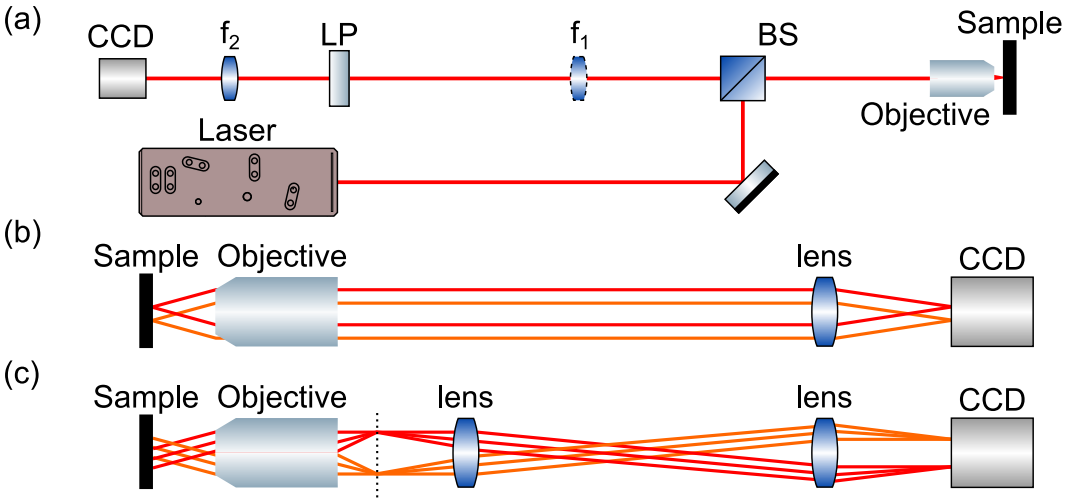

Figure 3.1: **Experimental setup for real and momentum space imaging**. (a) Scheme of the experimental setup for measuring the emission in real and momentum space. Beam splitter (BS), lenses f_1 and f_2 and long pass (LP) are marked respectively. (b) Real space imaging. Red and orange beams correspond to the light emitted from different positions on the sample. (c) Momentum space imaging. Red and orange beams correspond to the light emitted at different angles from the sample. Focal plane of the objective is marked with the dotted line.

reflected from the sample. We used lenses f_1 and f_2 to image the real (spatial) or reciprocal (momentum) space. The real space imaging is schematically presented in Figure 3.1(b). The different positions on the sample were imaged on the different positions of a CCD camera. In this imaging, the beam was collimated behind the objective. A single lens was used to focus an image on a focal plane. In the position of a focal plane, the CCD camera chip was placed.

The momentum of exciton polaritons is directly translated into the angle of light emission. For momentum space imaging, we used the experimental setup with two lenses [Figure 3.1(c)]. Here, the different angles of emission were projected on different positions on the sample. For this purpose, we placed the first lens in a distance of focal length from the focal plane of the objective. Another lens was placed a focal length before the CCD camera.

Chapter 4

Spin properties of semimagnetic exciton polaritons

In recent years, there has been growing interest in exploiting polaritons as a platform for the realization of simulators in complex structures with a well-defined photonic potential [45–49]. However, the lack of application in spin-related polaritonics comes from the limited control of polarization and, in many cases, from the need for a large external magnetic field. Studying the spin properties of exciton polaritons can be facilitated by using microcavities with semimagnetic quantum wells. Magneto-optical experiments performed on these materials have allowed the observation of giant Faraday rotation and giant Zeeman splitting in a microcavity [50–53]. Recent results show even more spectacular effects, such as polariton lasing induced by the magnetic field [54], the giant spin Meissner effect [55], and the fast build-up of condensate polarization in the external magnetic field [56]. Semimagnetic polariton condensates are a very interesting topic, which includes and distinguishes the spin in the system.

In this chapter, we study the magnetic properties of exciton polariton condensates formed in a sample MC-S containing nonmagnetic distributed Bragg reflectors with semimagnetic quantum wells [57]. Typical nonmagnetic condensates manifest linear polarization under non-resonant excitation [58, 59] which is consistent with theoretical predictions [60]. Similar behavior has been predicted [61] and achieved [56] even for semimagnetic samples. However, it is possible to obtain a nonzero circular polarization of the condensate at zero magnetic field [62–64] but this effect is stochastic and difficult to control. The highest controllable degree of circular polarization has been observed for high-quality samples as a result of engineering the confinement in the cavity [65].

We show that it is possible to create an elliptically polarized semimagnetic condensate in the absence of a magnetic field. This is due to the presence of a purely photonic, synthetic, out of plane magnetic field acting on a polariton pseudospin. This allowed us to create condensates with different spin polarizations using the same excitation laser. We discuss in detail the origin and stability of this effective magnetic field. Furthermore, we show that the initial polarization can be tuned in a full range of circular polarization by changing the magnetic field, power, energy, or polarization of the excitation laser. Finally, we estimated the strength of polariton-polariton interactions.

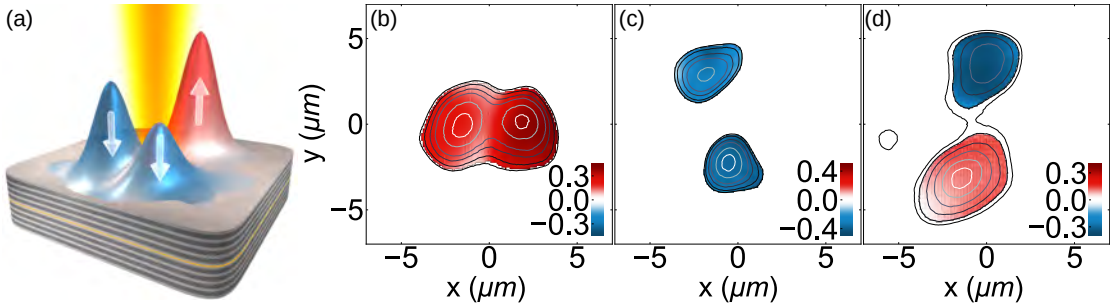

Figure 4.1: **Synthetic magnetic field acting on the spin polarization of condensates.** (a) Schematic illustration of linearly polarized laser forming three localised condensates with different spin polarisation. (b-d) Different spin arrangements of localised condensates realized on different positions on the sample. The total intensity is marked by constant intensity contours. Color scale gives information about degree of circular polarization.

4.1 Spin polarization of exciton polaritons

One of the most intriguing properties of the samples studied in this thesis is the presence of a synthetic magnetic field acting on polaritons. This effective magnetic field allows for the realization of different spin-polarized condensates summarized schematically in Figure 4.1(a). It has been previously reported that CdTe-based structures have a rich photonic potential and photonic inhomogeneities of the cavity and DBRs have been observed [66]. The nonresonant excitation with a linearly polarized laser with a spot diameter large enough to cover a few potential minima leads to the creation of elliptically polarized condensates. The dominant spin polarization is locally random and depends on the position on the sample. This allows for creating two condensates having the same or opposite spin polarization [Figure 4.1(b-d)]. All these realizations can be achieved under the same conditions at different positions on the sample. The method is not deterministic, but finding a specific position on the sample with the desirable configuration is not difficult.

The presence of photonic potential distribution leads to the localization of a condensate in a local minima. Our plan was to create condensates localized in a local potential minima with a nonzero degree of circular polarization and control their polarization using external parameters. We will start with a discussion on

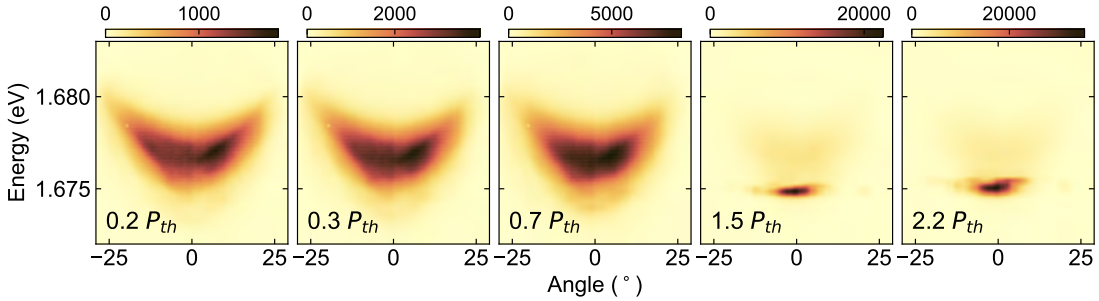

Figure 4.2: **Dispersion of lower polariton for different excitation power.** Angle-resolved photoluminescence maps of lower polariton for different excitation power. Color scale gives information about the intensity of emission. The excitation power is marked in the bottom left corner of each panel.

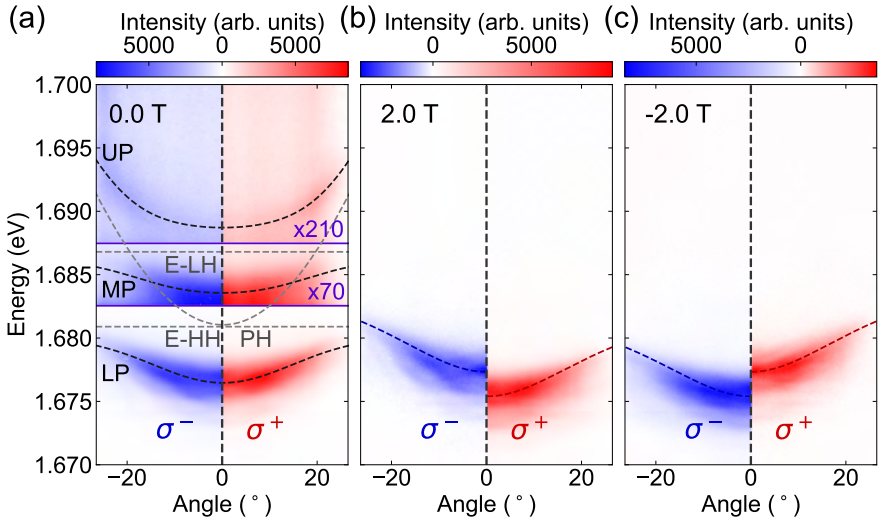

Figure 4.3: **Dispersion of semimagnetic exciton polaritons in external magnetic field below the condensation threshold.** Angle-resolved photoluminescence maps in external magnetic field below the condensation threshold. σ^- (left) and σ^+ (right) polarised emission at (a) 0 T (b) 2.0 T and (c) −2.0 T. Colorbars describe emission intensity in σ^- (in blue) and σ^+ (in red) polarization. In the absence of magnetic field polariton modes are marked with black dashed lines and exciton and photon modes are marked with grey dashed lines. The regions above the purple lines are are multiplied by indicated factors for better visibility.

the spin properties of polaritons below and above the condensation threshold.

Figure 4.2 shows the angularly resolved photoluminescence of exciton polaritons for increasing excitation powers. The maps not resolved in polarization present dispersion in the energy range of a lower polariton. For a low excitation power, we observed a homogeneous occupation of the lower polariton branch. With increasing pulse energy, the emission intensity increased and the lower polariton line broadened. At the condensation threshold, reached for the pulse energy of 3.8 pJ, the emission nonlinearly increased, narrowed spectrally, and the lowest energy state was mainly populated. Further increase of the excitation power resulted in the appearance of interactions large enough to observe blueshifting and broadening of the condensate linewidth. The excitation laser was tuned nonresonantly to the first high-energetic Bragg minimum, so the main contribution to the blueshift was due to exciton-exciton interactions.

To study spin-related phenomena, we performed polarization-resolved measurements of photoluminescence. In Figure 4.3(a) we show the emission in the absence of a magnetic field observed below the condensation threshold in σ^- and σ^+ polarization. Three populated branches can be observed, corresponding to the lower (LP), middle (MP), and upper (UP) polariton. These modes are the result of strong coupling between heavy-hole (HH) and light-hole (LH) excitons with photons. All three branches are spin degenerate and have equally populated σ^+ and σ^- components. The emission from the lower polariton is the most intense. The higher modes are weakly occupied because of efficient energy relaxation from the excitonic reservoir to the ground state, so we focused on the lower polariton. In an external magnetic field, the degeneracy of LP is lifted as shown in Figure 4.3(b,c). Giant Zeeman splitting of the heavy hole exciton resulting from

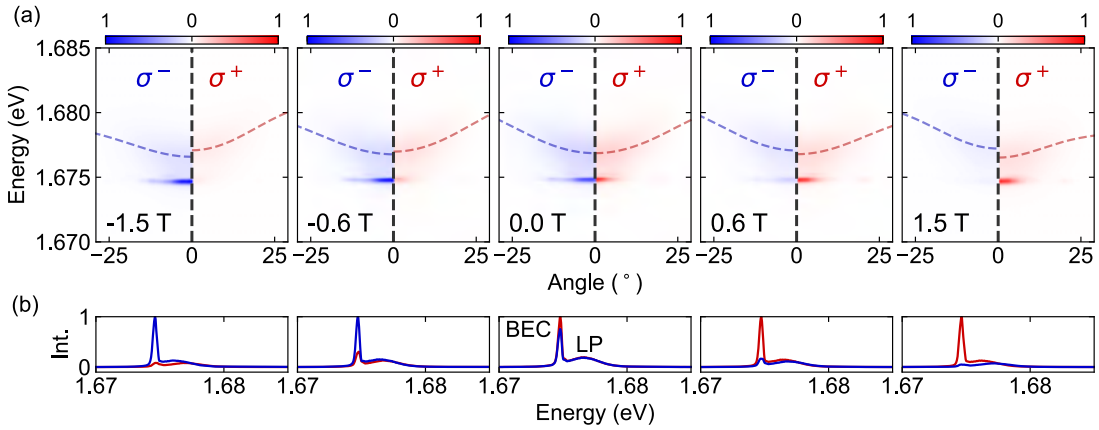

Figure 4.4: **Dispersion of semimagnetic exciton polaritons in external magnetic field above condensation threshold.** (a) Angle-resolved photoluminescence maps of polaritons in external magnetic field. σ^- (left) and σ^+ (right) polarised emission intensity is marked with blue and red color respectively. The dispersions of circularly polarised lower polariton branches are marked with the dashed lines. (b) Intensity of emission at zero wavevector for lower polariton (LP) and condensate (BEC) in σ^- (blue) and σ^+ (red) polarization extracted from the maps above.

the *s,p-d* exchange interaction between localized manganese ions and delocalized carriers gives the lower polariton splitting of about 2 meV at 2.0 T. The observed Zeeman splitting is comparable to the LP linewidth which is of 2.1 meV. Both observed modes are fully circularly polarized. There is a clear discrepancy in the occupation of the split branches with the predominance of the lower energy state.

We performed analogous studies for the same position on the sample above the condensation threshold. The emission resolved in angle, energy, and polarization was measured for the condensate at different magnetic fields (Figure 4.4). At the excitation power of $1.5\,P_{th}$ we observed strong emission from the condensate in both circular polarizations and a much weaker signal from a lower polariton. In the absence of a magnetic field, the lower polariton was unpolarized, and the occupation of opposite spin states was equal. However, the condensate was elliptically polarized with a predominance of a σ^+ component, what is better visible in a cross-section at zero emission angle. The condensate was spin-degenerated, there was no energy splitting visible. Interestingly, even a strong magnetic field of 1.5 T (or −1.5 T) does not split the condensate. This effect was previously reported as a spin Meissner effect [55]. With an increasing magnetic field, we observed a build-up of circular polarization of a condensate. The discrepancy in occupation was much larger for the condensate σ^+/σ^- spin polarized states than for the Zeeman split lower polariton modes. At 1.5 T the condensate was almost completely circularly polarized, the emission from the condensate was one order of magnitude greater in σ^+ than in σ^-. Analogous effects were observed at the negative magnetic field with a dominant σ^- spin component.

Based on the results presented in Figure 4.4 we calculated the degree of circular polarization of a condensate in the magnetic field. The degree of circular polarization $\wp$ can be defined as a normalized difference between the emitted light intensities $I_{\sigma^+}/I_{\sigma^-}$ observed in opposite circular polarizations as in equation (4.1).

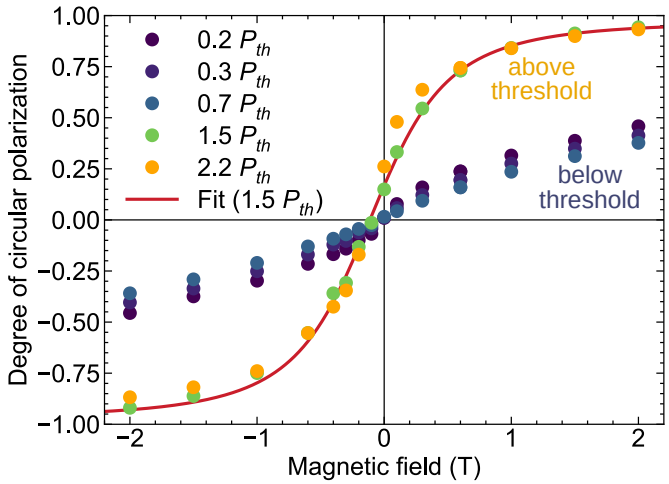

Figure 4.5: **Degree of circular polarisation of semimagnetic exciton polaritons for different magnetic field and excitation power.** The color code for excitation power is marked in the top left corner. The fit of equation 4.6 to data for excitation power of $1.5\,P_{th}$ is marked with a red curve.

$$\wp = \frac{I_{\sigma^+} - I_{\sigma^-}}{I_{\sigma^+} + I_{\sigma^-}} \tag{4.1}$$

The studies of $\wp$ in magnetic field are summarised in Figure 4.5. We measured angle-resolved emission maps in σ^+ and σ^- polarizations for five excitation powers: three below and two above the condensation threshold. We calculated the degree of circular polarization of the most intense line at zero emission angle. Below the condensation threshold, we observed zero degree of circular polarization in the absence of magnetic field. The increase of magnetic field resulted in a build-up of circular polarization. However, the magnetic field of 2 T (or −2 T) was insufficient to obtain a fully circularly polarized state. The increase of $\wp$ was slower for larger excitation power due to the heating of manganese ions observed previously in similar structures [67–69]. Above the condensation threshold, the degree of circular polarization increases much faster and does not depend much on the excitation power. At the magnetic field of 2 T (or −2 T) the condensate was almost fully circularly polarized. The qualitative difference between the linear and condensate regimes was also visible in zero magnetic field, where the condensate was elliptically polarized. To reduce to zero the $\wp$, an external negative magnetic field was needed. This is an indication of the presence of a synthetic magnetic field in the local potential minimum. The characteristics observed in Figure 4.5 resemble the exchange bias effect typically observed in the interacting antiferromagnetic-ferromagnetic layers [70]. This could be explained by the presence of antiferromagnetic inclusions of MnTe in the structure [71]. However, any amount of MnTe in the sample structure would indicate a lower epitaxy quality than expected.

Studies of the degree of circular polarization were also performed in real space (Figure 4.6). Note that here the observed degree of circular polarization was smaller than that measured in the reciprocal space, because of the averaging of the signal of noncondensed polaritons and the condensate. The $\wp$ was reduced by the particles occupying the lower and upper polariton branches. We observed a strong

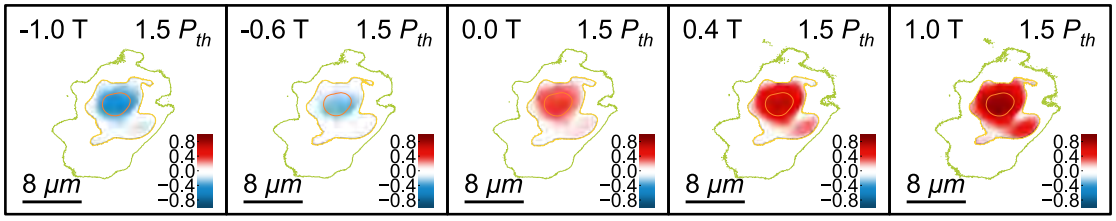

Figure 4.6: **Real-space maps of degree of circular polarisation of semimagnetic exciton polaritons above the condensation threshold in external magnetic field.** The annotations in the corners show a magnetic field, excitation power, and scale. Scale bars show the degree of circular of polarization.

localization in a potential minimum. The effect of a synthetic magnetic field was visible and we observed the elliptically polarized emission with the σ^+ component dominating over the σ^- polarized one. The change of the external magnetic field allowed for tuning of the spin polarization. The increase of the circular component was observed in the emission with increasing magnetic field. To reduce to zero the initial σ^+ spin polarization, the negative external magnetic field was needed. With the increasing value of the negative external magnetic field, the degree of spin polarization tended to be -1.

However, the spin polarization of the condensate can also be tuned by changing the power and polarization of the excitation laser. In the next experiment, we used a circularly polarized laser simultaneously exciting the area covering three photonic potential minima located next to each other. The degree of circular polarization of the polaritons localized in a local minimum is illustrated in Figure 4.7(a). Below the condensation threshold, the influence of excitation polarization was very weak, and the spin polarization of polaritons was mainly determined by the magnetic

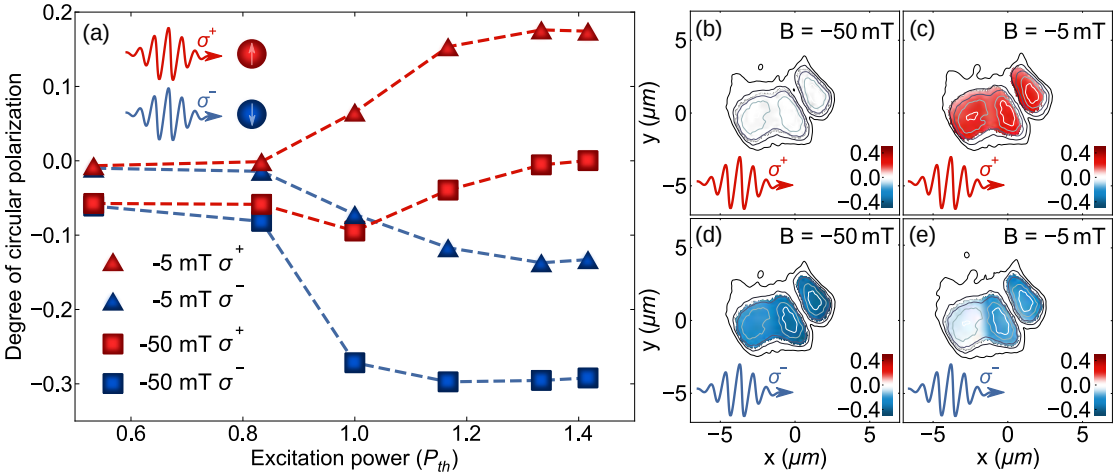

Figure 4.7: **Spin polarisation of a condensate induced by external laser.** (a) Degree of circular polarisation of condensate excited with circularly polarized laser. Annotation in left bottom corner indicates external magnetic field and polarization of excitation laser. Schematic illustration of the experiment is placed in top left corner. (b-e) Real space maps of degree of circular polarization for excitation power of 1.42 P_{th}. Magnetic field and polarization of the laser are marked in a top right and bottom left corner respectively.

field. At the condensation threshold, the nonresonant σ^+ polarized laser pulses created a greater degree of circular spin polarization than σ^- polarized ones. The difference between the condensate polarizations for opposite circular excitations was even greater for larger excitation power. The degree of circular polarization was controlled above the condensation threshold within the external magnetic field and the external laser. The negative magnetic field was decreasing $\wp$ and the laser polarization was increasing or decreasing the spin polarization depending on the handedness. The strength of the latter effect was changeable within the excitation power.

The degree of circular polarization observed in the real space for the condensates at the highest measured power ($1.42\,P_{th}$) is illustrated in Figure 4.6(b-d). In the magnetic field of $-50\,\mathrm{mT}$ the condensates formed by σ^+ polarized laser were linearly polarized. However, for σ^- polarized excitation, we observed a negative $\wp$ for condensates. In the smaller magnetic field, it was possible to reverse the spin polarization of the two condensates within the polarization of the laser. For the third condensate, the σ^- polarization of the laser decreased the $\wp$ to zero.

4.2 Polariton-polariton interaction strength

To describe the enhanced build-up of circular polarization of a condensate, we used a modified model describing the spin polarization of a condensate in the presence of magnetic ions [61]. In this model, the free energy of a condensate was minimized for a system with magnetic ions in an equilibrium state. This gives a formula that describes the degree of spin polarization in an external magnetic field:

$$\wp = \frac{n_M g_M \mu_B \lambda_M W\left(\frac{g_M \mu_B (B+\lambda_M \frac{n}{2}+B_{eff})}{k_B \cdot T}\right)}{n \cdot (\alpha_1 - \alpha_2)} \tag{4.2}$$

where n_M is a 2D concentration of magnetic ions, g_M is a g-factor, λ_M describes polariton-magnetic ion coupling, α_1 and α_2 are the interaction constants of polaritons with parallel and antiparallel spin configuration, respectively, and n is concentration of polaritons. The equation contains the term $W(x) = \sum_{j=-5/2}^{j=+5/2} \frac{j\exp(jx)}{Z(x)}$, defined by the statistical sum $Z(x) = \sum_{j=-5/2}^{j=+5/2} \exp(jx)$.

The value of g_M was calculated from the Zeeman splitting of the heavy-hole exciton at 5 T carefully studied for the same sample in [53]:

$$g_M = \frac{\Delta E}{\mu_B B} = \frac{2.8\,\mathrm{meV}}{0.29\,\mathrm{meV}} = 9.7 \tag{4.3}$$

The coupling constant was calculated on the basis of the exciton content χ^2 in the lower polariton and the width L_{QW} and number N_{QW} of quantum wells:

$$\lambda_M = \frac{\beta_{exc}\chi^2}{\mu_B g_M L_{QW} N_{QW}} = \frac{880\,\mathrm{meV} \cdot \frac{(0.648\,\mathrm{nm})^3}{4} \cdot 0.42}{\mu_B \cdot 9.7 \cdot 20\,\mathrm{nm} \cdot 4} = 5.6 \cdot 10^{-13}\,\mathrm{T \cdot mm^2}, \tag{4.4}$$

where β_{exc} is the integral of the CdMnTe exchange [18] $\left(\beta_{exc} = \frac{880\,\mathrm{meV}}{N_0}\right)$ and N_0 is the concentration of CdMnTe cations $\left(N_0 = \frac{4}{(0.648\,\mathrm{nm})^3}\right)$.

Table 4.1: Parameters obtained from the fitting procedure (Fit column) and calculations (Calc.) compared with parameters assumed in [61].

Parameter	**Fit**	**Calc.**	**[61]**
n_M [mm^{-2}]	$7.4{\cdot}10^{10}$	–	$5{\cdot}10^{12}$
g_M	–	9.7	2.02
n(α_1-α_2) [meV]	0.06	–	2.4
λ_M [T·mm^2]	–	$5.6{\cdot}10^{-13}$	$2.56{\cdot}10^{-11}$
B_{eff} [T]	0.11	–	–
T [K]	5.0	–	–

Having calculated the parameter λ_M, we were able to estimate the upper limit of the term $\lambda_M \frac{n}{2}$ by substituting the polariton concentration with the exciton saturation density n_{exc}^{sat} [72]:

$$\lambda_M \frac{n_{exc}^{sat}}{2} = 5.6 \cdot 10^{-7}\,\mu\mathrm{T} \cdot \mathrm{mm}^2 \cdot \frac{4.8 \cdot 10^7\,\mathrm{mm}^{-2}}{2} = 13\,\mu\mathrm{T} \tag{4.5}$$

In the following chapter, this term was neglected because of the small contribution to the total polarization. The equation 4.6 presents the formula with the omitted term.

$$\wp = \frac{n_M g_M \mu_B \lambda_M W\left(\frac{g_M \mu_B (B+B_{eff})}{k_B \cdot T}\right)}{n \cdot (\alpha_1 - \alpha_2)} \tag{4.6}$$

This equation was used to fit the degree of circular polarization presented in Figure 4.5 and measured for $P = 1.5\,P_{th}$. The parameters obtained from the fitting procedure along with the calculated parameters are summarized in Table 4.1 We put the values obtained from the fitting procedure with the parameters proposed for the CdMnTe sample in [61].

From the two-dimensional concentration of manganese ions n_M, we calculated the manganese ions concentration n_{Mn}:

$$n_{Mn} = \frac{n_M}{\sqrt[3]{(N_0)^2}} = 1.2\% \tag{4.7}$$

This value agrees well with the manganese concentration assumed from the MBE growth conditions. We were particularly interested in obtaining the value of the polariton-polariton interaction strength because it has not been previously reported for CdTe-based samples. Unfortunately, within this method we were unable to precisely define the polariton-polariton interaction constants for parallel and antiparallel spins, but we accurately determined the term $n(\alpha_1 - \alpha_2)$ that describes the polariton blueshift caused by interactions. We obtained the blueshift of 60 µeV, which was 24% smaller than the total blueshift acquired from the spectroscopic measurements. This suggests that the main contribution to the blueshift comes from interactions in the excitonic reservoir [74]. On the basis of the obtained parameter, we estimated the polariton interaction strength. For this reason, we plotted the interaction strength as a function of polariton concentration [Figure 4.8(a)]. The blue region illustrates the possible values of the interaction strength. The dashed line describes the exciton saturation density in CdTe of

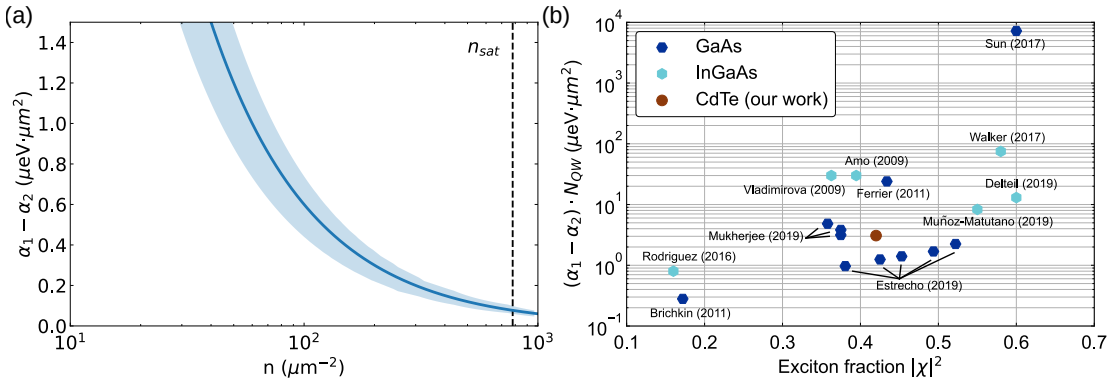

Figure 4.8: **Polariton-polariton interaction strength.** (a) Estimation of the polariton strength and polariton concentration. Blue line outlines the equation $n(\alpha_1 - \alpha_2) = 0.06\,\text{meV}$. The light blue area indicates the confidence level obtained from the uncertainty of manganese ions concentration n_{Mn}=(1±0.3)%. Exciton saturation density in cadmium telluride is marked with the dashed line. (b) Comparison of estimated polariton-polariton interaction strength with values previously reported in different systems, based on [73].

$7.8{\cdot}10^2\,\mu\text{m}^{-2}$. We estimated the polariton concentration to be one order of magnitude lower than the exciton saturation density [75]. Based on this assumption, we obtained the polariton-polariton interactions of $0.8\,\mu\text{eV}{\cdot}\mu\text{m}^2$. We compared this value with the polariton-polariton interaction constants previously reported for another systems [Figure 4.8(b)].

Using the parameters obtained from the calculations and the fitting, we plotted the equation 4.6 describing the degree of circular polarization of a condensate in Figure 4.9. In the diagram, one can distinguish four spin phases. In the magnetic field of $-0.11\,\text{T}$, independently on the temperature, the condensate was linearly

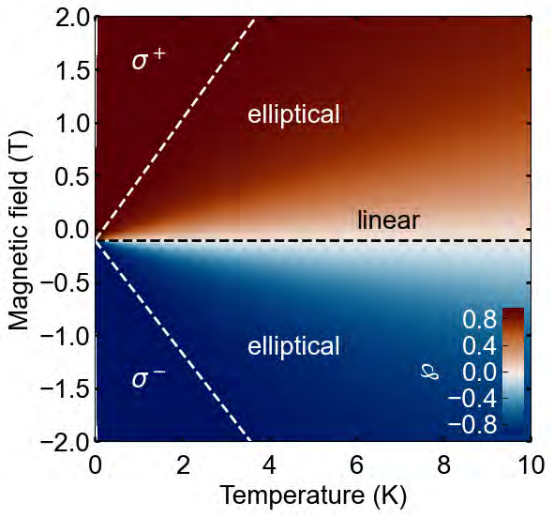

Figure 4.9: **Degree of circular polarization of a condensate.** Phase diagram calculated for parameters given in Fit and Calc. columns in Table 4.1. The distinct phases are separated with the white dashed lines. Note, that the linear polarization (marked with the black dashed line) occurs at nonzero magnetic field. Phase map corresponds to a specific position on the sample.

polarized. With increasing field, the condensate changed polarization from linear through the elliptical to circular. The change was more abrupt with the decrease of temperature.

4.3 Origin of synthetic magnetic field

To understand the nature of the synthetic magnetic field, we performed studies of polarization-resolved emission for a very negative exciton-photon detuning that was three times greater than the coupling strength (Figure 4.10). We excited the sample with a linearly polarized laser at the condensation threshold P_{th}. In the absence of the magnetic field, the ground state was elliptically polarized with a bigger left-handed circular polarization contribution, while the bottleneck region was linearly polarized. Spin polarization of both the ground state and the high wavector particles was tuned with the magnetic field. The build-up of spin polarization in the external magnetic field was much faster for the lowest energy state than for the bottleneck. The nonzero circular polarization component observed for the ground state in the absence of a magnetic field suggests that the synthetic magnetic field results from purely photonic effects.

It is interesting that the value of the synthetic magnetic field changes randomly with the position on the sample. We created one hundred condensates in different positions on the sample using a linearly polarized laser for excitation and studied the polarization of the emitted light. We measured six polarization components: horizontal (H), vertical (V), diagonal (D), antidiagonal (A), right-handed circular (σ^+) and left-handed circular (σ^-). The detailed description of the polarization setup is described in Sec. 4.5. The six parameters measured for the photons emitted from each condensate are visualized on a Poincaré sphere [Figure 4.11(a)]. We observed that for most positions on the sample, the dominant polarization component was horizontal. The circular polarization part was changing from -0.5 to 0.5. We also observed a correlation between the linear and circular components. The condensates having a greater part of $\sigma^+\backslash\sigma^-$ polarization also had a contribution of antidiagonal\diagonal polarization, respectively. We performed an analogous ex-

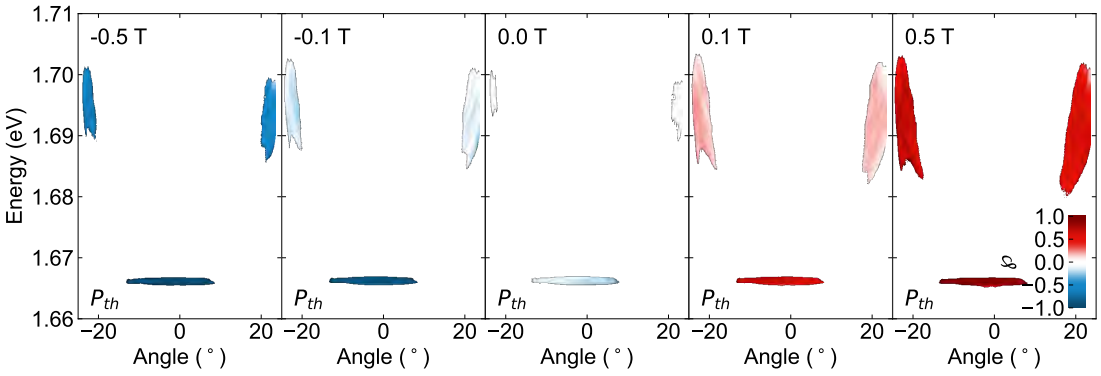

Figure 4.10: **Degree of circular polarization of polaritons with negative exciton-photon detuning in external magnetic field.** Separate colorbars placed in the bottom right corner show color scale. Annotations show external magnetic field (top left) and excitation power (bottom left) of linearly polarized laser. For better visibility the emission below 1% of maximum intensity was filtered out.

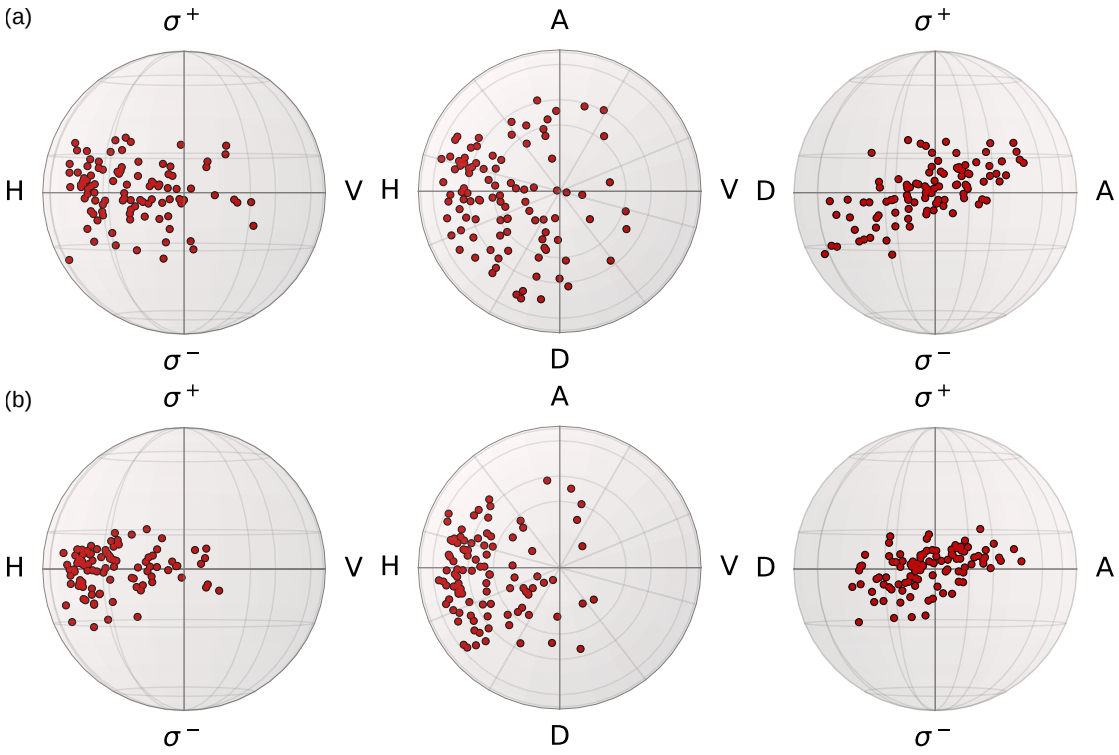

Figure 4.11: **Stokes parameters for 100 condensates.** Polarisation of light emitted from one hundred condensates on a sample (a) MC-S with, and sample (b) MC-N without manganese ions in the quantum wells. Subsequent plots show different views on a Poincaré sphere.

periment on a sample MC-N without manganese ions in the structure. We created 100 condensates under the same experimental conditions and studied the polarization of the emitted light marked on a Poincaré sphere in Figure 4.11(b). We observed an emission with dominating horizontal polarization for most positions. On this sample we also observed a synthetic magnetic field: the condensates were elliptically polarized with random spin polarization changing with the position on the sample. Again, we observed a correlation between the $\sigma^+\backslash\sigma^-$ and A\D polarizations.

On the basis of the above results, we calculated the Stokes parameters S1, S2, and S3 that describe the polarization state of the emitted light of each condensate:

$$S_1 = \frac{I_H - I_V}{I_H + I_V}, \qquad S_2 = \frac{I_D - I_A}{I_D + I_A}, \qquad S_3 = \frac{I_{\sigma^+} - I_{\sigma^-}}{I_{\sigma^+} + I_{\sigma^-}} \tag{4.8}$$

where I_x is the light intensity observed in polarization x. We were especially interested in a linear ($\mathcal{L}$) and circular ($|\wp|$) contribution to the total polarization, which we calculated based on the Stokes parameters following:

$$\mathcal{L} = |\sqrt{S_1^2 + S_2^2}|, \qquad |\wp| = |S_3| \tag{4.9}$$

In Figure 4.12 we present the histograms showing the distribution of both components in condensates for a sample with and without manganese ions in the quantum wells. From the histograms, we concluded that the manganese ions play

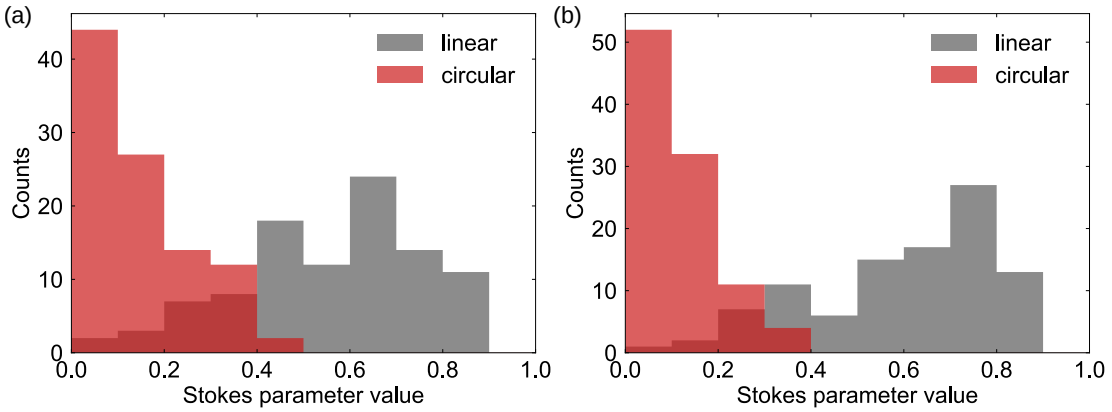

Figure 4.12: **Distribution of linear and circular polarization component in condensates.** Distribution of linear and circular polarization component in emission for randomly chosen condensates studied on a sample a) with and b) without manganese ions in the quantum wells.

no role in the presence of a synthetic magnetic field. For both samples, we observed dominating linear polarization for the majority of the condensates, but the circular contribution was unmistakably large. The condensate spin polarization for both samples was random in the absence of a magnetic field with a nonzero circular component. The distribution of $\mathcal{L}$ and $|\wp|$ was qualitatively the same, confirming that the synthetic magnetic field does not origin from the presence of manganese ions.

To check the stability of the synthetic effective magnetic field in the external magnetic field, we performed measurements of the intensity, blueshift, and full width at half maximum (FWHM) of the most intense emission line at zero wave vector in a circular polarization basis (Figure 4.13). We compared these three quantities in the absence of a magnetic field before and after applying an external magnetic field of $-5\,\mathrm{T}$. We observed an increase of intensity and blueshift with increasing excitation power. The linewidth was decreasing with increasing excita-

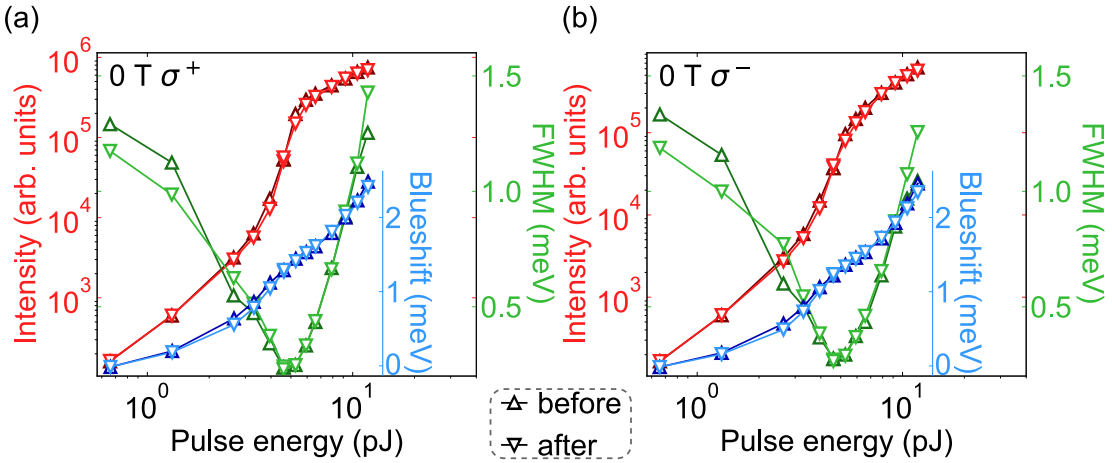

Figure 4.13: **Stability of the synthetic magnetic field.** Power dependencies for intensity, blueshift and linewidth of the most intense emission line at 0 T before and after applying external magnetic field of $-5\,\mathrm{T}$. Panels a) and b) correspond to σ^+ and σ^- detection.

tion power until it reached the condensation threshold. Above the threshold, we observed a broadening of the line. In both σ^+ and σ^- polarizations, there was no discrepancy between the data measured before and after the magnetic field was applied. This confirms that the observed effects do not depend on the magnetic history and are not a result of the permanent orientation of manganese ions.

4.4 Summary

This chapter introduced the properties of samples measured in this thesis and microcavities with semimagnetic quantum wells in general. We discussed the spin properties of exciton polaritons and condensate in an external magnetic field.

In Sec. 4.1 we showed that in the linear regime, the nonresonant, linearly polarized laser creates linearly polarized exciton polaritons manifesting giant Zeeman splitting in an external magnetic field. The same effects do not apply to a condensate that manifests a nonzero degree of circular polarization and the giant spin Meissner effect in the magnetic field. The appearance of a circular component in total polarization is a consequence of a synthetic magnetic field. This effective magnetic field originates from the inhomogeneities of the DBRs and cavity and is randomly distributed on a sample.

In Sec. 4.2, we presented a method to estimate the polariton-polariton interaction strength from the spin properties of the polariton condensate in an external magnetic field. We found that the determined interactions are comparable to those obtained for GaAs- and InGaAs-based structures. We were able to produce a full spin-phase diagram for a polariton condensate.

In Sec. 4.3 we discussed the properties of the synthetic magnetic field. We show that it is stable in time and cannot be changed by an external magnetic field or excitation laser. We show that the circular polarization contribution to the total condensate polarization can be tuned by an external magnetic field or an excitation laser. When the polarization of the laser is changed, it is possible to choose the direction of the polarization. The excitation power tunes the strength of this effect.

In summary, the introduced system manifests strong nonlinear effects related to the spin degree of freedom, which can be easily tuned with external parameters. The presented effects pave the way for the use of spin effects in practical applications such as neuromorphic computing or quantum simulators.

4.5 Appendix: Alignment of polarization detection setup

The light emitted from the condensates is directly related to the polariton properties. Similarly, the spin polarization of polaritons is directly related to the polarization of the emitted light. Thus, polarization-resolved studies of emission allow for studies of the spin properties of exciton polaritons. The alignment procedure for these studies is presented in Figure 4.14. The main idea is to measure the contribution of horizontal (H), vertical (V), diagonal (D), antidiagonal (A), right-handed circular (σ^+) and left-handed circular (σ^-) components to the light polarization. This can be achieved by transforming each component into the linear one using polarization optics and measuring its intensity on the CCD camera behind the spectrometer.

The intensity on the CCD camera depends on the polarization of the incident light due to the different diffraction efficiency of the grating in the spectrometer [76]. For this reason, it is a good practice to direct light of the same polarization to the camera. In the first step, we check for which linear polarization the grating has the highest diffraction efficiency [Figure 4.14(a)]. We guided the laser beam through the half-wave plate and measured the intensity for different rotation angles. The half-wave plate rotated the linear polarization of the laser beam

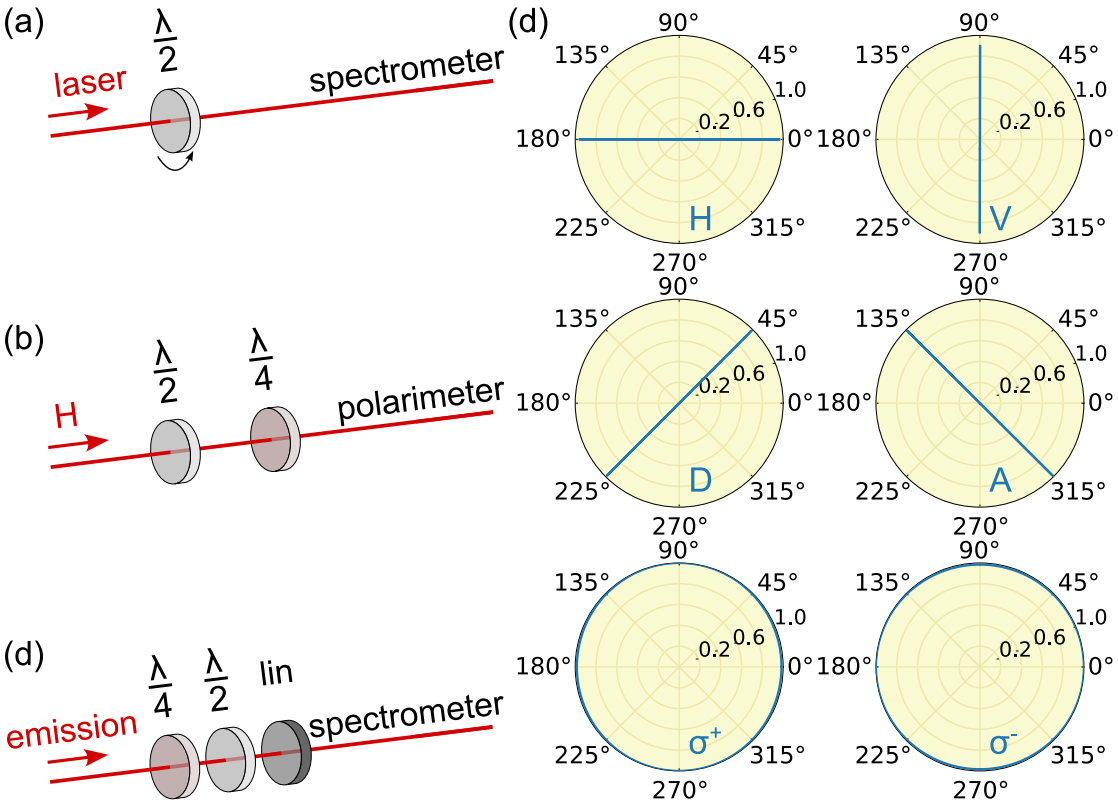

Figure 4.14: **Alignment of polarization detection**. (a) First, (b) second and (c) third step of the polarization-resolved setup alignment. $\frac{\lambda}{2}$, $\frac{\lambda}{4}$ and *lin* correspond to half-wave plate, quarter-wave plate and linear polarizer. (d) Normalized electric field of polarized light measured in the second step on a polarimeter. Each studied light polarization is described with blue annotation on the bottom.

without changing its intensity. However, the intensity on the CCD camera behind the spectrometer was changing. We chose the light polarization for which the intensity on the CCD camera was the largest, which turned out to be horizontal. In the second step, the horizontally polarized laser beam was passed through the half-wave plate and the quarter-wave plate [Figure 4.14(b)]. We transform the horizontally polarized light into the H, V, D, A, σ^+ and σ^- polarized light by rotating both elements and then note the rotation angles for each polarization. The rotation angles were set while measuring the x- and y- components of the electric field using a polarimeter (TXP Polarimeter PAX5710IR1). Exemplary fields measured for each polarization are presented in Figure 4.14(d). As shown in the panel, it is possible to obtain each polarization with high accuracy. In theory, single half- and quarter-wave plates are enough to transform any polarization into any polarization. The rotation of half-wave (quarter-wave) plate allows for changing the polarization along the circle of latitude (meridian) on a Poincaré sphere. In practice, the optical elements can be imperfect or the optical elements in the experimental setup can lead to slight deviations. This problem can be resolved by using another half-wave or quarter-wave plate in the setup and compensating for the differences between the expected and obtained results. The last step is based on the fact that light polarization is subject to time-reversal symmetry [77]. We swapped the quarter-wave plate and the half-wave plate and placed the linear polarizer set to horizontal polarization before the spectrometer [Figure 4.14(c)]. Using the rotation angles saved in the second step, we were able to transform any polarization component of the light emitted from the sample into a horizontal component and then filter it with the linear polarizer. Within this method we were able to measure the intensity of all three Stokes components just by changing the rotation angles of the polarization optics and measuring the intensity on the CCD camera. This described procedure allows for measuring not only the imbalance in the occupation of two opposite spin states but also full information about the polarization of the emitted light.

Chapter 5

Photonic potential

Cadmium telluride-based microcavities are characterized by a rich photonic potential created by natural defects. The disorder observed on the quaternary structures has a strong impact on the properties of exciton polaritons and condensate. In this chapter, we present an investigation of the natural photonic potential. Furthermore, we use the disorder to create a nonlinear system.

The potential distribution strongly depends on the quality of the sample. The main sources of potential fluctuations are defects of various types. The typical GaAs-based samples have a potential distribution of several tens/hundreds of µeV and Q-factors greater than 10,000 [9, 78, 79]. The CdTe-based samples investigated in this work have an inhomogeneous potential of the order of few meV that provides deep localization levels and leads to strong spatial localization. The structures measured in this study are made of quaternary layers, which limits the Q-factor to values below 2,000 [80].

In a non-resonant excitation, the laser creates an excitonic reservoir with strong Coulomb interactions forming a potential acting on polaritons. On gallium arsenide samples with homogeneous potential, the radial movement of the polaritons from the excited place is observed because of the blueshift created by the external laser [81, 82]. On samples with internal disorder, the localization of polaritons in local minima is dominating [83, 84]. However, the photonic potential landscape can be used to produce nonlinearities.

In this chapter, we will discuss various basic potential configurations and use them to create nonlinear systems.

5.1 Polariton localization in potential inhomogeneities

We performed real-space reflectivity measurements to explore the photonic potential landscape. We measured the lower polariton energy for two positions with different photon-exciton detuning. The energy-resolved maps in the real space presented in Figure 5.1 reveal the density and depth of the potential minima. We observed numerous randomly distributed defects located throughout the observation area with a density of about 1 defect per 2.5 µm^2. At positive detuning (panel (a)), the energy changes are smaller than at negative detuning (panel (b)). From the lower polariton energy changes, we extracted the mean energy and obtained the energy residuals, which correspond to the depth of the defects. The distribu-

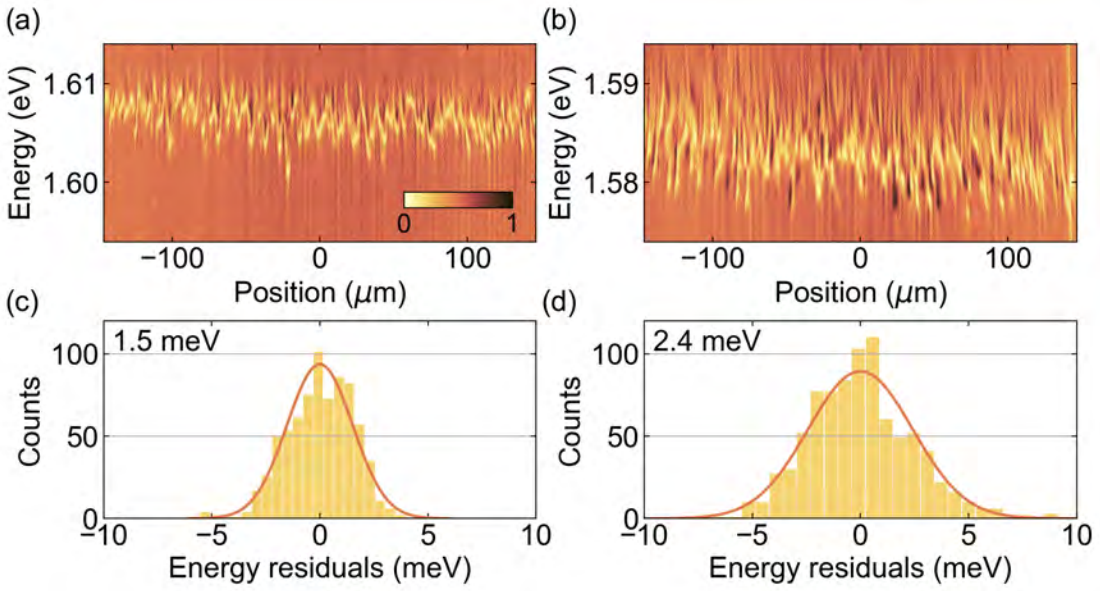

Figure 5.1: **Photonic potential inhomogeneities.** Real space maps of lower polariton reflectivity at (a) positive (b) negative detuning. Scale bar in panel (a) show the color scale for both reflectivity maps. Distribution of the lower polariton energy residuals from the mean energy at (c) positive (d) negative detuning. Red curve corresponds to the fitted Gaussian function. Standard deviation obtained from the fitting is marked in the top left corner. Experiment performed at the University of Würzburg during the internship.

tion of the energy residuals for positive detuning is presented in Figure 5.1(c). The Gaussian function fitted to the distribution revealed a standard deviation of 1.5 meV. This value is comparable to the typical line width of the lower polariton in this sample. At the negative detuning (panel (d)), the dispersion of energy residuals is much larger. The depth of the defects was reaching almost 10 meV. The standard deviation of the obtained energy residuals from the Gaussian fitting was 2.4 meV. Interestingly, despite the similar density of the energy minima for both positions, the difference is evident in the magnitude of the energy changes. The energy changes of lower polariton scale with its photonic component. The lower the Hopfield coefficient $|C^2|$ the smaller the changes of the lower polariton. This confirms that the inhomogeneities observed on the sample have a photonic origin.

The internal photonic potential has a direct impact on the condensates. We studied real-space photoluminescence below and above the condensation threshold (Figure 5.2). We chose a position with many localized states of different energies. Below the threshold (panel (a)) we observed emission from the lower polariton and discrete states below the dispersion. The position of the most localized state is marked with the dashed line. For a higher excitation power (panel (b)), we observed condensation at the same position of the sample. This shows that the condensates are localized in a potential minima. Depending on the position on the sample, the potential is different, so the energies of polariton and condensate are also different.

However, the natural photonic disorder can be used to create a highly nonlinear system. We discuss four different scenarios possible in a system consisting of

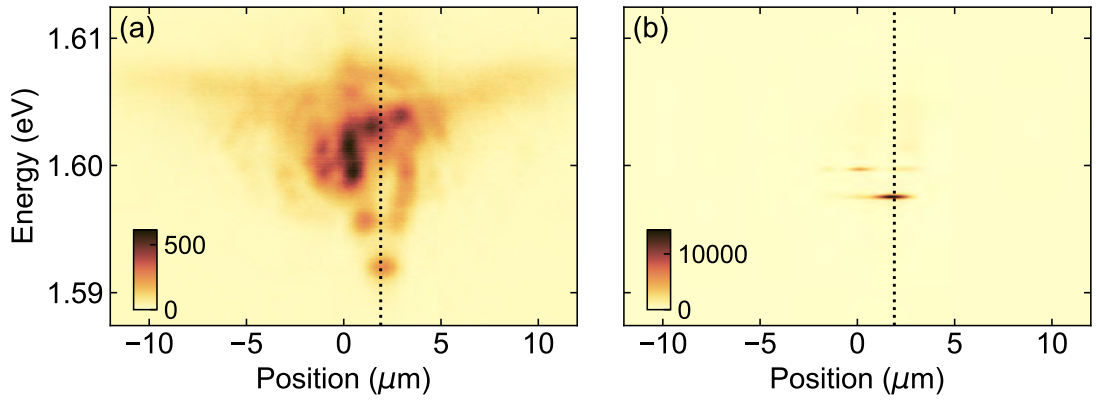

Figure 5.2: **Condensation in a potential minima.** Real space photoluminescence maps for excitation power (a) below (b) above the condensation threshold. Dashed line corresponds to the position, where the lowest energetic localised state was observed at lower excitation power.

two condensates in the vicinity of potential inhomogeneities (Figure 5.3). In panel (a), the condensates are localized in two spatially separated potential minima. The barrier between the condensates is large enough to prevent any interactions between them. In this scheme, the condensates behave like two separate systems and their properties are independent. When spatial separation and barrier between condensates are smaller, the condensates can interact with each other (panel (b)). This type of potential has been used to create coupled condensates and observe Josephson oscillations [85–87]. The photonic potential acting on polaritons, can be effectively reduced due to the interactions: large polariton occupation in the local miminum can lead to the ground state blueshift. In particular, by increasing polariton population or the interactions in the left minimum one can make a transition from the scenario described in Figure 5.3(b) to the one illustrated in Figure 5.3(c). This can be achieved for example in nonresonant excitation, when the high-energy pulse creates large concentration of excitons interacting with each other which leads to the blueshift of the polariton energy. For high enough exci-

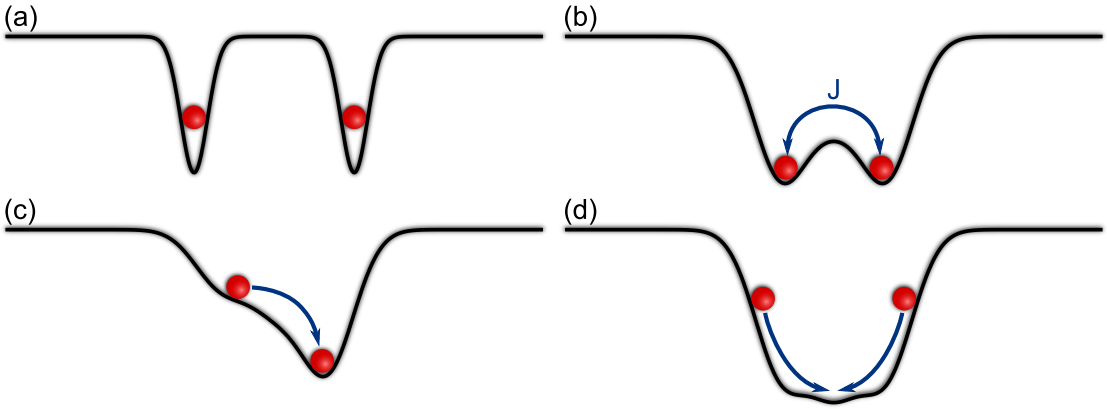

Figure 5.3: **Two condensates in a vicinity of a photonic potential.** Schemes of (a) two localized, not interacting condensates (b) two condensates interacting with each other with the coupling J (c) particles flow from one condensate to another (d) two opposite flows of particles between the condensates.

tation power, the created potential can exceed the confining potential and allow polariton flow from the first spot to another. As a result, polariton flow depletes polariton density in one place and increases in another. The presented scheme is a source of large nonlinearities. However, the particles flow can occur from two excited places on the sample. The scheme presented in Figure 5.3(d) shows the particles created on the opposite slopes of the potential. In this realization, the particles flow in the opposite directions and interact with each other in the place where they meet. The particles flowing in opposite directions have been used for simulations of a spin-glass and phase synchronization experiments [81, 88, 89].

5.2 Mutual flows of polaritons between condensates

We investigated a configuration with two potential minima separated by a potential barrier. Systems with a single potential barrier have already been applied to control the quantum state of a polariton superfluid [90], build linear logic gates [91] and transistor switches [92], or study polariton propagation [93]. Here, we excited two potential minima with two beams of the nonresonantly tuned pulsed laser. As part of an initial characterization, we excited only the first condensation site and measured the emission in real space (Figure 5.4). The laser was aligned perpendicularly to the sample so that no momentum was injected into the particles. However, at high excitation power, we observed the signatures of particles flowing from the potential minima. On a CCD camera [Figure 5.4(a)], we observed an increase of the emission intensity with increasing excitation power. The narrowing of the emitting region with increasing laser pulse energy was observed, indicating a strong localization. At the two highest powers, the emission was also visible on

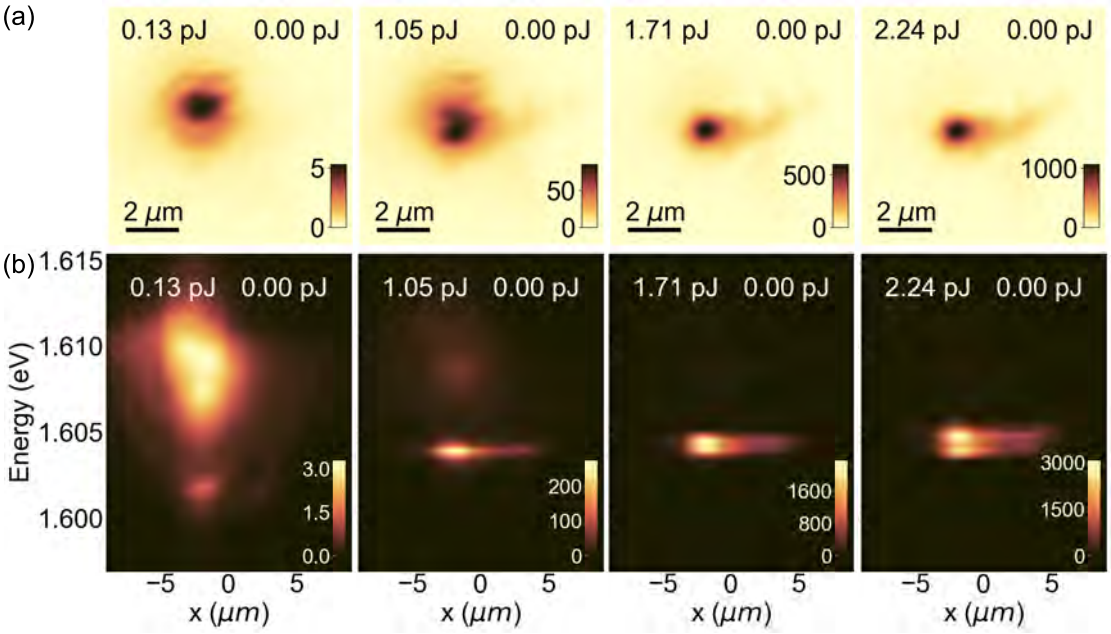

Figure 5.4: **First condensation site characterization.** (a) Real space (b) energy resolved maps of emission from the first condensation site. Top left (right) annotation illustrates the pulse energy of the laser exciting the first (second) condensation site.

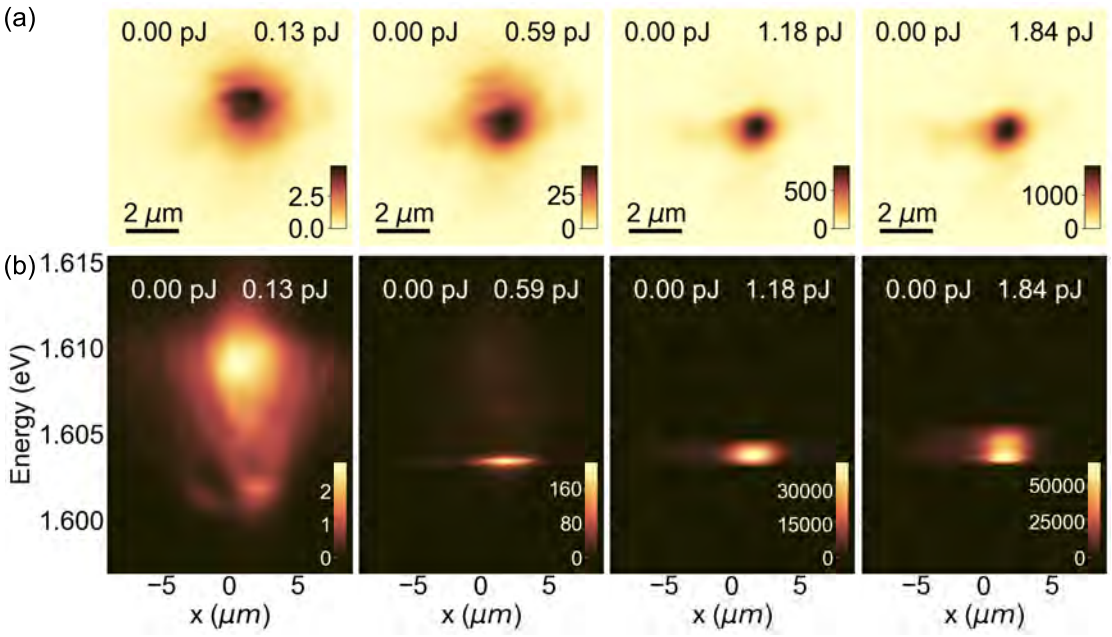

Figure 5.5: **Second condensation site characterization.** (a) Real space (b) energy resolved maps of emission from the second condensation site. Top left (right) annotations illustrate the pulse energy of the laser exciting the first (second) condensation site.

the right side of the excited position, suggesting the flow of particles from the first condensation site. The energy-resolved photoluminescence maps measured in real space are presented in Figure 5.4(b). For a pulse energy of 0.13 pJ, we observed a weak emission from the lower polariton in the excited place and the occupation of a localized state of about 1.601 eV. At higher excitation power, condensation occurred and the particles occupied the lowest energy state. An additional increase of the excitation power resulted in an increasing blueshift of the condensate. Note that there is also a visible emission from the states located to the right of the stimulated place, at the second condensation site.

An analogous measurement was repeated for the second condensation site (Figure 5.5). For this position, the localization and polaritons flow effects were present. For a low excitation power, we observed emission from the excited place. For higher powers, the polaritons were localized at the local potential minimum. Signs of particle flow were observed in the emission present to the left of the excited site. In fact, one can see that a single excitation beam affects both condensation sites. The energy-resolved measurements revealed lower polariton emission from the excited site at low power and localized condensate emission at high excitation power. Similarly to the previous place, the localized state can be distinguished in the low-power regime, which increases its energy with increasing pulse energy. The line width decreases at the condensation threshold and then increases as a result of increased interactions.

From the real space maps, we calculated the mean intensity of the emission in the excited sites and presented in Figure 5.6. Panel (a) corresponds to the emission intensity from the first (red) and second (blue) condensation sites, while only the first one is excited. The photoluminescence observed from the first condensation site was increasing with the excitation power, and at some point we obtained a nonlinear increase in the intensity. The second condensation site was insensitive to

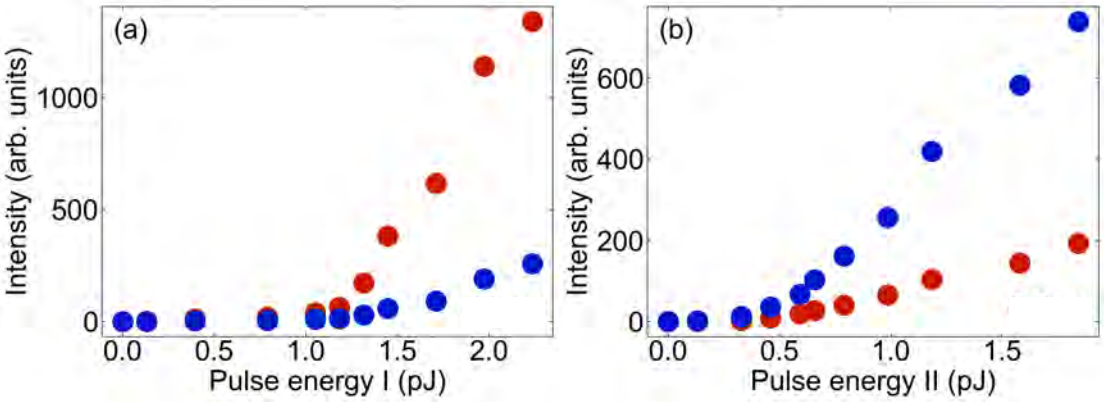

Figure 5.6: **Emission from individually excited condensation sites.** Emission intensity from the first (red circles) and second (blue circles) condensation site for different pulse energy of the (a) first (b) second laser beam.

the first beam in the low-power regime. However, with higher powers, the emission intensity from the second condensation site was also increasing. This is the signature of the polariton flow between the condensation sites. Panel (b) corresponds to the excitation of the second condensation site. In this realization, both spots responded to the applied excitation power. The first condensation site increased its intensity with increasing laser pulse energy. However, there was no threshold behavior. The excited place was more sensitive to laser pulses and increased the intensity more efficiently. The condensation threshold in this site was observed at around 0.6 pJ.

The Figure 5.7 shows the angularly resolved emission for laser excitation of the first (a) and second (b) condensation site separately. The slit of the spectrometer was aligned to be parallel to the axis defined by the condensation sites. Below the condensation threshold, we observed a dispersion of the lower polariton for both places. Above the condensation threshold, we obtained a single macroscopically occupied state. The emission lines were blueshifting and widening with increasing excitation power. Note that for the panels corresponding to the excitation of the first condensation site the highest intensity was observed for the positive wave vectors, and for the excitation of the second condensation site the states with negative wave vectors were the most populated. This suggests that the potential on the sample modified by laser-induced interactions forces the polaritons to flow between the condensates.

Based on the obtained maps, we plotted the emission intensity, blueshift, and full width at half maximum of the most intense mode for excitation of the first [Figure 5.8(a)] and second [Figure 5.8(a)] condensation site. Both excited sites had similar blueshifts, condensation thresholds (1.1 pJ and 0.6 pJ, respectively) and linewidth. The linewidth in both condensation sites decreased to about 0.5 meV when condensation occured. The interactions present in the system were enough to increase the FWHM above 2 meV and blueshift the emission line more than 3 meV.

The interesting features appear in the experiment configuration with the two simultaneously excited condensation sites. In Figure 5.9(a) we presented the real space emission from the characterized potential minima excited previously with separate laser beams. We excited one condensation site with a constant pulse en-

ergy and another condensation site with a changing energy of the second pulse. Surprisingly, on the second and third panels, the more intense emission was observed from the site excited with smaller pulse energy. In general, an increase of the emission intensity would be expected at the position where the excitation power increases. In this case, despite an increase of the excitation power of only the first condensation site, the emission increased in both sites. The presented emission maps suggested that at some point, the increase of the emission was even faster in the site excited with constant power.

In Figure 5.9(b) the subsequent panels correspond to the emission from the

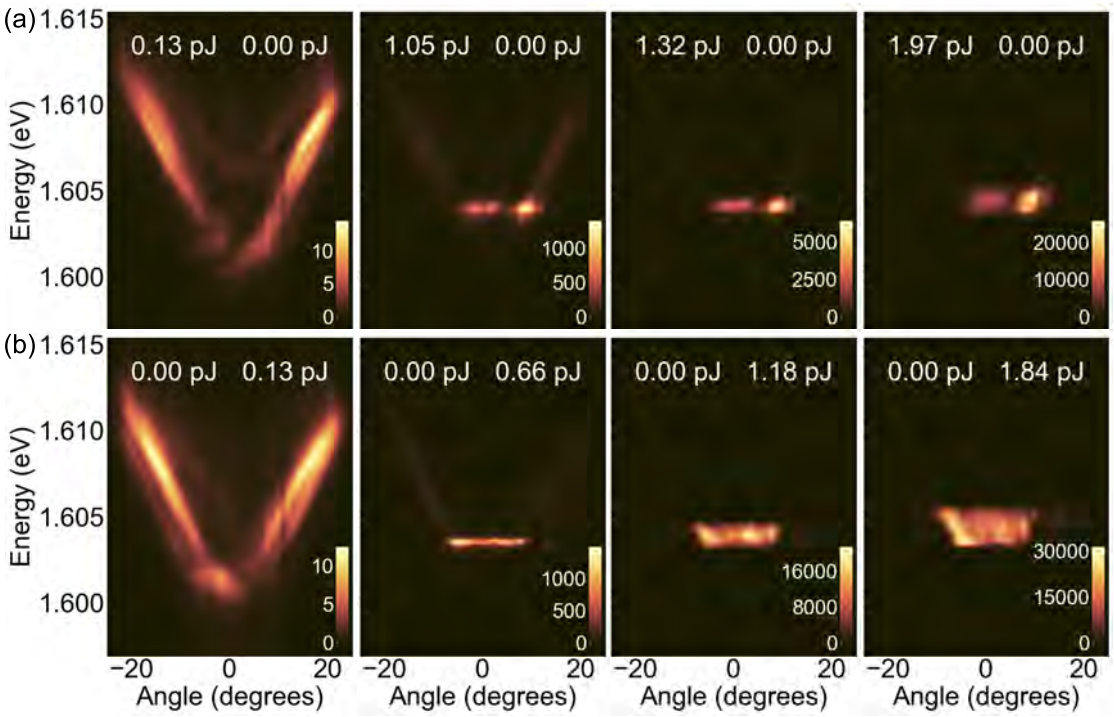

Figure 5.7: **Condensation sites characterization in momentum space.** Angularly and energy resolved maps of emission from the (a) first (b) second condensation site. Top left (right) annotations illustrate the pulse energy of the laser exciting the first (second) condensation site. Color scales give information about the intensity of emission on each panel.

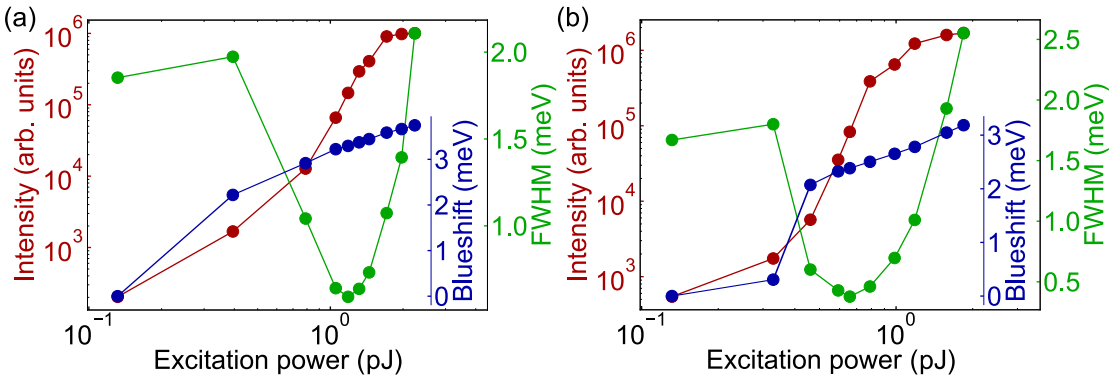

Figure 5.8: **Occupancy of individually excited condensation sites.** Intensity, blueshift and full width at half maximum of the most intense mode at zero emission angle for pulse energy of the laser exciting the (a) first (b) second condensation site.

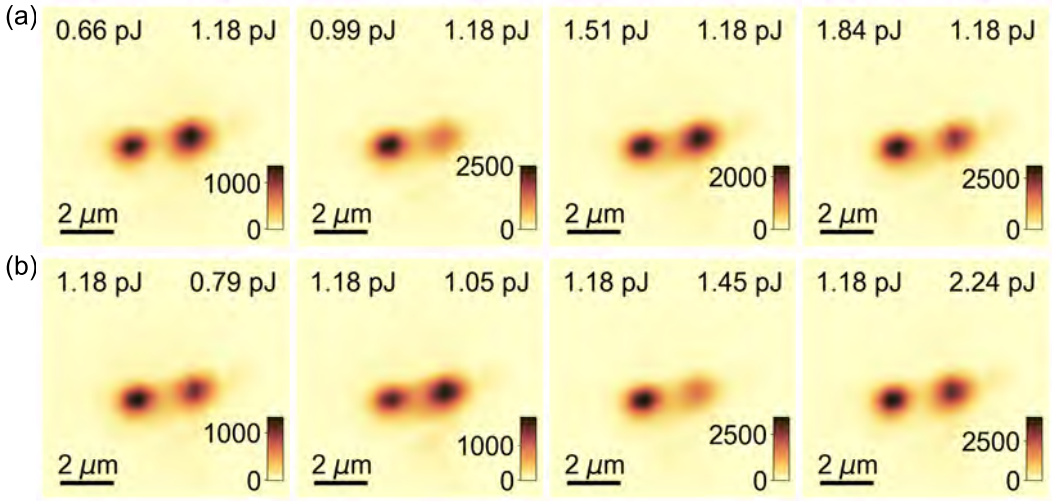

Figure 5.9: **Emission from simultaneously excited condensation sites.** Real space emission maps from the two excited condensation sites. The pulse energy is constant for (a) second (b) first condensation site. Top annotations illustrate the pulse energies of the laser exciting the first (left) and second (right) condensation site. Color scales give information about the intensity of emission on each panel.

first condensation site excited with the constant pulse energy and second condensation site excited with the increasing pulse energy. Again, the spots with the larger emission despite the smaller excitation power can be distinguished. For the pulse energies of the second pulse of 0.79 pJ and 1.45 pJ the first condensation site was more populated. In the other two panels, the emission from the second condensation site was greater than that from the first one.

The average intensity in both condensation sites calculated from the presented maps is illustrated in Figure 5.10. The characteristic in panel (a) corresponds to the constant pulse energy of the laser beam exciting the second condensation site. In the region of low pulse energies of the first beam, the emission increases at the first condensation site and remains constant at the second condensation site. Above the pulse energy of 1.2 pJ the occupation of the condensate began to decrease in the first site. At the same power, an increase in emission was observed in the second condensation site. At this pulse energy, the particles started to flow from the first condensate to the second. In the high-power regime, the emission intensity from the first condensate increased again and remained constant in the second one. The polaritons flux was stopped, and the second condensation site was again insensitive to the external laser.

In Figure 5.10(b) we presented the emission intensity for different pulse energy of the laser beam exciting the second condensation site while exciting the first condensation site with constant power. Here, increasing the energy of the second pulse leads to an increase in the intensity of the emission from both excited sites, with a greater change observed for the excited condensation site. This time, for a certain pulse energy, the occupation of the first condensate increased significantly at the expense of reducing the occupation of the second condensate. The emission from both condensates then increased again, but again the intensity observed for the condensate excited by the second beam changed faster. These results confirm that particle flows occur between the condensates, and the direction and size of

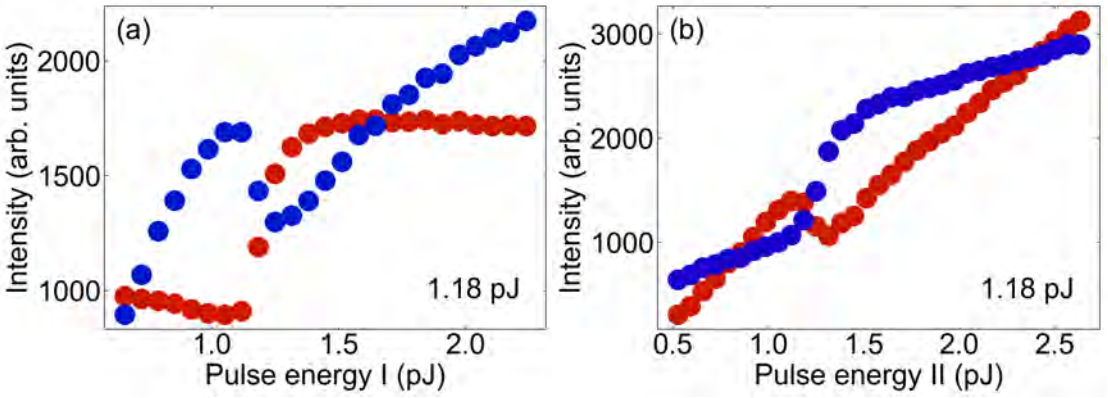

Figure 5.10: **Occupancy of simultaneously excited condensation sites.** Emission intensity from the first (red circles) and second (blue circles) condensation site for different pulse energy of the (a) first (b) second laser beam. The annotation in bottom right corner shows the energy of another pulse.

these flows can be controlled by the energy of the laser pulses.

To investigate the effective potential acting on polaritons during the two-beam excitation experiment, energy-resolved photoluminescence maps in real space (Figure 5.11) were measured. The slit of the spectrometer was positioned along an axis that intersected the centers of both condensation sites. Measurements were performed for the same excitation powers as used in Figure 5.9. In panels (a), the first condensation site was excited with increasing pulse energy, while the second pulse energy remained constant. In the first panel, the excitation power of the first beam is lower than that of the second. For such parameters, two spatially separated emission lines of different energy were observed. Quasiparticles excited with lower excitation power had lower energy. Increasing the energy of the first pulse resulted in an increase in the occupation of the first condensate, and eventually in a blueshift at the excited site and a reduction in the potential barrier between the condensates. A further increase of excitation power led to an increase of particle density and resulted in an even greater interaction-induced blueshift. In the third panel, the potential increased enough to level the barrier between the two condensates, and an efficient flow of polaritons was allowed. The emission from the second condensate was stronger than that from the first condensate as a result of the flow of polaritons. For higher excitation powers, line broadening and potential equalization were observed at the excited places. Increasing the excitation power caused a significant increase in the emission from the first condensate, and the same effect was observed on a smaller scale for the second condensate.

Figure 5.11(b) corresponds to the excitation of the first condensation site with constant pulse energy and the second condensation site with increasing energy. In the first panel, the first condensation site is higher energetic than the second one. The increase of the excitation power in the second condensation site resulted in a blueshift of the second condensate. At a pulse energy of 1.58 pJ the highest intense lines in both condensation sites were aligned in energy. Above this energy, the blueshift was the same for both condensates.

The energy differences presented in Figure 5.9 correlate with the emission intensities. At the low power regime, the higher energetic condensate was more intense. At enough large excitation power, the polariton flow was observed from

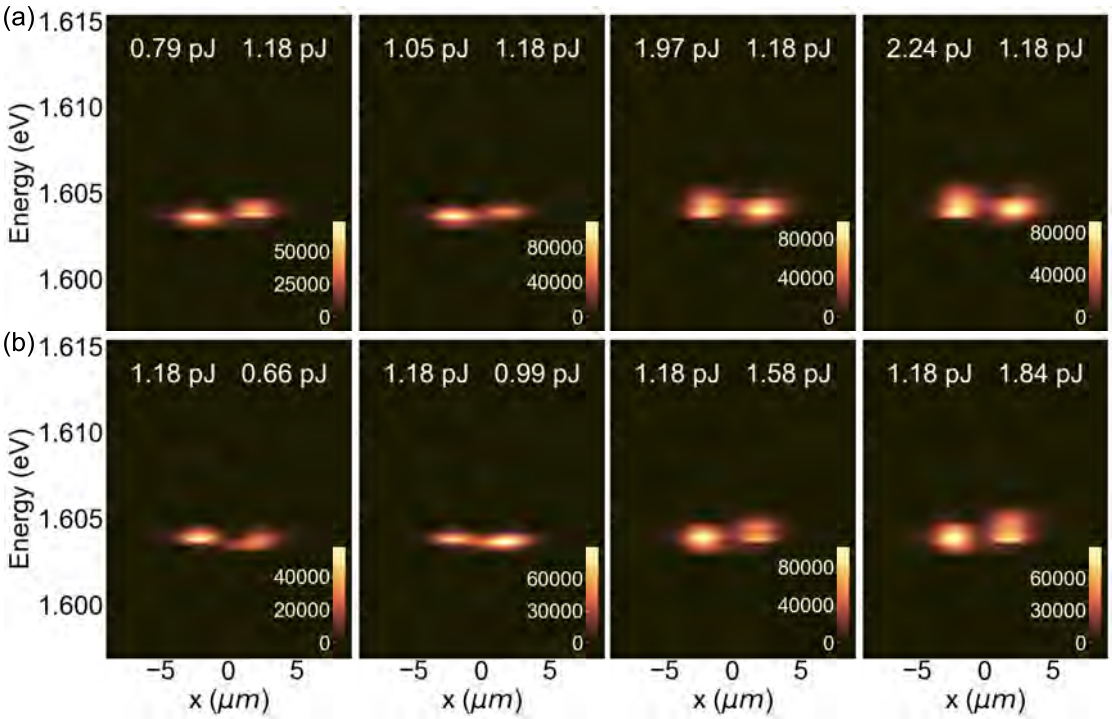

Figure 5.11: **Energy of simultaneously excited condensation sites.** Real space energy resolved maps of emission from the two condensation sites. Top left (right) annotations illustrate the pulse energy of the laser exciting the first (second) condensation site. Color scales give information about the intensity of emission on each panel.

the blueshifted condensation site and abrupt change in the emission intensity. The results presented above confirm that the photonic potential can be modified in both condensation sites. The direction and size of the polariton flows between the condensates can be controlled by the energy of the laser pulses.

5.3 Interference patterns of flowing polaritons

In this chapter, we considered a potential configuration that forces the polaritons to flow simultaneously from the two excited sites. An analogous potential landscape has been achieved on GaAs samples by injecting repulsive interactions with the external laser [94, 95]. The group of Prof. Pavlos Lagoudakis successfully applied it for the ballistic coupling of polariton condensates [88, 89, 96]. We made use of the random distribution of the photonic potential and the intrinsic potential shape to study opposite flows of polaritons.

We performed nonresonant pulsed excitation of two spots spatially separated by 3 µm. The two pulse beams simultaneously excited the two different condensation sites with the same power. The laser beams excited the sample at zero wave vector to avoid injecting any additional momentum to polaritons. The real space emission maps for different excitation powers are presented in Figure 5.12. For a small pulse energy, we observed polariton emission from the excited spots. At higher excitation power, condensation occurred in the local minima. We observed a narrowing of the emission in spatial dimensions and an increase in the intensity of the emission. Interestingly, at an energy of 2.6 pJ of each pulse, the fringe between

the condensates appeared. The interference pattern remained at larger excitation power and even increased its intensity. The fringe is a result of interference between the two polariton waves propagating between the condensates.

We performed an analog experiment on the same position on the sample that is exciting at only one site at a time. The emission maps presented in Figure 5.13(a-e) were measured only for excitation of the first condensation site. We observed the emission from one spot for all the measured pulse energies of the laser. At the same time, there were no signs of interference. Similar conclusions can be drawn from the Figure 5.13(f-j) where the sample was excited with the second excitation beam only. We observed the emission from the excited place in the whole range of measured powers. At high pulse energies, the localization in local minima was observed, but again there was no evidence of the interference fringes.

We performed measurements of the emission under the same conditions in reciprocal space to gather information about the momentum of the particles. The energy-resolved maps in the momentum space for different pulse energies in the two-pulse experiment are presented in Figure 5.14. Excitation with pulses of energy

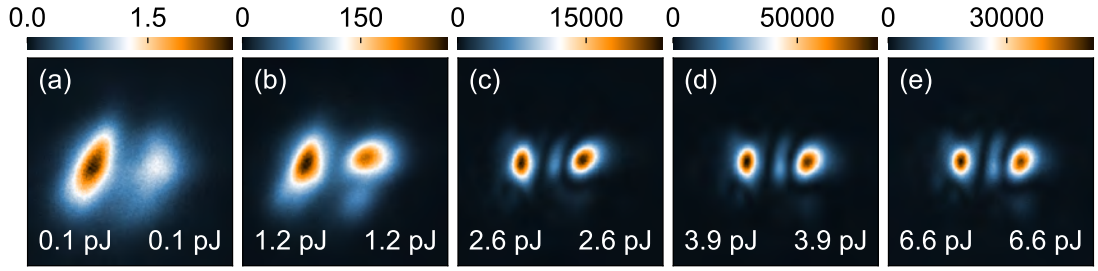

Figure 5.12: **Formation of fringe pattern between two condensates in real space.** (a-e) Real space emission maps for different pulse energies. Bottom annotations show the energy of the first (left) and second (right) pulse. Color bars above each panel indicate the color scale.

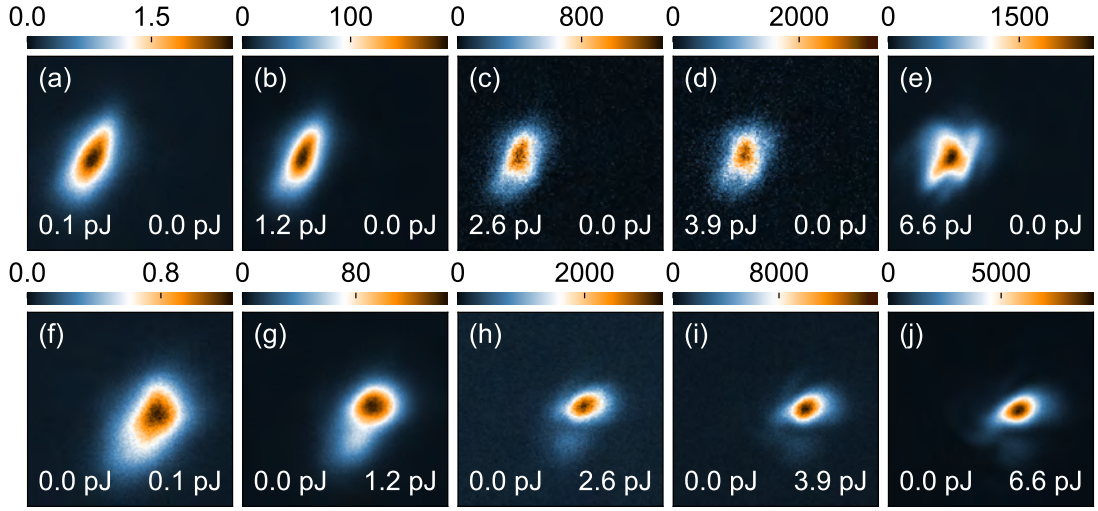

Figure 5.13: **Real space characterisation of condensation sites.** Real space emission maps for different pulse energies of the laser beam exciting the (a-e) first and (f-j) second condensation site. Bottom annotations show the energy of the first (left) and second (right) pulse. Color bars above each panel indicate the emission intensity.

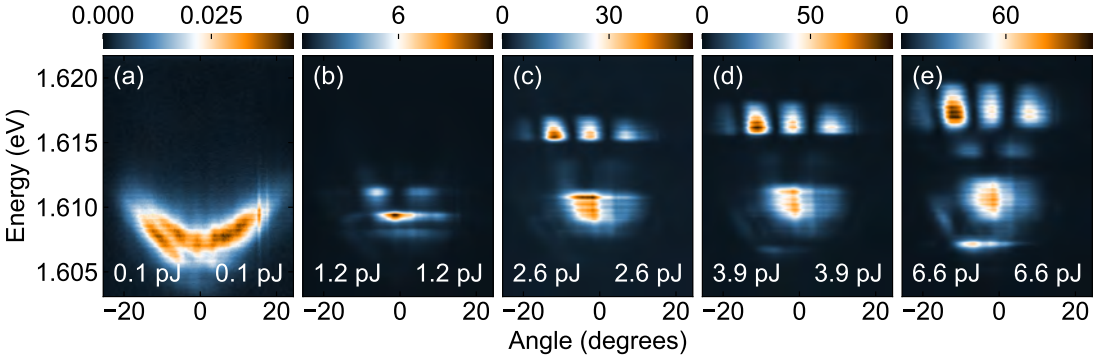

Figure 5.14: **Fringe pattern between two condensates in dispersion relation.** (a-e) Energy-resolved emission maps in reciprocal space for different pulse energies of exciting laser. Bottom annotations show the energy of the first (left) and second (right) pulse. Color bars above each panel indicate the emission intensity.

of 0.1 pJ resulted in the populating of the lower polariton branch. We observed homogeneous occupation of the dispersion in the full range of accessed wave vectors. The pulses energy of 1.2 pJ was sufficient to reach a condensation threshold and macroscopically occupy higher localized states. Because of the rich photonic potential, condensation occurred in many localized states. However, for higher pulse energies, the dominating effect observed on the spectra was an interference pattern at an energy of about 1.616 eV. This pattern corresponds to the opposite flows of particles from the two excited condensation sites. With increasing excitation power, the number of fringes does not change. In this case, the mode parity was even, which means in-phase synchronization between the condensation sites [96].

We studied the angle-resolved photoluminescence for excitation of the same system with single beams separately. The results are illustrated in Figure 5.15. We observed the lower polariton dispersion while exciting the sample with the small pulse energy of the first beam. For higher excitation power, higher states were populated. The following panels show that the dominant part of the polaritons have a nonzero angular momentum. This was another strong indication of polariton flows from the excited condensation sites. However, there was no interference fringes as observed in Figure 5.14.

Full information about the momentum of the particles was collected in the experiment performed in reciprocal space on the CCD camera. We measured the emission in the two-pulse experiment for the same pulse energies as before. The energy-integrated emission maps in the momentum space are illustrated in Figure 5.16. The observed signal is limited in angles by the numerical aperture of the objective that collects light from the sample. For the ideally homogeneous photonic potential, we expect a uniform distribution of the signal on the circle, manifesting equal occupation of all states. In our case, the inhomogeneous potential significantly changes the distribution. For the low excitation power (panels (a, b)), the emission was the highest at the negative angles. The qualitative change was observed at the pulse energy of 2.6 pJ where four interference fringes covered the reciprocal space. The direction of the fringes was correlated with the position of the condensates. At higher pulse energies, only the emission intensity from the fringes changed.

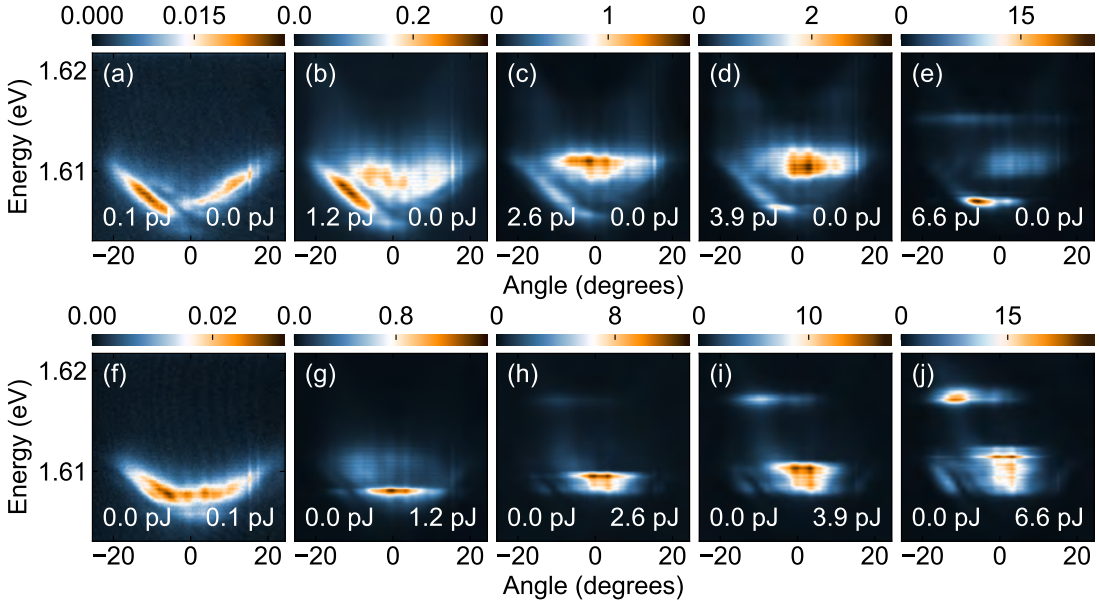

Figure 5.15: **Characterisation of condensation sites in dispersion relation.** Energy-resolved emission maps in reciprocal space for different pulse energies of the first (a-e) and second (f-j) laser beam. Bottom annotations show the energy of the first (left) and second (right) pulse. Color bars above each panel indicate the emission intensity.

The one-pulse experiment revealed the momentum of the particles flowing from each excited condensation site. For the first beam excitation [Figure 5.17(a-e)] the majority of the created particles had a nonzero momentum. At low excitation power, there was a preferred direction of particle flow that manifested itself in emission at negative angles. With increasing pulse energies, the favored momentum was changing and the particles propagated mostly in the horizontal direction. For the second beam excitation [Figure 5.17(f-j)] the emission was comparable at low excitation power. However, for higher pulse energies, polaritons started to propagate mainly to the left. Clearly, the force acting on the polaritons, which is proportional to the potential gradient, had an opposite sign in this case.

The results presented above show that we have two flows in opposite directions

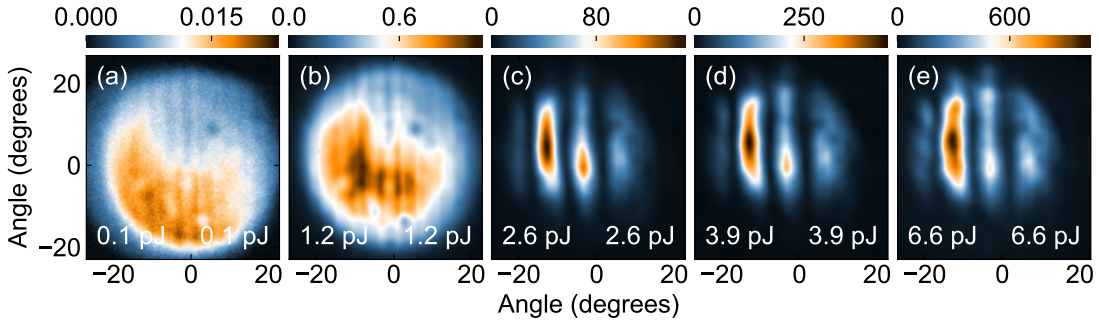

Figure 5.16: **Fringe pattern formation in reciprocal space.** (a-e) Emission maps in reciprocal space for different pulse energies of exciting laser. Bottom annotations show the energy of the first (left) and second (right) pulse. Color bars above each panel indicate the emission intensity.

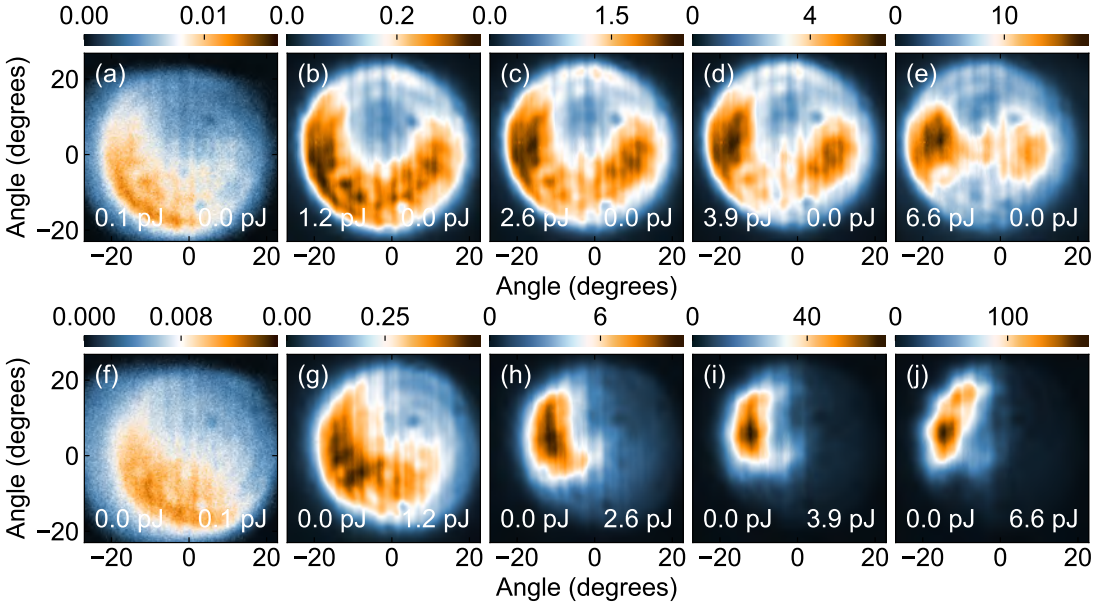

Figure 5.17: **Momentum space characterisation of condensation sites.** Emission maps in reciprocal space for different pulse energies of the (a-e) first and (f-j) second laser beam. Bottom annotations show the energy of the first (left) and second (right) pulse. Color bars above each panel indicate the emission intensity.

between the two excited condensation sites. Both polariton waves interfere with each other, giving a fringe pattern. In the following, we tried to characterize the observed effect in more detail and see if it can be controlled. We performed studies of the emission of created system as a function of the delay time between the pulses. Figure 5.18(a-e) presents real space emission maps for different delays between the pulses exciting different condensation sites. The pulse energy of the two beams was 6.6 pJ each. When the pulses approached the sample at the same time, emission from the two condensation sites and from the single fringe between them was observed. Introducing a time delay of 12 ps between the pulses resulted in a change of the relative emission intensity from the condensates and the fringe. This change was not symmetric, and for the negative delay (when the second pulse excited the sample before the first pulse), the fringe was more intense than for the positive delay. The asymmetry was even more pronounced for a longer delay. For a time delay of −54 ps, the interference was still present, but for a time delay of 54 ps it was quenched. The observed asymmetry was a consequence of the inhomogeneous potential acting differently on each of the excited sites. The angle-resolved emission revealed that depending on the position on the sample, the flow of polaritons from the condensation site can be different. As a consequence, depending on the photonic potential, the fringe pattern can be observed for a different range of the delay times. However, evidence of interference was evident for time delays longer than the length of the laser pulse (being of about 4 ps). This confirmed that the fringe does not originate from the laser beams interference (despite filtering them with the long pass filter). We measured angle-resolved emission maps for the same delays between pulses of 2.2 pJ [Figure 5.18(f-j)]. For a delay time of −54 ps we observed a strong signal in the region of low energies. Above that region, fringes were observed at two energies. For a shorter delay, the fringes were more

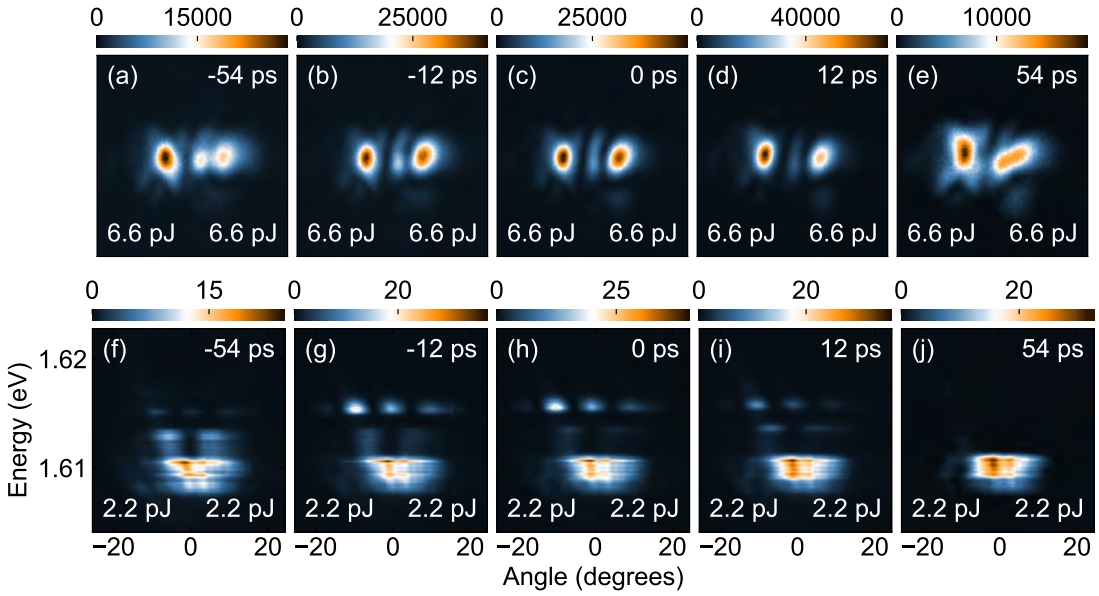

Figure 5.18: **Fringe pattern in time-delayed experiment.** Emission maps in (a) real space (b) momentum space for excitation with two beams of pulses delayed in time. Bottom annotations show the energy of the first (left) and second (right) pulse. Top annotation illustrates the time delay between the pulses. Color bars above each panel indicate the emission intensity.

pronounced. In these results, emission asymmetry was also observed with respect to the delay time, and at 54 ps, the fringes were not visible.

The asymmetry in fringe pattern formation was expected to be controlled by exciting the two condensation sites with different pulse energies. For this reason, we studied energy and momentum resolved emission maps for excitation with different powers of the pulses exciting different sites. The consecutive panels in Figure 5.19(a-e) show the emission maps for the increasing excitation power of the first beam and the fixed power (6.6 pJ) of the second beam. No interferences were observed for first pulse energies of 0.1 pJ and 1.2 pJ. However, for a higher excitation power of the first pulse, the fringe was present between the condensation sites. With increasing power, the width and occupation of the fringe increased. Panels (f-j) correspond to the emission maps for the fixed excitation power of the first beam and the increasing power of the second beam. When the excitation power of the second beam was significantly lower, only the emission from the first site was observed. At the pulse energy of the second beam of 1.2 pJ we already observed the fringe pattern. This confirms that the particles flow between the excited sites is more efficient from the position excited with the first beam. The fringe contrast was the most visible for the pulse energy of the second beam 2.6 pJ. For larger excitation power, the interactions remained, and emission from two condensates and a single fringe was observed.

The influence of the excitation power on the fringe pattern formation was even more pronounced in results of photoluminescence measurements in a reciprocal space. We performed studies of the emission in momentum space for a constant pulse energy of one of the beams and an increasing pulse energy of another one. For low energy of the first pulse and large excitation power of the second pulse [Figure 5.20(a)] we observed flow of the particles along the axis defined by the

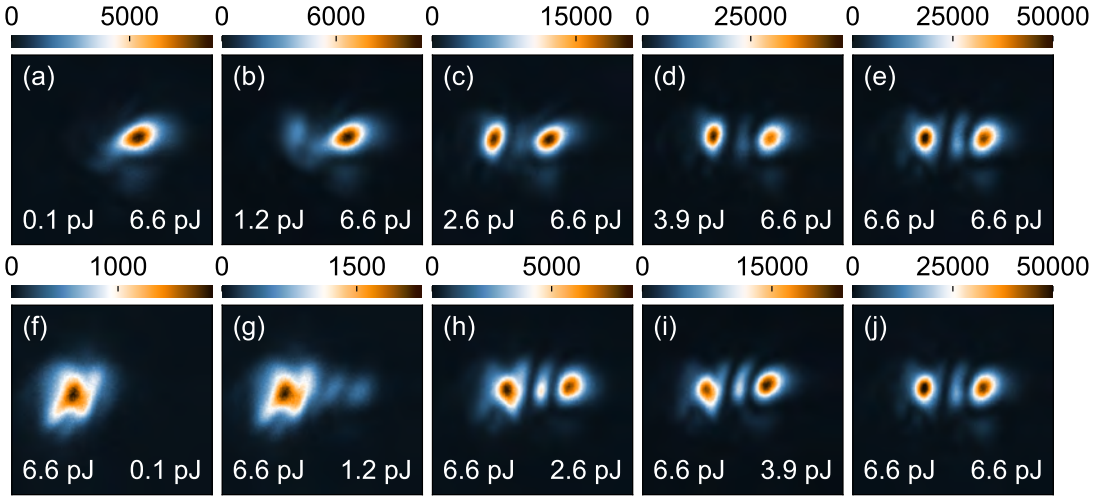

Figure 5.19: **Real space emission for asymmetric excitation.** Real space emission maps for different pulse energies. Bottom annotations show the energy of the first (left) and second (right) pulse. Color bars above each panel indicate the emission intensity.

two condensation sites. However, the polaritons flowed in both directions from the second condensation site. At higher excitation power of the first pulse, we observed formation of fringes and a change in their occupation [Figure 5.20(b-e)]. Interestingly, the position of the fringes changed with the excitation power and the highest intense fringe was moving towards the lower angles. This means that by changing the relative energy of the pulses exciting the condensation sites, one can tune the phase change between the polaritons moving in opposite directions by modifying their potential. This conclusion can also be drawn on the basis of

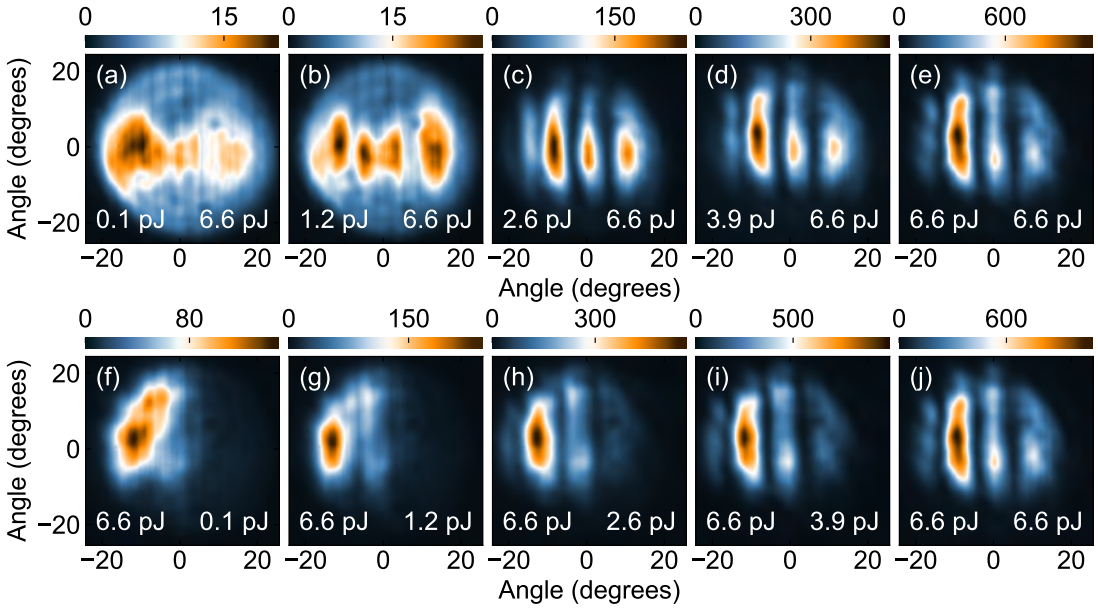

Figure 5.20: **Momentum space emission for asymmetric excitation.** Emission maps in reciprocal space for different pulse energies. Bottom annotations show the energy of the first (left) and second (right) pulse. Color bars above each panel indicate the emission intensity.

the results presented in Figure 5.20(f-j). At low pulse energy of the beam exciting the second condensation site, there is a strong occupation of high momentum states. With increasing excitation power of the second beam the fringe contrast is increasing, but also the position of the fringes changes. Again, the fringe of highest emission intensity moves towards smaller angles. This is clear evidence of potential and polariton phase modification using an external laser.

5.4 Summary

In this chapter we considered the influence of the photonic potential on the properties of exciton polaritons and its application in creating a nonlinear system.

In Sec. 5.1 we presented typical potential inhomogeneities on measured samples. We characterized the distribution of the defects and confirmed that the photonic potential has the greatest influence on negatively detuned polaritons. We showed that condensation occurs in discrete states due to localization in potential minima.

In Sec. 5.2 we considered a system with two condensates with a small potential barrier between them. We observed a flow of polaritons between them, leading to a nonlinear change in the emission intensity at both condensation sites. The polariton flow was induced by the energy blueshift exceeding the potential barrier at a sufficiently large excitation power of the laser.

In Sec. 5.3 we discussed the properties of the system with two opposite flows of polaritons between the two condensates. We observed a fringe pattern, which is a signature of interference between polaritons flowing in opposite directions. We have shown that the interference can be modified by changing the relative excitation power in condensation sites or by changing the time delay between the pulses driving the condensation sites.

The rich potential landscape provides strong modification of polariton properties and, if properly used, can lead to strong nonlinear responses. The analyzed photonic potential configurations were used to create condensate arrangements with nonlinear changes in the emission intensity. We obtained an energy efficient source of nonlinearities that can be easily implemented in a variety of neuromorphic computing applications.

Chapter 6

Low-dimensional structures etched using focused ion beam

One of the key parameters in neuromorphic computing is energy efficiency [97]. It can be determined for any system by measuring the energy required to perform a single operation. Improving the energy efficiency can, therefore, be achieved by reducing the energy needed to obtain nonlinear effects. One way to achieve this is to lower the condensation threshold.

In this chapter, we localize exciton polaritons in low-dimensional structures to decrease the condensation threshold. Typically polaritons are trapped in a micropillar structures [98, 99]. For single micropillars the nonlinear effects such as polariton lasing or condensation have been observed [100, 101]. We show that not only condensation is possible, but the excitation power of the laser needed to reach the condensation threshold is lower for micropillar than for planar structure. What is important, the modification of the potential does not affect the magnetic properties of polaritons. In particular, the synthetic magnetic field is preserved.

6.1 Etching of single micropillars

In this section, we show the procedure to obtain high quality micropillars in a reasonable time. We used the FEI Helios Nanolab 660 Focused Ion Beam (FIB) and Scanning Electron Microscope (SEM) with built-in software "xT microscope Control". The system allows for high-precision etching using a beam of gallium ions. The electron beam ensures high-resolution imaging. Imaging can also be performed with an ion beam, which allows images of the sample to be obtained with a quality that is superior to that of electron imaging, but leads to sample degradation. We will demonstrate the efficient way to create high quality single pillars. We developed a method that allows for precise etching, guaranteeing a structure with a given shape and spatial dimensions. The procedure is mainly based on the control of the etching speed, which is controlled by the beam current. The beam current determines how much the sample surface is damaged by the ion beam. This value should be as low as possible if one wants to etch the structure with high accuracy. However, a low current significantly increases the etching time. The total time of the etching process should be limited mainly for two reasons: during the etching process, the surface of the sample is charging, which can lead to slight movement of the whole sample and spoiling the process; the ion beam

sustains a stable mode for up to 8 hours. To minimize the first problem, one can focus on minimizing the charging effects by grounding the sample to the holder, e.g. using conductive glue and holder. The second problem is an intrinsic property of the machine and cannot be avoided.

To prove the effectiveness and repeatability of the method, we will present the etching process of nine micropillars having diameter of 4 µm, 4.5 µm and 5 µm. We divided the etching into three steps. In a first step, we etched nine rings with an outer diameter of 30 µm. The detailed inner and outer diameters of each ring are presented in Table 6.1. The etched rings were given using built-in software. The first stage of the etching process gives micropillars with diameter 5 µm larger than the target diameter. This procedure is performed to optimize the ratio of the quality of the cut structures to the time spent on cutting. The FIB should not work for too long, because after a longer time (approx. 5 h) the stability of the ion beam decreases significantly, which substantially affects the quality of the etching. The current can be increased to speed up digestion, but this also reduces the precision of the device. Therefore, usually a high beam current is used to cut the surface around first at the beginning and then taper the pillar with a smaller current.

The first stage of the etching process gives micropillars with diameter 4 µm larger than the target diameter. This procedure is expected to be performed with a relatively large beam current (in this case 4 nA) to decrease the time spent on the etching process. However, it should be remembered that for a beam current that is too large, the precision of the etching process will be significantly reduced. Therefore, a large current is set in the first step of the process to remove most of the material, and then the structure is tapered in the subsequent steps with a smaller current. Usually, only the top DBR is etched to avoid destroying the cavity and the quantum wells while preserving the localization effects [102, 103]. In this case, the etching depth was much greater than the width of the cavity. Deep etching allowed us to investigate the quality of the entire structure after the process and ensure that there was no emission from the neighborhood of the pillar. The result of the first etching process is illustrated in Figure 6.1(a). We etched nine pillars with diameters of 8 µm (top) 8.5 µm (center) and 9 µm (bottom). Each of the micropillars had a rather rough surface and a rounded tip due to the high current used in etching. On the edges of the etched rings we observed amorphous material, seen as a white border. It forms when exposed to heat and is observed

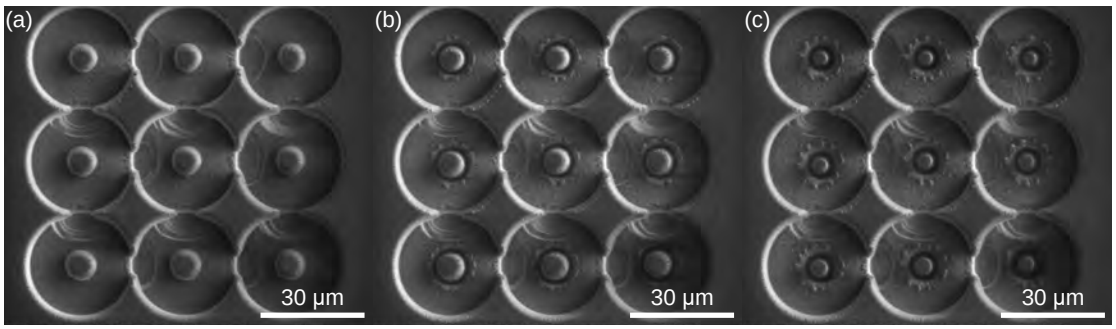

Figure 6.1: **Three-step etching process.** Scanning electron microscope image of the sample surface after (a) first (b) second and (c) third step of ion etching process. Scale bar shows scale on each panel.

only on structures etched with a large beam current. We also observed areas with amorphous material on the top or left side of the etched rings. The pillars were etched in order from left to right and from top to bottom. The diameters of the etched rings were the same as the distance between their centers. The pattern obtained results from the order of etching of the individual pillars.

The second stage of the etching process was used to narrow the diameter and improve the smoothness of the obtained micropillars. For this purpose, we etched a pattern with rings having smaller inner and outer diameters, but partially overlapping the etched surface. It is crucial to set the outer diameter larger than the diameter of the micropillar to ensure that all material except the pillar will be removed during the process. Introducing the overlap also increases the chance that all material except the micropillar will be etched even if the sample moves during the process due to charging. The diameters set in the second process are given in Table 6.1. The beam current was set to 0.9 nA giving higher accuracy than in the previous step. The result of the second etching process is presented in Figure 6.1(b). The micropillars were thinner and with less rounded tip. Once again, the depth of etching was set to 1 µm what resulted in even deeper hole in the area etched in the first step. We also observed residual material that remained after the process and was located outside the pillar.

Table 6.1: The diameters of the micropillars in the individual steps of the etching process.

	Micropillar 4 µm		Micropillar 4.5 µm		Micropillar 5 µm	
	Inner	Outer	Inner	Outer	Inner	Outer
Step 1	8 µm	30 µm	8.5 µm	30 µm	9 µm	30 µm
Step 2	7 µm	9 µm	7.5 µm	9.5 µm	8 µm	10 µm
Step 3	4 µm	7.5 µm	4.5 µm	8 µm	5 µm	8.5 µm

In the third step, the beam current used was reduced to 90 pA and the etching depth was changed to 0.5 µm. This process was the slowest, but also the most accurate. The inner diameters were set to the target diameters of the micropillars. The outer diameters were 0.5 µm larger than the diameters of the micropillars after the second etching step. The three steps were carried out for the dwell time of 15 µs and accelerating voltage of 30 kV. The top view of the final result is illustrated in Figure 6.1(c). We obtained nine straight micropillars that had desirable diameters and a direction perpendicular to the surface of the sample. The whole process took less than three hours.

Within this method, one can produce single micropillars having diameter down to 2 µm. The capabilities of this procedure are presented in Figure 6.2. We are reaching the limits of the smallest diameters in the Figure 6.2(a). Here, the cross sections at depth of distributed Bragg reflectors and cavity have the same diameter. Below the bottom DBR the width was larger due to the smaller etching depth set in the third process stage. The quality of the micropillars was even better for larger structures. We present micropillars with diameters of 3 µm, 4 µm and 5 µm in Figure 6.2(b). The surface and sidewalls of the pillars were smoother for larger structures. The more detailed picture of the etched micropillar structure is presented in Figure 6.2(c). This panel shows ion beam imaging of the exemplary single pillar. Using ion beam imaging we were able to investigate sidewalls in more detail. We observed single layers that create DBRs, cavity, and buffer layer. There

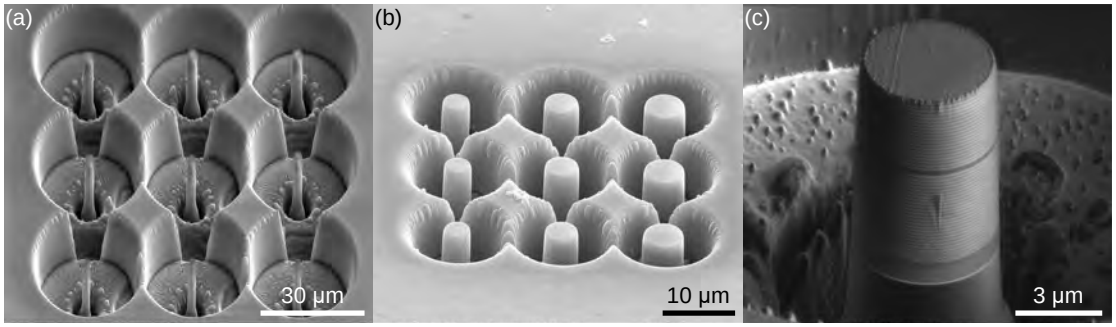

Figure 6.2: **Micropillars etched using Focused Ion Beam within the three-step procedure.** (a) Scanning electron microscope image of micropillars with diameter of 3 µm (top) 2.5 µm (center) and 2 µm (bottom). (b) SEM images of single micropillars with diameter of 3 µm (left) 4 µm (center) and 5 µm (right). (c) Ion beam image of a 4.5 µm diameter single pillar. Scale bar shows scale on each panel.

was no amorphous material on the sidewalls, which tells us that we used a beam current that was low enough in the last step of the etching process. We observed a defect on the bottom DBR that propagated through the structure. The surface of the pillar was unchanged compared to the sample surface before etching. There were inhomogeneities smaller than 200 nm at the edges of the surface that could be removed by using a lower current in the last step. However, the whole structure was good enough to expect localization effects and narrow emission lines.

Etched micropillars should be handled with extreme delicacy as they are very fragile. It should be noted that the DBRs in the considered samples contain a large amount of magnesium. Micropillars have an increased surface to volume ratio. After the etching process, magnesium reacts more efficiently with the oxygen present in the air; therefore, long storage of micropillars under ambient conditions increases the risk of their breakage. This case is presented in Figure 6.3(a). We observed a broken pillar after long exposure (1 h) to air. The problem of micropillar breaking can be easily resolved by keeping a sample under high vacuum.

When working with pillars, the effects of laser heating should also be taken into account. Heat dissipation from the micropillar is reduced due to the etched material around it. For this reason, they can be easily burned out with the external laser. The SEM imaging of a burnt micropillar is presented in Figure 6.3(b). Starting from the bottom, a substrate, buffer layer, bottom DBR and cavity were resolved. However, at the very tip, the individual layers of the top DBR cannot

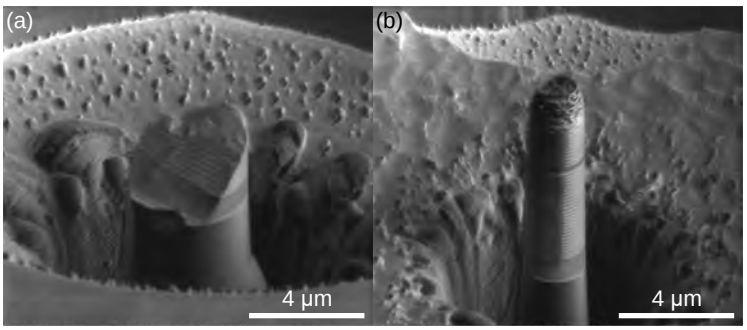

Figure 6.3: **Micropillars sensitivity to environment.** FIB imaging of (a) broken and (b) burnt single micropillar. Scale bar shows scale on each panel.

be distinguished. The upper part of the micropillar was completely burned. The pulse energy needed to destroy the pillar was $0.9\frac{mJ}{cm^2}$. A two orders of magnitude larger power does not damage the sample while exciting a planar structure.

6.2 Emission from micropillars

We performed angle-resolved photoluminescence studies of a single micropillar of 4 µm diameter (Figure 6.4). The upper (lower) panels show emission observed in σ^+ (σ^-) polarization. At low excitation power, the dispersion was composed of discrete states resulting from spatial localization. The emission was similar for each state. The increase of excitation power resulted in larger occupation and dominant emission from the ground state. We also observed a blueshift and broadening of the ground state. The condensation threshold was reached in both polarizations, but the condensate emission intensity was larger in (σ^-) polarization.

We retrieved the intensity, linewidth, and blueshift characteristics for the most intense mode at zero wave vector and illustrate in Figure 6.5. We measured the emission from the single pillar (panel (a)) and the planar structure next to the pillar (panel (b)). In both positions, the condensation threshold was reached. We observed a nonlinear increase of the intensity in both polarizations with the threshold behavior. Below the condensation threshold, the emission intensity in opposite circular polarizations was comparable. Above the condensation threshold, the emission in σ^- polarization was more intense than in σ^+ in the micropillar excitation case. In the planar structure, the σ^+ polarized mode was more intense. The linewidth of the lower polariton mode obtained on a micropillar was four times smaller than that obtained on a planar structure. The condensate blueshift

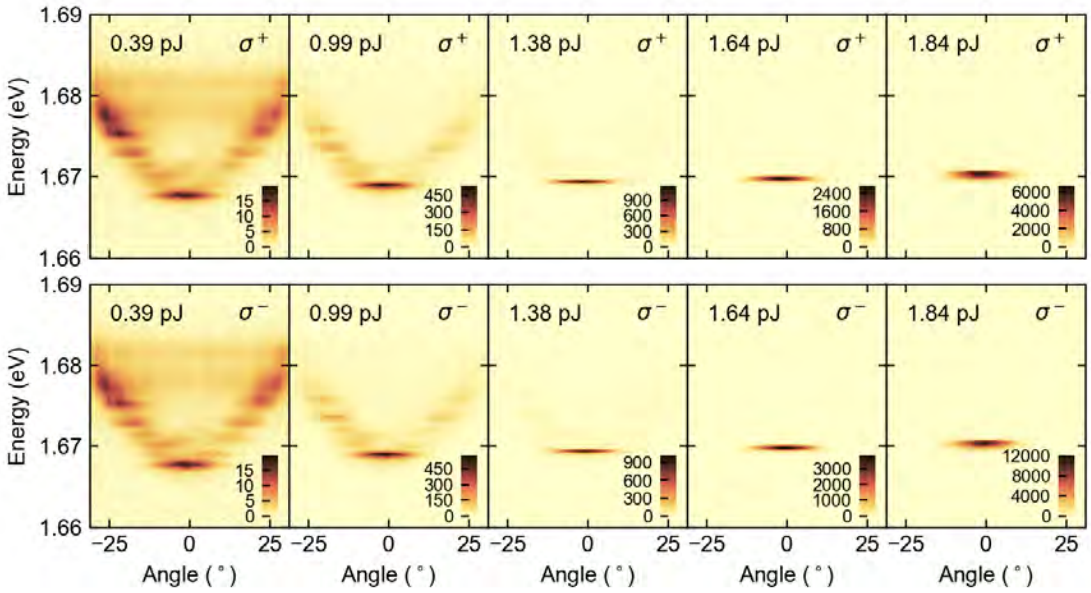

Figure 6.4: **Lower polariton dispersion measured in a micropillar.** Detection polarization and angle resolved photoluminescence maps of lower polariton for different excitation power. Pulse energy of the laser beam and detection polarization are marked in the top left and right corners, respectively. Color scale gives information about the intensity of emission.

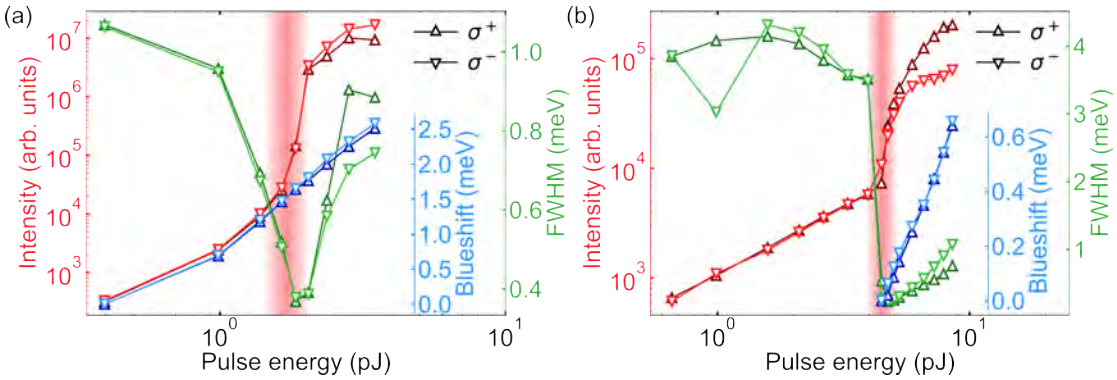

Figure 6.5: **Lowering the condensation threshold in micropillar structure.** Polarisation resolved power dependencies for intensity, blueshift and linewidth of the most intense emission line from the (a) micropillar (b) planar structure. The legend describing the σ^+ and σ^- polarised modes is illustrated in top right corner. Red vertical line shows the condensation threshold.

obtained under micropillar excitation was larger than in the not etched structure. The planar condensate was localized, and its energy was below the dispersion. For this reason, the blueshift was plotted starting from the condensation threshold. The two main conclusions that are drawn are that the effective magnetic field is still present after the etching process, and that the condensation threshold is lowered in the etched structure.

6.3 Spin properties of localized polaritons

We studied the emission from the micropillar in an external magnetic field. We measured six polarization components H,V,D,A,σ^+ and σ^- and calculated the three Stokes parameters of the emitted light. Figure 6.6 shows the change of the components S_1, S_2 and S_3 with pulse energy of the vertically polarized laser in an external magnetic field. All of these components change substantially at the condensation threshold. In the absence of magnetic field, at low excitation power, the polaritons are not polarized. At the threshold, a strong build-up of linear polarization was observed with the dominance of the vertical polarization component. However, an increase of the circular polarization (σ^-) was also observed.

Further increase of the excitation power resulted in the change of linear polarization with a stable S_3 parameter. In the larger magnetic field, the contribution of vertical polarization was greater in a linear regime, but it was decreasing for the emission from the condensate. At the same time, the contribution of the S_2 parameter to the total polarization above the condensation threshold decreased in favor of the S_3 parameter, which clearly increased. The higher the magnetic field, the smaller the influence of the external laser on the resulting polarization of the emitted light. In the magnetic field of 6 T the change of the polarization is observed only at the condensation threshold.

To better visualize the change of the polarization with the excitation power, we plotted the projections of the polarization states on a Poincaré sphere (Figure 6.7). In the absence of magnetic field, with the increasing excitation power, there is a build-up of vertical polarization, and then the slight increase of the σ^-

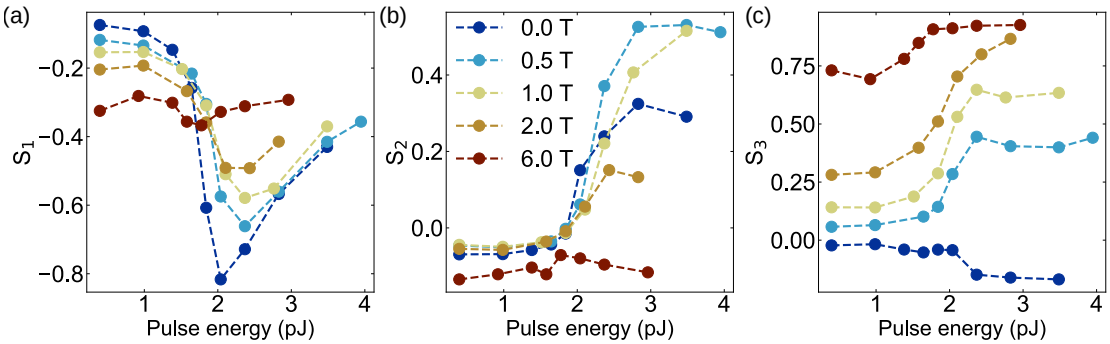

Figure 6.6: **Tuning of spin polarization in a micropillar.** Stokes parameters (a) S_1 (b) S_2 and (c) S_3 of the light emitted from the micropillar structure for different pulse energy of the laser. Magnetic field is marked in top left corner of panel (b).

component. In the magnetic field of 0.5 T, the circular polarization increases with increasing excitation power. Here, already the σ^+ component is more dominant than the σ^- one. Until the condensation threshold is reached, the vertical polarization also increases its contribution to the total polarization state. In larger magnetic field the initial polarization at the lowest measured excitation power has larger σ^+ component. In addition, the build-up of circular polarization is faster with increasing excitation power. The influence of the laser on the S_1 parameter is smaller with the increasing magnetic field.

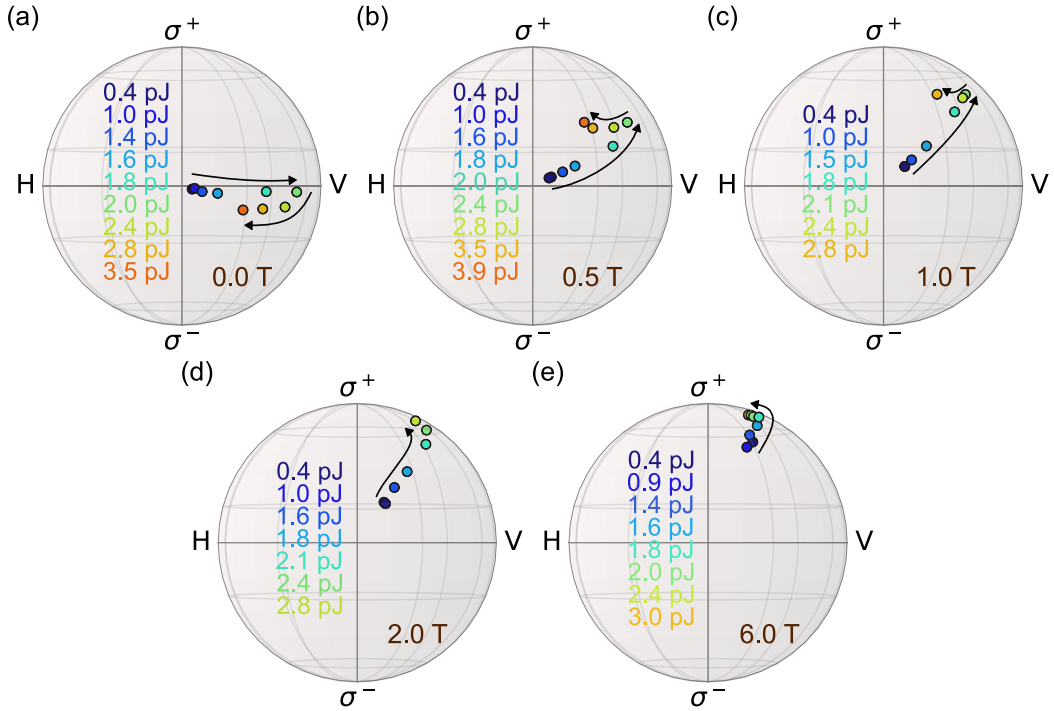

Figure 6.7: **Projections of polarization states on a Stokes sphere for increasing excitation power at different magnetic fields.** The arrows are guide to eye to show the change of polarization state with the increasing excitation power. The pulse energy of the laser is marked on a left hemisphere. Magnetic field is marked in a bottom right.

6.4 Summary

In this chapter, we studied the properties of exciton polaritons localized in low-dimensional structures etched by the focused ion beam. We discussed the phase transition to the condensate and spin properties in an external magnetic field.

In Sec. 6.1 we presented a method for etching single micropillars using focused ion beam etching. We showed that within the three-step procedure micropillars of the desired diameter and high quality can be produced with high repeatability. We discussed the sensitivity of the pillars to the environment and indicated the most common reasons for the destruction of pillars.

In Sec. 6.2 we showed that in the linear regime localization of polaritons results in a quantization of states observed in emission. Above a certain excitation threshold, condensation occurs in the lowest state. We presented the lowering of the condensation threshold in low-dimensional structures in relation to the planar structure.

In Sec. 6.3 we discussed the spin properties of localized polaritons. We showed that the synthetic magnetic field was present in micropillar structures. We found that all the magnetic properties observed in planar structures have been preserved. The tuning of the condensate spin polarization was possible with the use of an excitation laser and an external magnetic field.

Polaritons confined in low-dimensional structures result in localized states of lower threshold while maintaining other properties. The introduced localization allows for building devices with improved energy efficiency in a controllable way.

6.5 Appendix: Etching depth calibration

It is important to be aware of the technical details when etching the structure using a bitmap. The etching process with a bitmap is quite troublesome when one wants to obtain a structure with a very specific depth. The "xT microscope Control" software allows one to load a bitmap and set a specific etching depth, but the resulting depth depends on the size of the bitmap used. To investigate this feature, 14 rectangles with dimensions of 10 µm×5 µm were etched with the etching depth set to 5 µm. The only parameter that differentiated the rectangles was the size of the bitmap with the given structure. The etched rectangles were imaged using a scanning electron microscope and shown in Figure 6.8(a). We observed that rectangles etched with the same beam current have different depth. In fact, the larger the bitmap, the greater the depth at which the structure was etched despite the same parameters set in the program. Based on the SEM images, we were able to determine the depth to which the structures were etched for each bitmap size (Figure 6.8(b)). We observed linear behavior for $px/\mu m \geq 5$. We fit the linear function $y = ax + b$ in this region and obtained coefficients a = 0.6 and b = -3.1. This means that the target depth would be achieved for a bitmap with a size of 13.5 $px/\mu m$. Interesting behavior is observed below this region. We identified three rectangles with an undefined depth. A closer look at these three rectangles is shown in (Figure 6.9). In panels (a-c), we observe SEM images of rectangles etched for the increasing size of the smallest bitmaps used. We observed matrices of spots with increasing density. This allowed us to conclude that the ion beam etches structures in the places specified by specific pixels in the bitmap. When

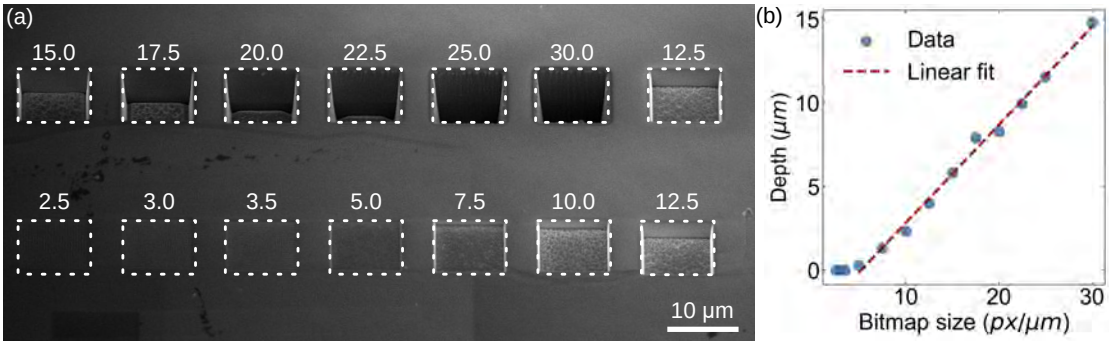

Figure 6.8: **Calibration of bitmap size for ion beam etching.** (a) SEM image of rectangles etched using different bitmap size. Positions of the etched rectangles is marked with the white dashed rectangles. The bitmap sizes (given in $px/\mu m$) used for each structure are illustrated above them. Scale is indicated by the scale bar. (b) Depth of the etched structures as a function of a bitmap size. The linear fit is marked with the dashed line. FIB etching and SEM image were performed by Monika Emmerling at the University of Würzburg.

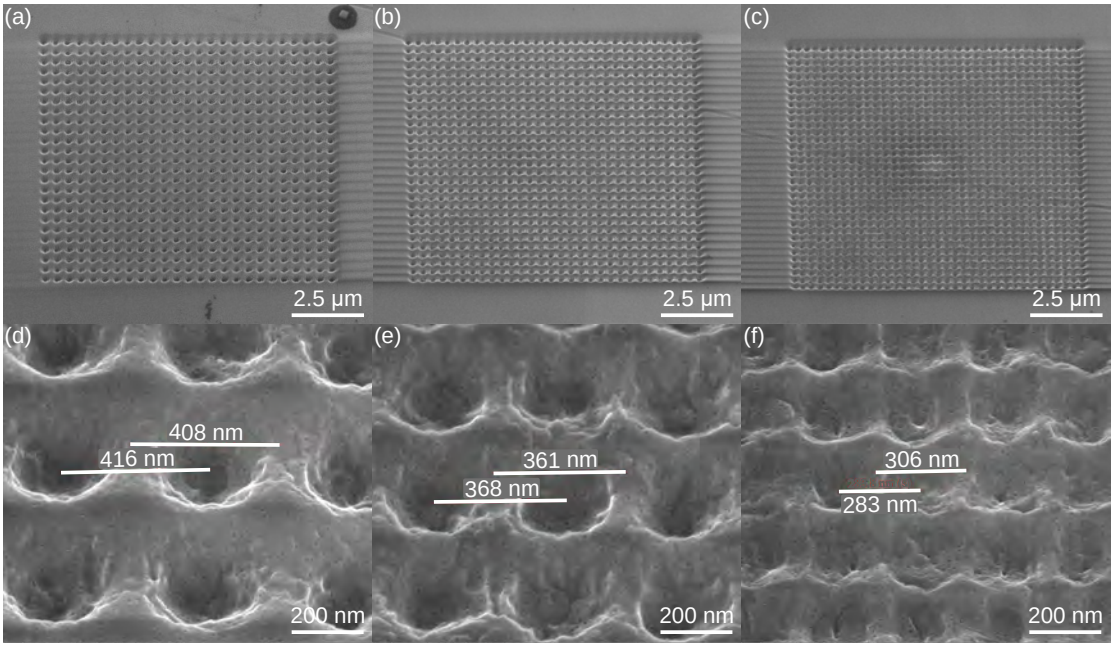

Figure 6.9: **Shallow structures in focused ion beam etching.** SEM image of rectangles etched using bitmap size of (a,d) $2.5\,px/\mu m$ (b,e) $3.0\,px/\mu m$ and (c,f) $3.5\,px/\mu m$. Scale is indicated by the scale bar in the bottom right corner. The calculated distances are marked with the white lines and values. FIB etching and SEM image were performed by Monika Emmerling at the University of Würzburg.

their density is so low that they do not overlap, the etching process is ineffective. To test this hypothesis, the distances between the neighboring holes were measured and compared with the distance between the pixels in the bitmaps. We observed that the measured distances correspond to the calculated values. This means that before etching the structures given by the bitmap, one should first perform depth calibration for the selected beam current value (the higher the current, the larger the holes, and the better overlap).

Chapter 7

Formation of half quantum vortices

Polariton condensates, as states of matter of wavelike nature, have a phase degree of freedom. Phase phenomena have been particularly interesting in terms of observation of superfluidity [104, 105] and quantum vortices [90, 106, 107]. In semimagnetic condensates considered in this thesis, spin degree of freedom is pronounced what allows for observation of half quantum vortices [108] observed only in one circular polarization. Polarization sensitive vorticity has already been observed for spinor condensates [66, 109, 110].

In this chapter, we study formation of quantum vortices using interferometry setup. We show half vortex pairs of opposite topological charges appearing at large enough laser excitation power. We discuss the stability of the half vortices in magnetic field and show signatures suggesting the merging of two half vortices during their annihilation.

7.1 Phase and amplitude retrieval method

A quantum vortex is a perturbation of a system characterized by zero particle density and a phase build-up by 2π around the center of the vortex. Experimental access to quantum vortices can be obtained by studying the amplitude and phase. For this purpose, interferometric measurements were performed. The direct method for the detection of vortices was proposed in 1998 [111]. It relies on creating an interference pattern and analyzing fringes in a real space. The pattern is obtained by overlapping the signal with a plane wave on a detector. Both components can be described as two waves u_1 and u_2 defined by frequency ω, momentum $\mathbf{k}$ and phase φ:

$$\begin{aligned} u_1(\mathbf{r},t) &= a_1(\mathbf{r})\exp^{-i(\omega t-\mathbf{k_1}\cdot\mathbf{r}+\varphi_1)} \\ u_2(\mathbf{r},t) &= a_2(\mathbf{r})\exp^{-i(\omega t-\mathbf{k_2}\cdot\mathbf{r}+\varphi_2)} \end{aligned} \tag{7.1}$$

The interference image observed on the CCD camera is a modulus squared of the sum of both waves:

$$I(\mathbf{r},t) = |u_1+u_2|^2 = |a_1|^2 + |a_2|^2 + \left(a_1 a_2^* \exp^{-i[(\mathbf{k_2}-\mathbf{k_1})\cdot\mathbf{r}+(\varphi_2-\varphi_1)]} + c.c.\right) \tag{7.2}$$

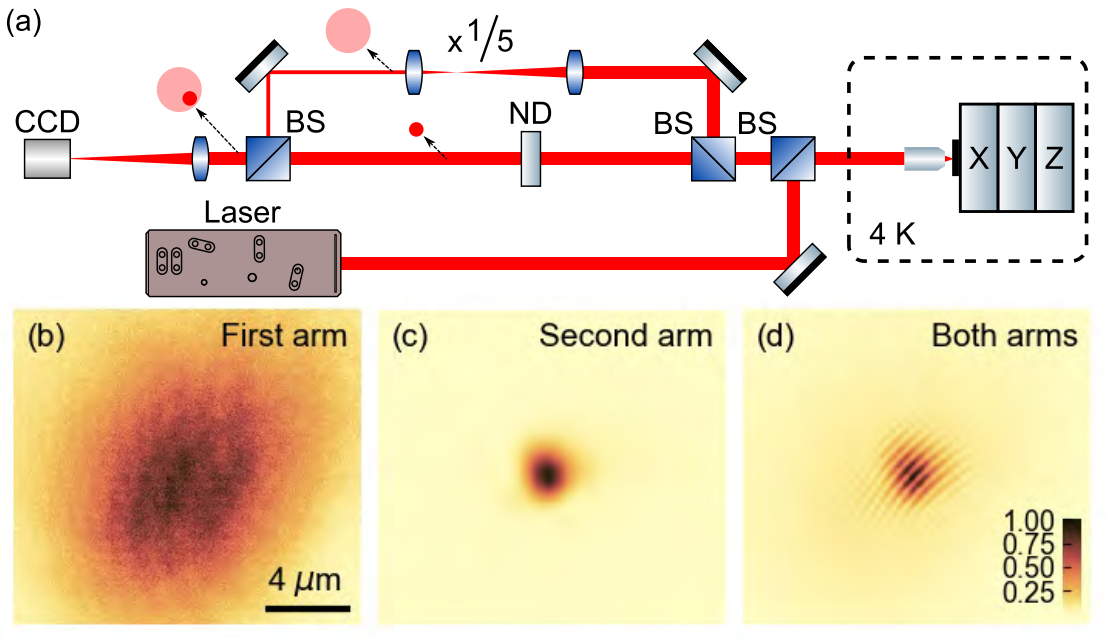

Figure 7.1: **Experimental setup for measuring the vortices.** (a) Scheme of the experiment with the Mach-Zehnder detection setup. The relative size and positions of the signal on each and both arms of the interferometer is indicated with the arrows. (b-d) The normalized intensity of the signal on the first, second and both arms of the interferometer. Colorbar shows color scale for each panel.

The experimental setup used to produce interference patterns is presented in Figure 7.1(a). The pulsed laser is focused with a microscope objective on a sample placed in a cryostat. The emission is collected with the same objective and directed to the interferometer. The beam splitter divides the signal equally into two arms of the interferometer. In the first arm, the beam is expanded five times using a telescope to produce a wave with a reference phase. The second arm contains the delay line to align the pulses in time. Both beams merge on a CCD camera at an angle to obtain interference fringes. The typical signal obtained from both interferometer arms separately and together is illustrated in Figure 7.1(b-d). The expanded beam from the first beam is a source of constant phase. The second arm contains the raw unprocessed signal. Interference between the two beams results in an interference pattern.

An example of a fringe pattern is presented in Figure 7.2(a). It was theoretically calculated as the result of the interference of the field describing two quantum vortices with a plane wave. The interferogram contains fringes and characteristic fork-like dislocations that indicate the positions of quantum vortices. From the fringe pattern, it is possible to obtain the amplitude and phase of the system. For this purpose, spatial filtering is performed using the fast Fourier transform. From the calculated Fourier fransform, a reciprocal map with three peaks is obtained [Figure 7.2(b)]. The center peak corresponds to $|a_1|^2$ and $|a_2|^2$. The remaining two peaks contain complete information about the phase. They are shifted from the center by the vector of length $|\mathbf{k_2} - \mathbf{k_1}|$ and correspond to the last two terms in equation (7.2). One of the side peaks is shifted to the center and the rest of the map is filtered [Figure 7.2(c)]. In the last step, the inverse Fourier transform is performed. From the above procedure, the amplitude [Figure 7.2(d)] and the

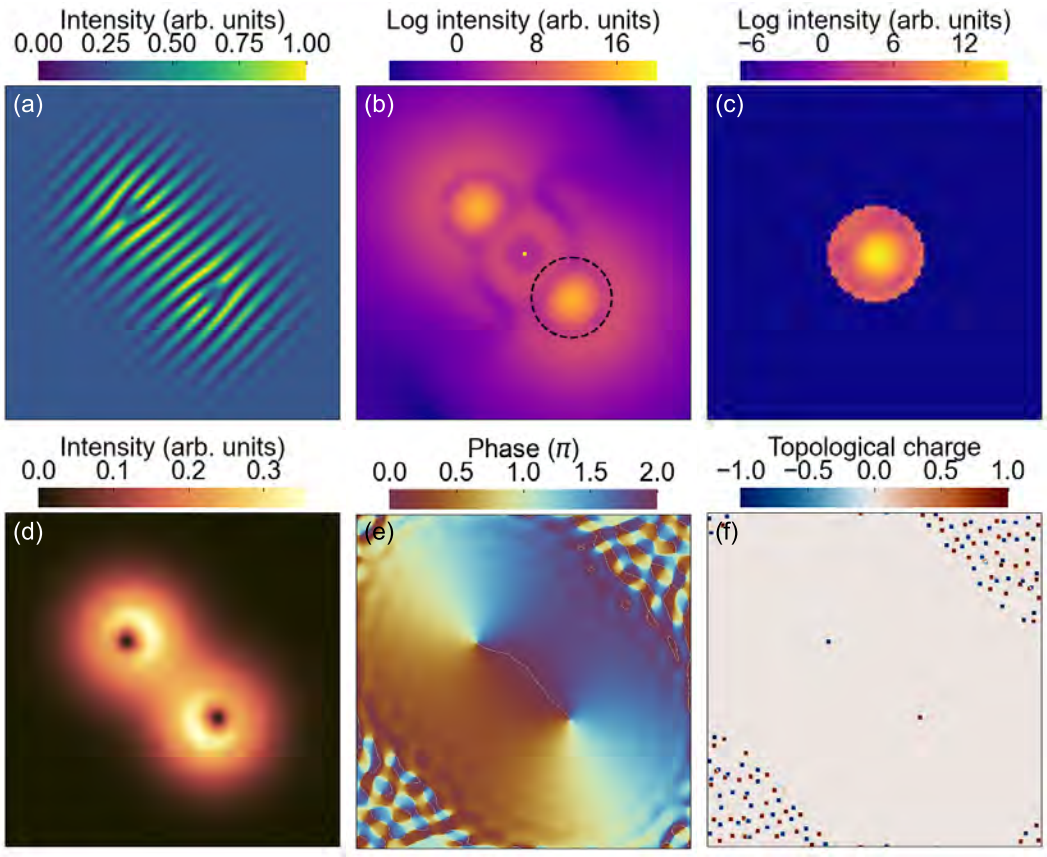

Figure 7.2: **Phase and amplitude retrieval.** (a) Interferogram calculated by interfering the signal of two vortices with a plain wave. (b) Fourier transform of the interferogram. Black dashed circle indicates the peak chosen for further analysis. (c) Filtered fourier transformed signal with translation of the chosen peak to the center of the reciprocal space. The inverse fourier transform of this signal gives the (d) amplitude and (e) phase maps in real space. (f) Topological charge obtained from the circulation calculated from the phase map. Two vortices with opposite topological charges. The nonzero topological charges at the corners of the map are artifacts.

phase of the system [Figure 7.2(e)] are obtained. From the maps, the positions of the vortices can be obtained from the local zero-density regions in the amplitude and the 2π phase change around the vortex center. The phase circulation on the phase map gives information about the topological charge of the vortex. This information can be obtained by calculating the phase circulation, which is defined as an integral of the phase gradient in a closed curve:

$$\Gamma = \oint_C \nabla\Phi \, dl \tag{7.3}$$

where $\nabla\Phi$ is a phase winding, and C is a circle around the vortex core. For quantum vortices, one can define the topological charge l which describes the quantization of the phase winding:

$$\nabla\Phi = 2\pi \cdot l \tag{7.4}$$

The topological charge can have both positive and negative values, and can be determined from the circulation as shown in Figure 7.2(f).

We presented in chapter 4 and chapter 6 the spin effects already observed in the absence of the magnetic field. The broken symmetry between the σ^+ and σ^- components allows studies of half quantum vortices [66]. They exhibit a phase rotation of 2π observed only in one circular polarization and not present in the opposite one.

7.2 Half quantum vortices

In search of vortices, we examined the phase in the condensate formed in the MC-S sample. We excited the sample nonresonantly with a 5 µm diameter laser beam and studied the phase of quantum states of the polariton field for different pulse energy. The formation of vortices with increasing excitation power is illustrated in a Figure 7.3. Panels (a-e) present the phase distribution in a real space revealed from a σ^+ polarized light in the absence of magnetic field. For small excitation power, we did not observe any evidence of vortices. The increase of pulse energy resulted in the creation of two vortices with opposite topological charges. Each vortex has a phase winding of 2π. Both vortices are stable as the excitation power increases. Unfortunately, due to the setup instabilities we were unable to trace the position of the vortices, but we observed that with increasing pulse energy, the distance between the vortices changes. A similar behavior was observed in the σ^- maps [Figure 7.3(f-j)]. For a small pulse energy, we did not observe signs of vortex formation. At higher laser power, two vortices appeared with a smaller distance compared to that observed in σ^+ polarization. In fact, we observed four half quantum vortices, two visible in the σ^+ and two visible in the σ^- polarization. Interestingly, they co-existed in pairs having opposite topological charges. It has been previously shown that the position of the vortices is strongly correlated with the photonic potential what has been previously observed on CdTe samples [109]. In our case, the existence of two pairs of half quantum vortices forming at different

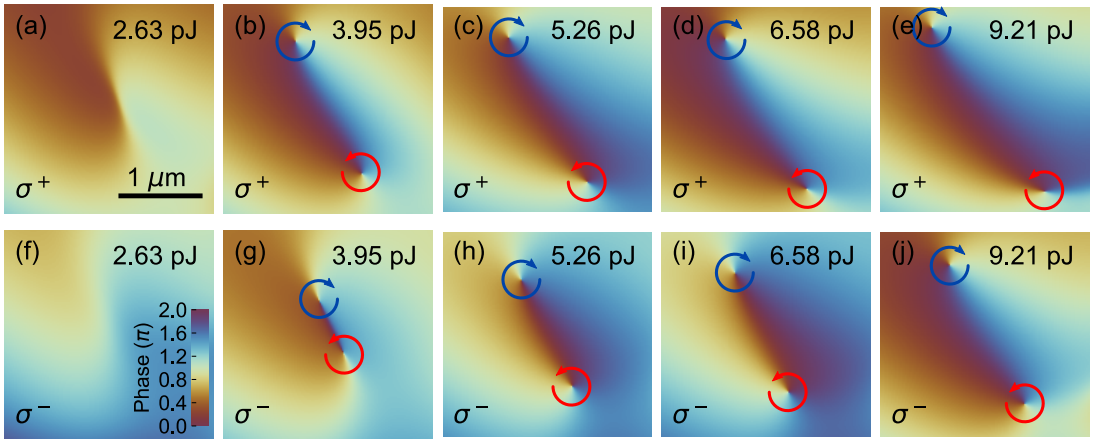

Figure 7.3: **Half vortices formation in the absence of magnetic field.** Phase distribution in a real space for different pulse energy of the laser beam. The pulse energy and detection polarization are marked in top right and bottom left corners, respectively. Blue and red arrows indicate the phase winding around the vortex cores. Scale bar shows the spatial dimensions. Color scale on panel (a) gives information about the phase on each panel.

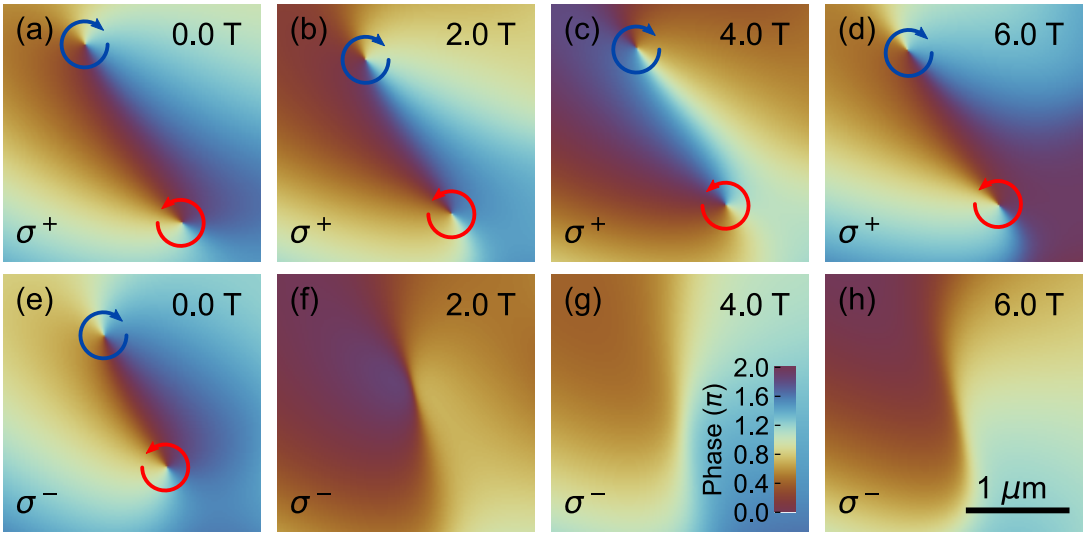

Figure 7.4: **Half vortices formation in magnetic field.** Phase distribution in a real space at different magnetic field for pulse energy of 5.26 pJ. The magnetic field and detection polarization are marked in top right and bottom left corners, respectively. Blue and red arrows indicate the phase winding around the vortex cores. Scale bar shows the spatial dimensions on each panel. Color scale on panel (g) gives information about the phase on each panel.

positions on the sample suggests that the potential is different for the σ^+ and σ^- polariton fields.

We performed measurements of the vortices in the magnetic field, as it introduces additional asymmetry between the σ^+ and σ^- components. We expected to induce the creation or annihilation of half vortices with an increasing magnetic field. Figure 7.4 shows real space phase maps in an external magnetic field for a laser pulse energy of 5.26 pJ. For this excitation power, we observed two half-vortices of opposite topological charges in σ^+ polarization. The 2π phase change around the singularities was observed in the entire range of measured magnetic fields. In opposite polarization, the two vortices were observed in the absence of a magnetic field. The distance between the vortices was smaller than that measured in σ^+ polarized light. In the following panels, the vortices are not present, and up to 6 T there was no evidence of phase singularities.

We performed careful studies of the same position on the sample in a wide range of magnetic fields and excitation powers. From these measurements, we extracted the number of vortices observed in both circular polarisations (Figure 7.5). In clockwise polarization, the vortices appeared at around 3.5 pJ and were stable at larger laser pulse energies. There was no clear dependence of the magnetic field. It is worth noting that the vortices always appeared in pairs. In counterclockwise polarization, we observed two areas where the vortices formed. In general, the formation of vortices in positive magnetic fields was more difficult to obtain in σ^- polarization. To create vortices, higher excitation power was needed in each magnetic field. At 4 T, even a pulse energy above 9 pJ was not enough to obtain the phase transition.

For laser pulse energies and magnetic fields where the vortices were present, we calculated the distance between them and illustrated in Figure 7.6. In panel

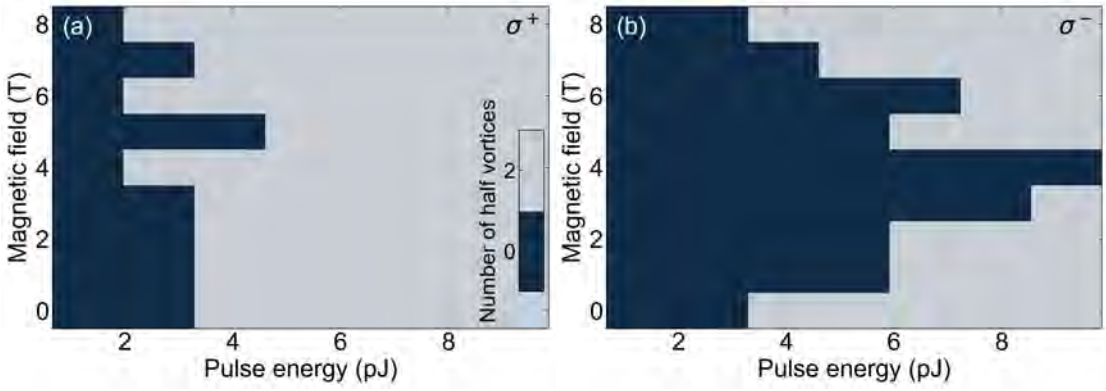

Figure 7.5: **Phase diagram of vortices.** Number of vortices detected in (a) σ^+ and (b) σ^- polarization on the phase maps.

(a) which describes the vortices observed in σ^+ polarization, the distance depends on the excitation power. The vortices were farther away from each other when the pulse energy of the laser was larger. The decrease of excitation power resulted in vortices coming closer to each other. The smallest distances between the vortices were observed for the lowest pulse energies required to create them. The calculated distance between the vortices observed in σ^- leads to similar conclusions, but it can be described from another angle. The distance between the vortices reflects their stability. The annihilation of vortices can be obtained both by decreasing the laser energy pulse or changing the magnetic field towards 4 T. Tuning these parameters leads to a decrease of the distance between the vortices, and finally to the disappearance of them. This suggests that vortices are annihilated when they meet at the same place.

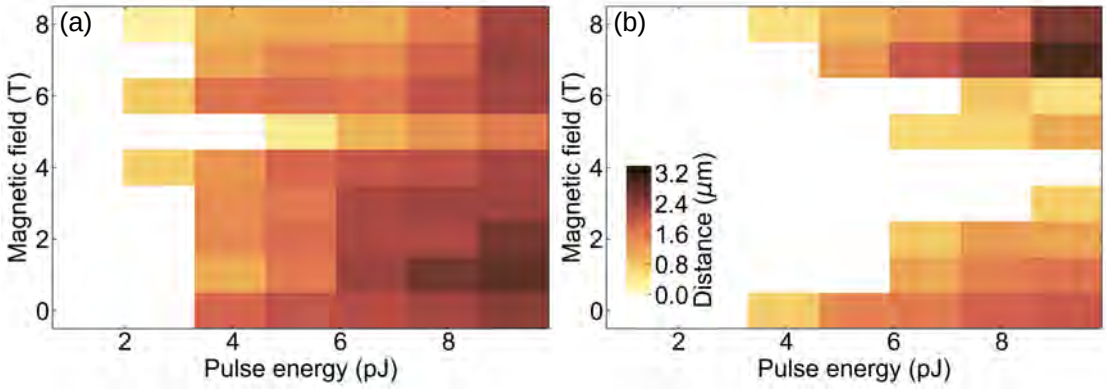

Figure 7.6: **Distance between the vortices.** The calculated distance between the detected vortices in (a) σ^+ and (b) σ^- polarization for different magnetic field and pulse energy of the laser. Color bar on panel (b) gives information about the color scale for the distance on both panels.

7.3 Summary

In this chapter, we studied the formation and annihilation of quantum vortices on a sample.

Sec. 7.1 was dedicated to the procedure to measure and retrieve the spatial distribution of amplitude and phase from the interferograms. We showed the typical experimental setup in the Mach-Zehnder configuration and described the step-by-step process of measuring and detecting the vortices.

In Sec. 7.2 we presented a formation of half vortices in the absence of a magnetic field. We showed that it is possible to create a pair of half vortices with opposite topological charges in both circular polarizations. With increasing excitation power, the created vortices moved away from each other. In an external magnetic field, the annihilation of the half vortices in one polarization was possible. We discussed the stability of the half vortices in a magnetic field and connected it with the distance between the two half vortices of opposite topological charge.

Presented results are a strong indicator that phase-related phenomena can be potentially low-power-consuming sources of strong nonlinearities. The formation and annihilation of half-vortices can be used to construct switches or logic gates with two distinct logic states. The presence of opposite topological charges allows for an increase in the complexity of constructed devices and potentially can facilitate the implementation of more complicated devices in the future.

Chapter 8

Phase build-up induced by polariton-polariton interactions

In photonic systems, nonlinearities required for efficient computation have been implemented from the phase shift between the signals. We expect that the optical phase shift can also be applied to perform nonlinear operations with polaritons. In this case, the neuromorphic computation based on phase shifts is expected to be very efficient, reaching the level of 3 aJ per operation, which corresponds to about 12 photons per pulse [112]. This value is very promising and can allow us to surpass the electronic platforms.

The purpose of this chapter is to check how large phase shifts can be observed in CdTe-based microcavities. We expect to observe the highest nonlinear effects related to the phase change in interferometric experiments. Nonlinearities at the level of a few photons have already been observed in phase shift in polariton condensate in GaAs-based microcavities [113, 114]. The effort to understand these effects pays off, and the topic is beginning to apply, for example, to quantum simulators [47, 115] where the phase synchronization in multi-condensate systems has been achieved [116, 117].

In this chapter, we demonstrate an experimental method for probing the phase changes of resonantly created polariton condensate. We perform transmission measurements with phase detection to look for nonlinear behavior. We show the interferometric method to measure real space phase distribution. We present a method to retrieve the small phase shifts in an unstable experimental setup. Finally, we show the interaction induced phase build up.

8.1 Interaction induced phase build up of polaritons

To study the phase of resonantly injected polaritons, we performed interferometric measurements. The beam that excited the sample was split into two. One part was transmitted through the sample. Another beam, which served as a reference beam, was merged with the transmission signal on a CCD camera. The sample MC-T was excited with a pulsed laser from the back side of the sample using a lens with a focal length of 50 mm. The transmitted light was collected by a lens of the same focal length and then imaged on a CCD camera. The scheme

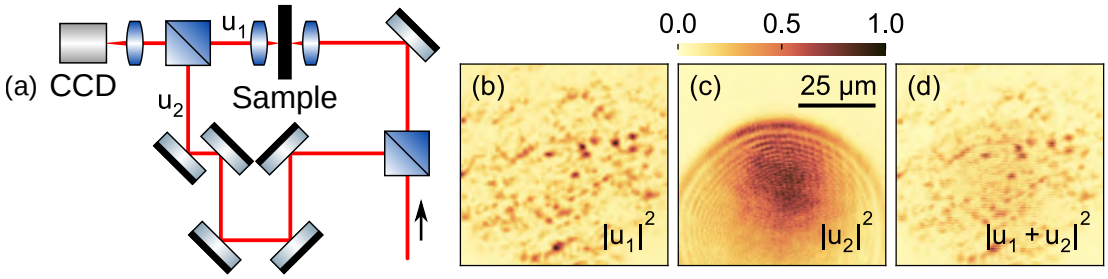

Figure 8.1: **Experimental setup for phase measurements** (a) Scheme of experimental setup for transmission measurements with Mach-Zehnder interferometer. $|u_1|$ and $|u_2|$ correspond to the signal transmitted through the sample and reference wave, respectively. (b) Real space map of the transmission intensity. (c) Real space of the reference beam laser intensity. (d) Interferogram image on a CCD camera. Scale bar on panel (c) shows spatial dimensions for panels (b-d). Color bar shows color scale for the normalized intensity for each map.

of the constructed transmission setup is illustrated in Figure 8.1(a). The diameter of the excitation beam was about 60 µm.

We resonantly created the polariton condensate and investigated the phase change due to the interactions. In this approach, the studied interactions take place without the contribution of the excitonic reservoir, the only source of the phase changes are polariton-polariton interactions. Transmission measurements with the laser slightly blue detuned from the dispersion minimum have been previously used for studies of the bistabilities [118, 119]. In our case, the laser was detuned two linewidths (about 2 meV) above the polariton mode.

The Figure 8.1(b-d) show the exemplary real-space maps of the transmission intensity, laser intensity for the additional beam, and the resulting interferogram, respectively. Typical transmission consists of many spots of different intensities influenced by the photonic potential. The reference beam was placed at the edge of the aperture to maximize the angle between the two interfering beams, increase the number of fringes in the obtained interferogram, and thus increase the spatial resolution of the phase measurement. The last panel shows the interferogram that contains information about the intensity and phase of the transmitted signal. The interferogram resembles the signal transmitted through the sample, but also consists of the fringes resulting from the interference with the reference beam.

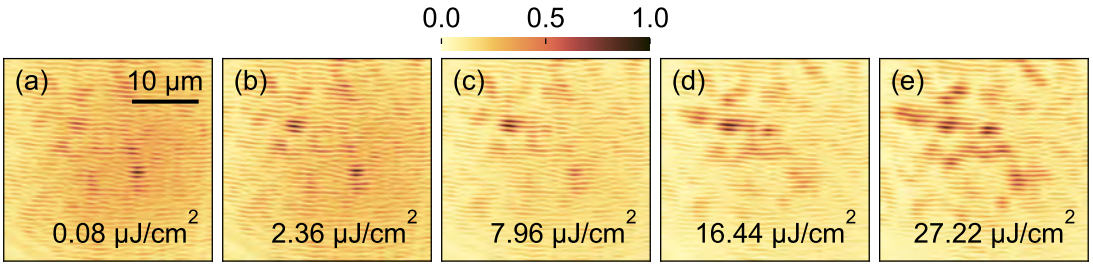

Figure 8.2: **Interferograms for different excitation power.** Real space interferograms for different pulse energy of the transmitted laser. Scale bar on panel (a) shows spatial dimensions for all panels. Color bar shows color scale for the normalized intensity for each map.

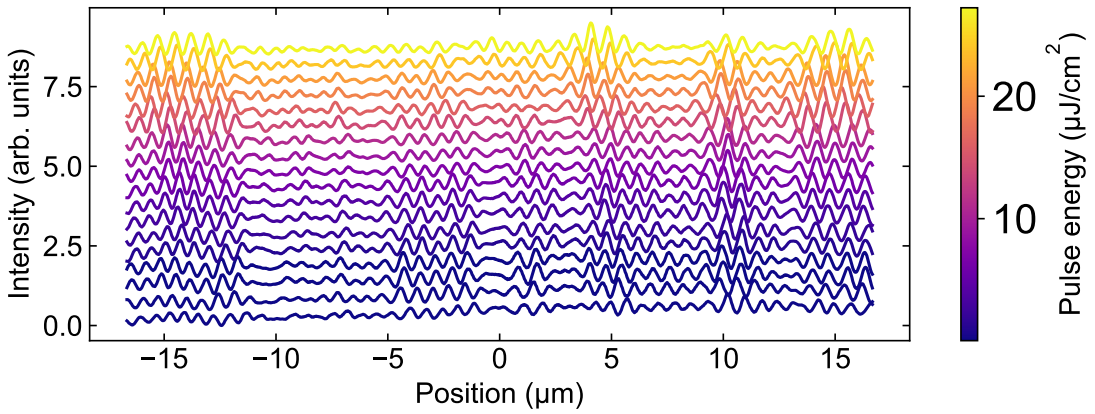

Figure 8.3: **Fringes position on the interferograms.** Waterfall representation of the fringes position for different excitation power. Cross sections in a horizontal direction at the center of the interferograms presented in Figure 8.2. Color bar shows color scale for pulse energy of the exciting laser.

We excited a large area of the sample and measured the interferograms for different excitation powers. The consecutive real space images are presented in Figure 8.2. Measurements were made for a delay of about 0.7 ps between the pulses originating from both arms of the interferometer. For an excitation power of $0.08\,\mu\mathrm{J/cm^2}$ we observed numerous places with dominant transmission. When the pulse energy of the laser was increased, the distribution of the places with large transmission changed. This is the first signature of the polariton-polariton interactions present in the system. With increasing excitation power, the interactions resulted in an increasing blueshift. We observed an increasing number of places with nonlinear increase of the intensity due to the matching of the energy modes with the laser.

The main purpose of the measurements was to track the polariton phase, which can be recovered on the basis of the position of the interference fringes. We present the vertical cross section calculated in the center of each measured interferogram in Figure 8.3. The results show many fringes of different intensity. These fringes change the position in between the cross sections corresponding to different excitation powers. In fact, it is very difficult to study the phase properties based on the cross sections of the interferograms. Within this procedure, one can focus only on a specific place on a sample and cannot distinguish the phase originating from the setup instabilities from the phase changes caused by the nonlinearities. For this reason, we extracted the phase using the procedure explained in chapter 7.

Figure 8.4 presents the amplitude and phase calculated based on the measured interferograms. In the normalized real-space maps of the amplitude (a-e), we observed many spots of different intensities. These places project the photonic potential and indicate spatial inhomogeneities in the efficiency of polariton injection into photonic potential minima.

Panels (f-j) show the real-space phase map calculated from the interferograms. The intriguing feature observed at first glance is that the mean phase changes significantly and randomly in the consecutive panels. This is due to the instabilities of the experimental setup. The main problem was caused by vibration of the optical table. In addition to that, we observed local phase fluctuations on the sample that

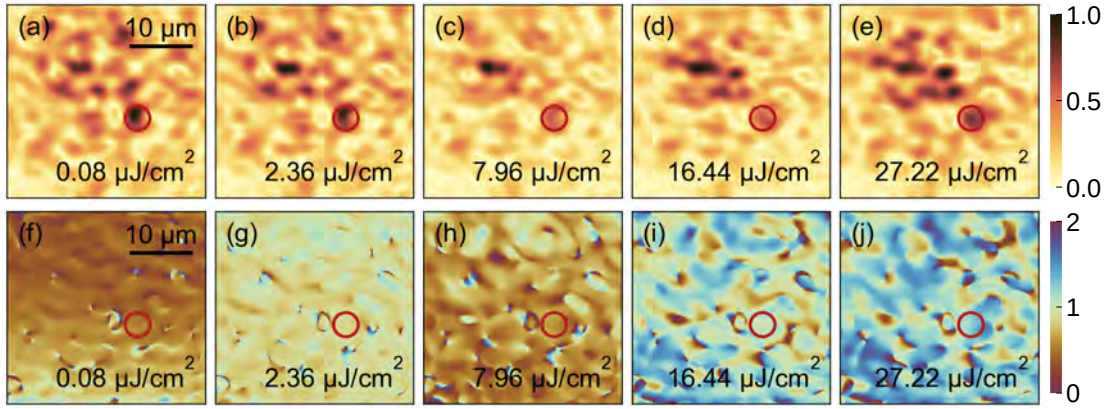

Figure 8.4: **Amplitude and phase of polaritons.** Real space maps of the (a-e) amplitude and (f-j) phase of the polaritons for different excitation power. Scale bar on panels (a,f) shows spatial dimensions for all panels. Color bars on the top (bottom) right show color scale for the normalized intensity (phase in π units) for each map.

seemed to be stable and repeatable.

In order to trace in detail the phase change for localized condensate, we chose a spot with a relatively large polariton population and marked it with the red circle. To trace the changes in phase (φ) in the marked spot, we compared it with the phase measured at four randomly chosen positions ($\varphi_1, \varphi_2, \varphi_3$, and φ_4) of small emission intensity. The idea behind it was to check whether the marked place exhibits phase changes correlated with the increasing excitation power of the laser. As we were unable to obtain an exact phase change, we wanted to check the relative phase change between the marked position and the four randomly chosen places on the sample. We chose places with low emission intensity to compare the phase φ with reference reminiscent of linear behavior.

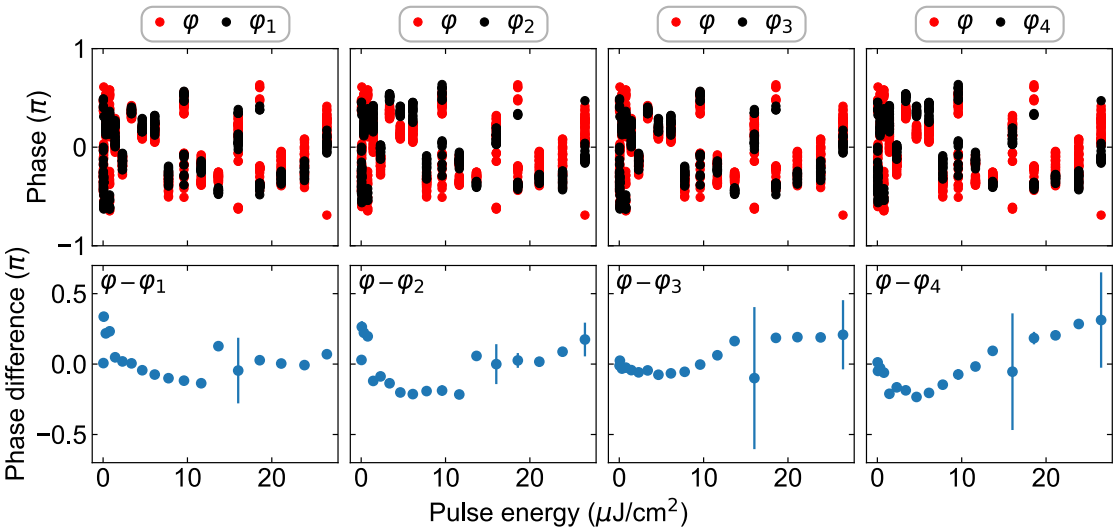

Figure 8.5: **Interaction induced phase build up of polaritons.** (Top panels) Phase φ (red dots) retrieved from the place marked with the red circle in Figure 8.4 and phases φ_1, φ_2, φ_3 and φ_4 (black dots) retrieved from random places on the sample. (Bottom panels) Phase difference between the marked place and four random positions for increasing pulse energy.

The phase in the marked region and four randomly chosen regions are illustrated as a function of pulse energy in Figure 8.5. Each excitation power was measured twenty times to take into account the fluctuations of the phase in time caused mainly by the setup instabilities. The red points on each top panel are the same and correspond to the phase φ. It is very difficult to find any correlations between the phase and the pulse energy. In addition, there is a large spread of the phase for many realizations at given pulse energy. The black dots in the following top panels present the phase extracted from four randomly chosen places. The black points on each panel seem to be random, but now they correlate with the red points. To demonstrate this, we subtracted each of the reference phases from the phase φ and plotted the difference for different pulse energies in the bottom panels. Here, the blue points indicate the mean phase difference and the error bars show the standard deviation for each pulse energy. We observed similar behavior in each scatter plot. In the low power regime, the phase difference decreased. Then, at higher pulse energies, it increased and stabilized. The same behavior on each panel proves that the measured interferograms contain information about the phase changes caused by interactions. The proposed method allowed for evidence the interaction-induced phase changes. The largest relative phase changes were observed for excitation power below $10\,\mu J/cm^2$ and were below 0.5π.

8.2 Summary

In this chapter, we considered the phase properties of resonantly excited polaritons in the transmission configuration. We presented a simple method to measure the polariton phase in a real space under unstable experimental conditions. We presented the relative phase change by comparing the place from which the emission changed nonlinearly with the excitation power with a few randomly selected places. We have shown that the relative phase changes are nonlinear and remain below 0.5π. The pulse energies needed to observe the phase changes are below $10\,\mu J/cm^2$.

The proposed system is very promising from the point of view of neuromorphic computing; however, there is still room for improvement. The nonlinear phase change can be acquired at lower pulse energies, but parameters such as exciton-photon detuning and depth of potential minima can still be optimized. Since the vibrations of the optical table are much slower than the single operation time, estimated at about 10 ps, the system instabilities are not a huge problem. To conclude, the presented experiment is simple to implement and allows one to easily achieve nonlinearities.

Chapter 9

Polariton condensate emission enhanced by optical feedback

Recent applications of nonlinearities in excitonic polaritons have allowed the creation of optical switches that approach fundamental quantum limits [120–123]. In such realizations, the system is pumped with the strong pump laser and the much weaker seed responsible for switching. This technique has also been used to improve the speed of operations or switching [124] compared to opto-electronic solutions [125]. In the devices discussed, the seed was pulsed; however, the pump laser was continuous.

In this chapter, we propose a similar idea to that discussed above, but working fully in a pulsed regime. Our aim is to create strong nonlinearities which can be applied to neuromorphic computing, giving an opportunity to improve the energy efficiency of the operation and giving hope for scalability to extend the polariton platform to large networks. For this purpose, we propose a new type of experiment in which the output signal from the condensate is reused to pump back the next condensate. This process should decrease the nonlinear threshold by injecting extra particles directly into the condensate. We realized this in an experimental configuration composed of a feedback loop.

9.1 Characterization of a feedback loop

The scheme of our idea is illustrated in Figure 9.1. We excited nonresonantly the sample MC-S with the pulsed picosecond laser. The emission from the sample was directed into the feedback line consisting of a mirror with tunable position. Our intention was to use a feedback arm to additionally excite the sample with the emitted light. The pulse of the emission passed the feedback setup and excited the sample resonantly at the moment of next nonresonant laser pulse approaching the sample. This is an ideal form of additional resonant excitation, taking into account the blueshift caused by interactions. The laser frequency was 76 MHz, which means that a single pulse travels approximately 3.95 m in the air before the next one is fired. For this reason, our feedback loop was about 2 m long, with the possibility of precisely adjusting the position of the last mirror with a delay line and using a piezo stage. The two pulses (nonresonant laser and resonant emission) excited the sample simultaneously, and the resulting signal was directed to the CCD camera (and time integrated). To avoid exciting the sample with the laser

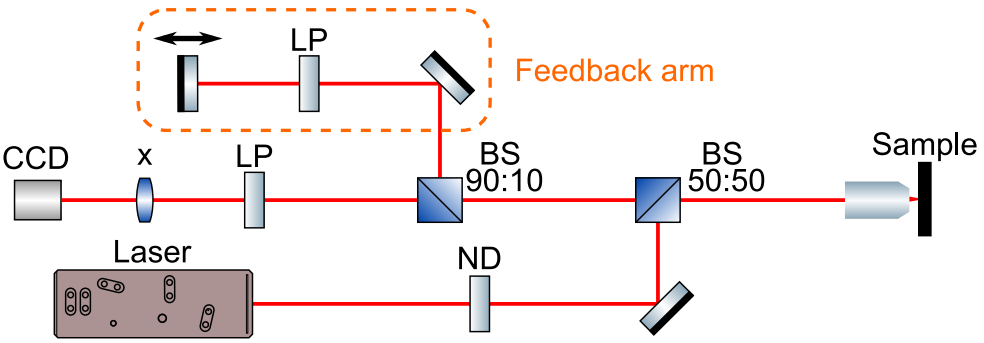

Figure 9.1: **Scheme of the experimental setup with feedback loop.** Pulsed laser excites nonresonantly the sample from the front side. Neutral density (ND) filter is used to control the power of the laser. The emission from the sample is directed to the feedback arm (marked with dashed orange rectangle) and then excites the sample. The length of the feedback arm is tuned using the last mirror. The signal is collected on a CCD camera that record the real-space images produced by a lens (x). Long pass filters (LP) on the detection side and feedback arm were used to remove the laser. Reflection to transmission ratios of beam splitters (BS) are marked.

reflected from the sample, we used a long pass filter on a feedback arm.

The initial measurements were performed without the long pass filters to characterize the laser. We excited the sample with a laser tuned to the first high-energy Bragg minimum of the sample reflectivity spectra and compared the signal observed on the CCD camera without and with the feedback arm. We excited the sample with the 1.32 pJ pulses and measured the laser on a CCD camera for different delays between the pulses, thus exciting the sample from the feedback loop and from the main line. For each delay, we repeated the experiment 100 times with an acquisition time of 100 ms. The results of the studies are illustrated in Figure 9.2. Panel (a) presents the signal intensity for different delays between pulses set by the position of the mirror on the feedback loop. The bright red points show the laser stability during the experiment. Each point corresponds to the mean intensity collected from the 100 frames with blocked feedback loop. These frames were collected just before measuring the signal with the full setup including the feedback loop. During the whole experiment, the laser intensity was stable and the signal on the camera was roughly on the same level. The signal observed for the laser with a feedback loop was qualitatively different. For delays larger than 10 ps we observed a stable signal of higher intensity than that observed without a feedback loop. For smaller delays, we observed interference between the pulses that led to significant changes in intensity over time. As a consequence, the mean intensity value varied around the value of about 1.8×10^7 counts. The changes were the highest around the zero delay. We calculate the feedback signal (I_F) that describes the quantitative contribution of the feedback loop to the total intensity observed on a camera:

$$I_F = \frac{\langle I_{EF}\rangle - \langle I_E\rangle}{\langle I_{EF}\rangle + \langle I_E\rangle} \tag{9.1}$$

where I_{EF} is the emission signal from the single measurement in the experimental setup with the feedback loop and I_E is the single measurement of the emission intensity for the setup configuration without the feedback loop. The feedback

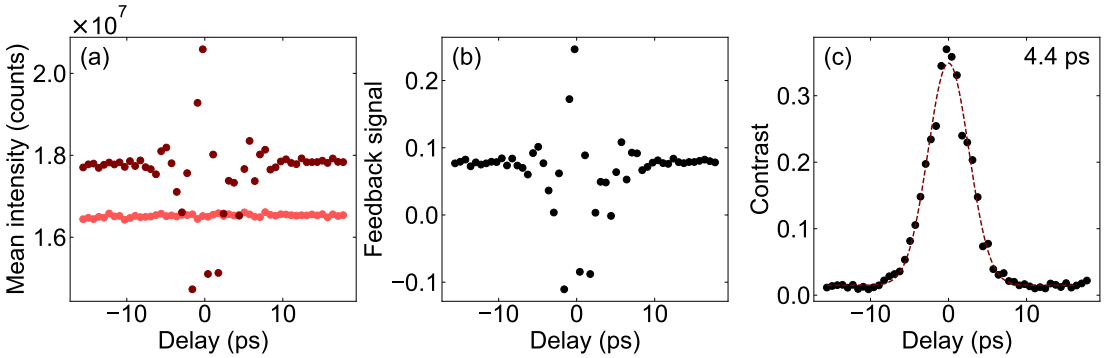

Figure 9.2: **Laser characterisation in a feedback experiment.** (a) Mean intensity of the signal measured 100 times for each delay set on a feedback arm. Results collected on a setup without long pass filters. Dark (bright) red dots correspond to the signal obtained with (without) feedback arm. (b) Feedback signal calculated for each delay based on mean intensities. (c) Contrast I_C calculated for each delay based on the 100 maps measured with and without the feedback arm. Red dashed curve illustrates the Gaussian fit of 4.4 ps FWHM.

signal presented in Figure 9.2(b) is constant at a level below 0.1 for large delays. This is the additional contribution resulting from the feedback arm excitation. For small delays, the feedback signal reflects the pattern observed in total intensity, which is a result of laser interference. Subsequent frames measured for each delay were used to characterize the interference. We calculate the contrast I_C based on the maximum I_{EF}^{max} and minimum I_{EF}^{min} intensity emission intensities measured for each delay according to the equation:

$$I_C = \frac{I_{EF}^{max} - I_{EF}^{min}}{I_{EF}^{max} + I_{EF}^{min}} \tag{9.2}$$

The contrast is illustrated in Figure 9.2(c). The contrast maximum was observed at zero delay. We fitted the Gaussian function to the data points and obtained the full width at half maximum of 4.4 ps. This means that the interferences were the highest at zero delay and decreased with increasing delay time as a result of a smaller time overlap between the pulses. The FWHM agrees with the laser pulse width, which is estimated at about 4 ps.

9.2 Nonlinearities enhanced by the feedback loop

Knowing the basic properties of the setup and the laser, we performed the measurements with the long pass filter on the feedback arm. We studied the intensity on the CCD camera for the emission from the sample and compared with the signal observed for the mix of nonresonant excitation with resonant excitation from the feedback loop. Figure 9.3(a) shows the intensity on the CCD camera for different pulse energies. The delay between pulses was set initially to 4 ps. In the single-beam only experiment (light blue dots), we observed a nonlinear increase of the intensity with increasing excitation power. The strong increase in the signal intensity corresponds to the condensation threshold at about 60 pJ. For the experiment with the feedback loop (dark blue dots), we observed a similar characteristic, but of higher intensity. The addition of the feedback arm resulted in a

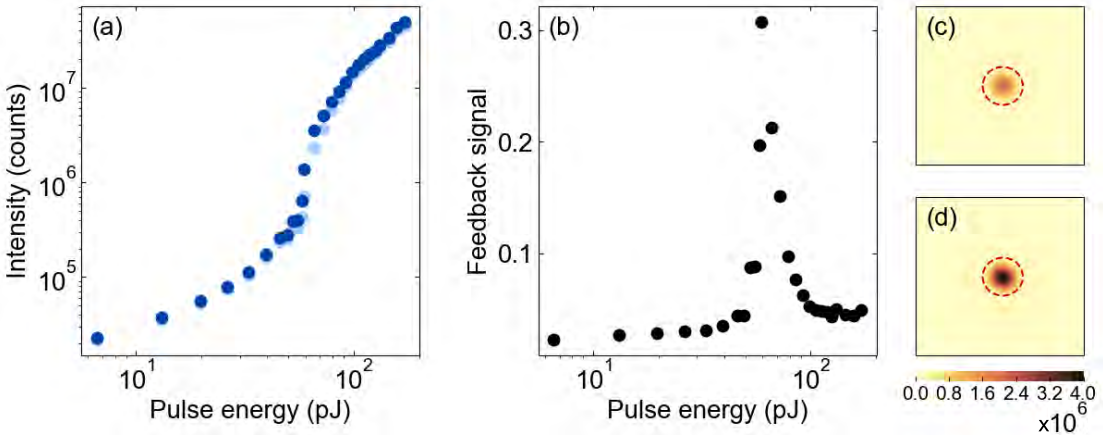

Figure 9.3: **Nonlinearities obtained in a feedback setup.** (a) Power dependence of the signal intensity observed on the CCD camera for a setup configuration with (dark blue) and without (bright blue) feedback arm for delay time between the pulses of 4 ps. (b) Calculated feedback signal for different pulse energy. Real space image of the signal observed at pulse energy of 59.21 pJ in a setup configuration (c) with (d) without a feedback arm. Red dashed circles indicate the areas from which the signal intensities were obtained. Colorbar placed in the bottom shows color scale for both (c) and (d) panels.

lowering of the condensation threshold. The calculated feedback signal presented in Figure 9.3(b) revealed that the feedback loop nonlinearly increases the total signal observed on a camera. For pulse energies below 60 pJ, the feedback signal was below 10%. The highest increase was observed at the threshold power and exceeded 30%. The last panels present the real space images measured for the excitation energy of 59.21 pJ for the configuration without (c) and with (d) feedback loop.

Figure 9.4 shows the feedback signal calculated from the measurements performed for different excitation powers as a function of the delay between pulses. For a small excitation power, the feedback signal was low and did not depend on the delay between pulses. For a pulse energy of 0.66 pJ the feedback signal was about 0.04. In this case, part of the emission excited the sample again and acted as a new source of light, adding additional energy to the system. For a higher excitation power (39.47 pJ), the emission from the sample was larger, so the feedback signal was also higher, because the pulse that passed the feedback line carried more energy. The considered conditions are similar to the situation where the system is excited with two pulses delayed in time and the intensity is integrated in time. Here, the feedback signal does not depend on the delay time, as a result of averaging the signal in time on a CCD camera.

Interestingly, for the excitation power just below the threshold (59.21 pJ), we observed a strong dependence of the feedback signal on the delay. For a long delay time, we again observed an additional constant intensity originating from the feedback arm, which we attribute to the emission from polaritons below the condensation threshold. However, around the zero delay, a sudden increase of the feedback signal occurred. Here, the laser pulse energy was slightly below the condensation threshold. In the small time delay, the pulse that passed the feedback line was enough to induce condensation, resulting in a large feedback signal. Under

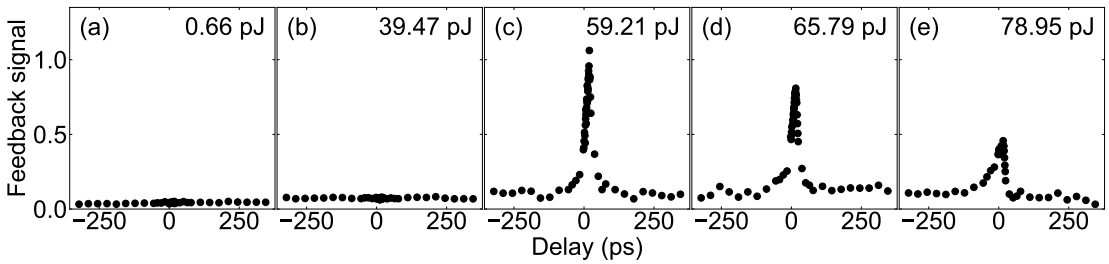

Figure 9.4: **Feedback signal for different pulse energies.** Feedback signal for different delay time between the nonresonant pulse and pulse from the feedback arm. The consecutive panels correspond to different pulse energy of the laser indicated in top right corner.

these conditions, the use of a feedback loop increased the intensity measured on a CCD camera more than twice. The condensation threshold was achievable only for small time delays between pulses.

For a higher excitation power (65.79 pJ and 78.95 pJ), the condensation threshold was exceeded for every delay between pulses. However, a nonlinear increase of the signal was observed for delays around zero. Here, the peaks of the feedback signal were smaller because instead of reaching the condensation threshold using the feedback loop pulse, an increase in nonlinear emission from the already obtained condensate was achieved.

Note that for pulse energies above the condensation threshold, the feedback signal was asymmetric, with higher intensity at negative delays. In these delays, the laser pulse created the condensate coexisting with the depleting excitonic reservoir, and then the second pulse after some time created a second condensate. For positive delays, this nonlinear behavior was not observed because of the inability to reach the condensation threshold within the weaker feedback arm pulse. Our results show that the highest nonlinearities are present at the condensation threshold. Interestingly, the maximum of the feedback signal was at delay of 18 ps between the pulses independently on the excitation power. This value is closely connected to the blueshift of the modes which was changing with the time.

From the decrease of the amplitude of the feedback signal, one can obtain the decay time τ of observed nonlinearities. Depending on the pulse energy of the exciting laser, this characteristic time should change as the depletion of the

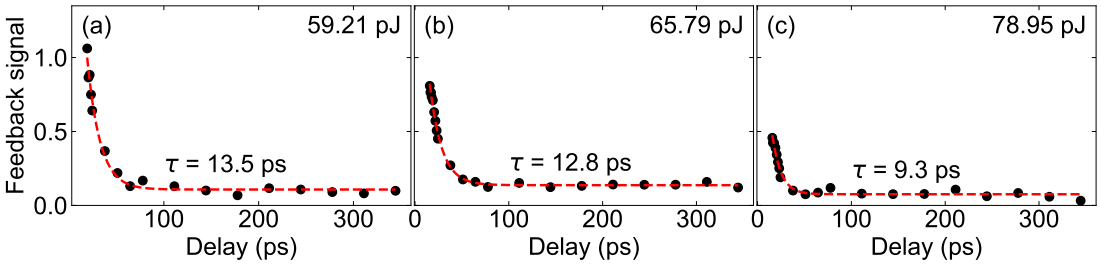

Figure 9.5: **Decay of the feedback signal.** Decay of the amplitude of the feedback signal for different pulse energies of the excitation laser indicated in top right corner. Red dashed curves correspond to the exponential decay fit to the data. The decay time τ obtained from the fitting is illustrated on the bottom.

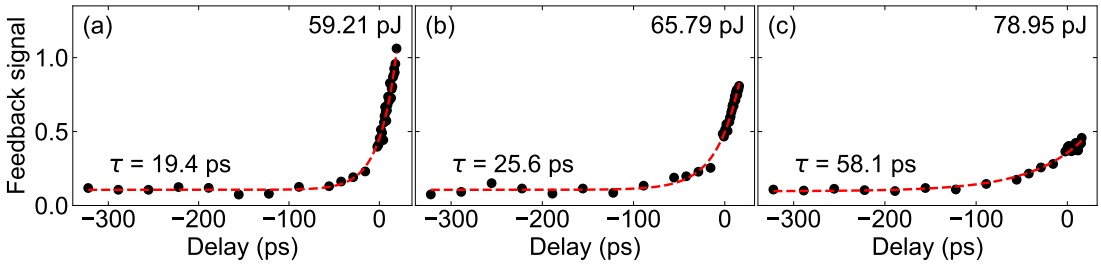

Figure 9.6: **Build-up of the feedback signal.** Build-up of the feedback signal for different pulse energies of the excitation laser indicated in top right corner. Red dashed curves correspond to the exponential growth fit to the data. The characteristic time τ obtained from the fitting is illustrated on the bottom.

reservoir changes. We received the decay time of the nonlinearities from the fitting of the exponential decay of the feedback signal as presented in Figure 9.5. The decay times were comparable to the typical lifetime of the condensate on our samples [126] and were shortened with increasing excitation power. In this case, the main signal propagating through the feedback arm originated from the condensate emission. This means that the decay time of the feedback signal followed the lifetime of the condensate. We observed a shortening of the condensate lifetime with an increase of the excitation power as a result of increased depletion of the reservoir.

The build-up of the feedback signal is expected to be much longer than the decay as the pulse from the feedback arm approaches the sample before the non-resonant pulse. Studies of the feedback signal in the negative delays allow one to probe the excitonic reservoir. We perform a fit of the exponential growth in the feedback signal as presented in Figure 9.6 and obtained the time constants τ for each excitation power. Interestingly, growth slows with increasing excitation power. At the pulse energy close to the condensation threshold, the characteristic time was of 19.4 ps. The largest τ (of 58.1 ps) was observed for the highest measured pulse energy. In this case, the first pulse was a weaker pulse originating from the feedback arm. The second, more intense pulse created the polariton condensate. The nonlinear increase of the intensity or the feedback signal appeared when the excitonic reservoir was still present wihle second pulse excitation. The intensity of the feedback signal increased with the number of excitons in the reservoir at the moment of second pulse excitation. At higher pulse energies, one can probe the larger timescales of the reservoir. Within this method, we could probe a bottom bound of the lifetime of the excitonic reservoir.

9.3 Summary

This chapter introduced a unique idea to create a nonlinear polariton system using an additional feedback loop on a detection side. The presented experimental setup realized an additional seed that resonantly excited the sample. We discussed the consequences of this experimental idea.

In Sec. 9.1 we presented the idea of the experiment and performed the characterization of the system. We defined the feedback signal and characterized the exciting laser.

In Sec. 9.2 we discussed the nonlinearities triggered by the feedback loop. We observed a reduction of the nonlinear threshold by reusing the emission from the sample. We observed that the increase of the nonlinearities strongly depends on the time delay between the laser pulse and the emission pulse from the feedback loop. We achieved more than doubling of the emission intensity using a seed. The increase was greatest at the condensation threshold.

The presented system possesses unexpectedly high nonlinearities which can be used in ultrafast operation. Our results can be used for acquiring nonlinearities observed in ultra-low power regimes. Perhaps the main advantage of our idea is scalability. The presented system allows for connections between the condensates in time and paves the way for building complex neural networks based on many nodes. These results are encouraging for studying delayed-in-time nonlinear phenomena.

Chapter 10

Binarized artificial neural networks

Photonic neuromorphic computing is developing very intensively in recent years, significantly improving the speed and energy efficiency of operations [39, 127–135]. The greatest advantage of photonics over electronics lies in the significantly lower energy losses during data transmission. However, the main problem with a photonic system is the weak interaction which is needed to create nonlinear operations. Exciton polaritons as half-light half-matter particles provide strong interactions [136, 137], potentially decreasing the power consumption in a working device. In addition, they can perform operations on very short timescales [92, 138, 139]. In the most common experimental realizations of neural networks, the input data is encoded by simultaneously arriving light pulses, or continuous beams formed by spatial light modulators [140–142].

In this chapter, we present an experimental realization of a binarized neural network, where the hidden layer in the network is composed of the nonlinear logic gates, in this case XOR logic gates. We chose the XOR-based binary network, as it is relatively simple to implement and comparable to other architectures [35].

The realization of XOR logic gates by real physical systems was demonstrated in photonic crystals [143, 144], optical fibers [145] and plasmonic structures [146].

We present the opto-electronic realization in semiconductor microcavity with the hardware part consisting only of passive optical elements. We demonstrate further on, that our binarized network can be applied to solve handwritten digits recognition problem. In addition, we show a fully optical implementation of the XOR logic gate with outstanding energy efficiency.

The holy grail would be to create an all-optical polariton-based neural network, as it could potentially operate on very fast timescales and have very high energy efficiency [112, 147].

10.1 Two-dimensional nonlinearities

To create a nonlinear XOR logic gate, a system with two-dimensional nonlinearities is needed. Two-dimensional nonlinearities can be explained on system with two spatially separated localized condensation sites excited independently by two pulsed laser beams. The emission from the single node can be considered as an output associated with the two-dimensional input space spanned by the energy of

the first and second pulses.

For a large spatial separation between the condensates, the nodes do not interact with each other. The first node responds to the first excitation pulse and the second node responds to the second excitation pulse. In the case where the first pulse affects only the first node, the emission intensity map has linear fronts of equi-intensity surfaces as in Figure. 10.1(a). This behavior is expected even if the first spot responds with the nonlinear emission to the first input pulse. Similarly, linear fronts are expected to be observed when the pulse affects only the second node, as presented in Figure. 10.1(b). For a sufficiently small distance between the nodes, each laser beam will affect the two condensation sites, or interactions between the condensates will appear. In this case, the system can still exhibit linear interactions manifested by linear fronts on the emission intensity map. The slope of these fronts depends on the influence of the laser beams on the condensate emission and impact of the interactions between the condensates. In the presence of nonlinear interactions between the condensates, the emission begins to behave nonlinearly, and the fronts start to bend [Figure. 10.1(c)]. The bending of the equi-intensity surfaces is a clear signature of nonlinearities. Finally, determining the output as a function of two arbitrarily chosen input parameters allows one to find a system with nonlinearities that could perform the logic operations of nonlinear logic gates. Note that we do not even discuss the origin or properties of the nonlinearities; this method does not require any knowledge about the nonlinear response.

In the experimental approach, the linear behavior system is easily achieved, for

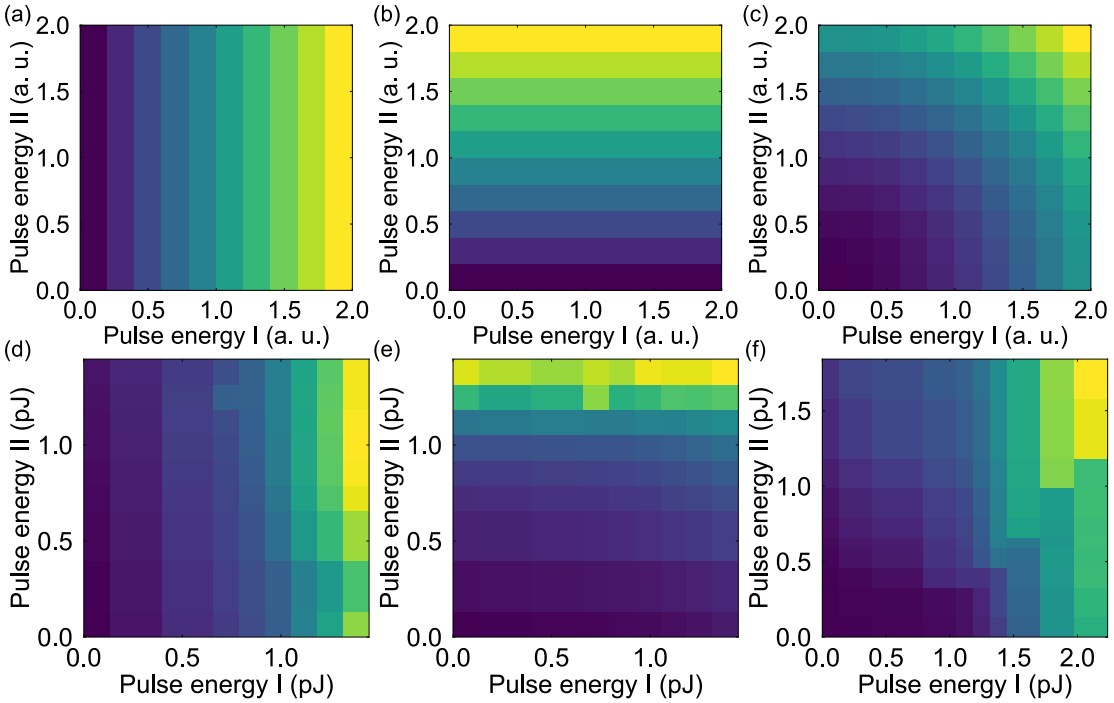

Figure 10.1: **Two-dimensional nonlinearities.** (a-c) Simulated and (d-f) measured maps of emission intensity of a condensate excited with two excitation beams separated in space. Emission of condensate insensitive to the increasing excitation power of first (left), and second (center) beam. Right panels show condensate revealing nonlinearities in emission visible as bends of the equi-intensity surfaces on the map.

example, by creating the two condensates within the two significantly separated in space beam pulses. The emission studied for each condensate in this configuration is presented in Figure. 10.1(d,e). We observed that the emission of the first condensate (panel (d)) increased with the energy of the first pulse. The change of the second pulse excitation power did not change the emission. Similarly, the emission from the second condensation site (panel (e)) was influenced by the second pulse but not by the first pulse. On both emission intensity maps, we observed linear fronts, confirming the linear behavior. Nonlinear behavior was generally observed for the shorter distance between the excitation beams (of about 2-5 µm), where flows of polaritons and interactions between the condensation sites were possible. In Figure. 10.1(f) we present the emission from the first node that resembles the curved surfaces of equal intensity in a two-dimensional input space. In this case, the distance between the condensates was approximately 3 µm.

10.2 Opto-electronic machine learning

Our goal was to create a binarized neural network that performs simple classification tasks. For this reason, we started by constructing an XOR logic gate that can be a building block of such a network [35]. The creation of a single logic XOR gate requires two-dimensional nonlinearities as it is not a separable classification problem. Since we know that in a linear system we can only achieve a nonlinear gate with 75% efficiency or less, we used exciton polaritons to create two-dimensional nonlinearities. The scheme of the experimental idea that presents the realization of the logic gate XOR is illustrated in Figure. 10.2. Here, the input binary data were encoded by two independent laser pulses separated in space. The low (0) and high (1) logic states were encoded using two pulse energies of each laser beam (low and high, respectively). The two laser beams created two condensates at separate condensation sites. Within this method, the strength of nonlinear interactions can be easily tuned, for example, by changing the distance between the condensates or choosing the localization potential depth that affects the efficiency of polariton tunneling between the condensates. The nonlinear emission of each condensate served as an output signal, which was further linearly classified.

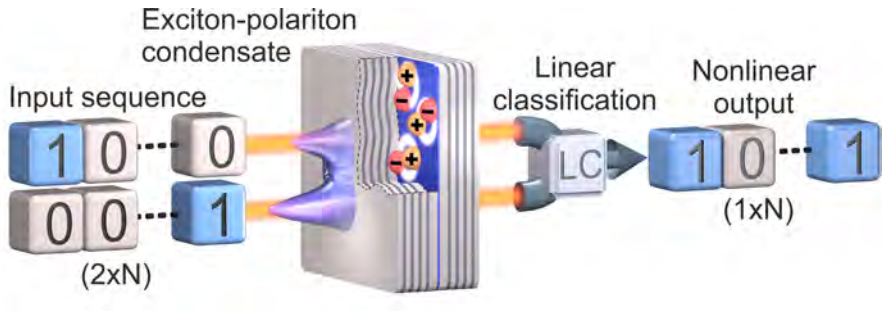

Figure 10.2: **Scheme of opto-electronic XOR realization.** Schematic illustration of opto-electronic realization of XOR logic gate using exciton polariton condensate as a source of nonlinearities. Two beams of ps pulses encoding the inputs create two polariton condensates producing a nonlinear response. The linear classification is performed on the nonlinearly transformed signal to obtain the output of logic gate. Illustration produced by Dr. Mateusz Król.

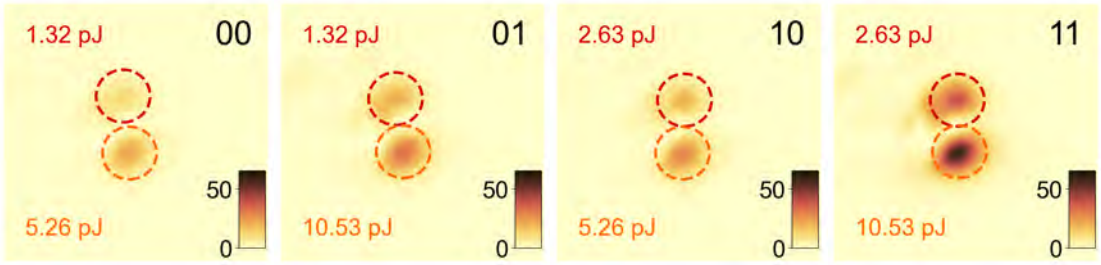

Figure 10.3: **Emission from two condensation sites.** Real-space emission of two spatially-separated polariton condensates excited with (a) low/low, (b) low/high, (c) high/low and (d) high/high excitation powers encoding '00', '01', '10' and '11' input states, respectively. Color code corresponds to the emission intensity marked by the color bar on each panel. Left annotations in the panels describe the pulse energy applied to the first (marked with red circle) and second (marked with orange circle) condensate site.

Linear classification was performed on a computer using the data obtained in the experiment.

The presented scheme of the experiment was realized with 4 ps long pulses of 76 MHz laser tuned to the first minimum of the cavity stop-band on the high-energy side of Bragg mirrors. The pulses were separated in space by 2 µm and delayed by 14 ps to create two condensates without the effects of laser interference. We realized four configurations with different excitation powers of two pulses that encoded all four input logic states. The emission from the excited condensation sites was collected by a CCD camera. The real space emission from two spatially separated polariton condensates for different excitation powers of the two excitation lasers is presented in Figure. 10.3. For each realized logic state, we detected emission from the condensation sites marked with dashed circles. The orange spot was excited with larger pulse energy, and the photoluminescence observed from this site was more intense. However, both sites were close enough to observe each laser beam affecting both condensates. The presented maps reveal the nonlinear character of the investigated system. The emissions from both condensation sites were significantly higher for the '11' input configuration than for the others.

To check whether the nonlinearities present in the studied system are large

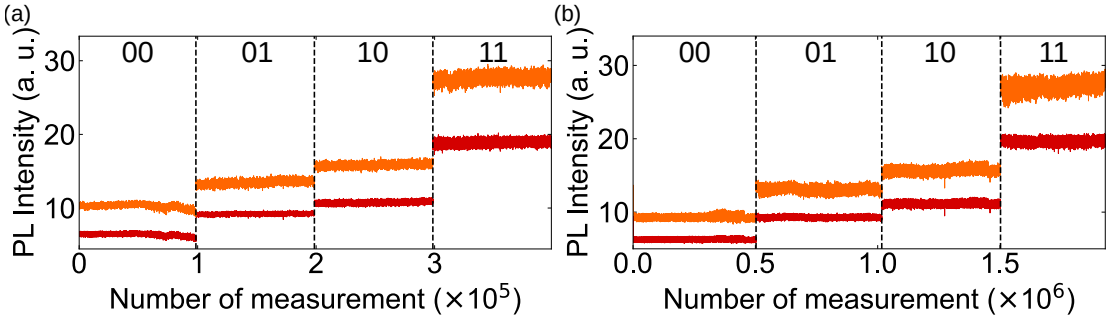

Figure 10.4: **Intensity of emission from two condensation sites.** Intensity of emission from first (orange) and second (red) condensation site marked respectively by red and orange circles in Figure. 10.3. (a) Learning and (b) testing set of data with four logic realizations marked on the top.

enough to create an XOR logic gate, we produced more than 550,000 realizations of each logic state. These realizations were used to prepare two datasets and perform linear classification to verify the accuracy of the XOR gate operation. We used almost 2 million real space photoluminescence maps for teaching and 400,000 maps for the testing phase. Both data sets were measured separately in time to avoid learning the algorithm of time-dependent features. The mean intensities of emission from the first and second condensation sites (regions marked with red and orange dashed circles, respectively) are presented in Figure. 10.4. We observed a nonlinear response with strong emission intensity in the realization of the logic state '11' and significantly smaller signal for all other states '00', '01' and '10'). The signal was noisy, mainly because of the laser instability pronounced by the nonlinear response of the condensate.

To describe the nonlinearities present in our realization, we define the degree of nonlinearity η:

$$\eta = \frac{\langle I_{00}\rangle + \langle I_{11}\rangle - \langle I_{01}\rangle - \langle I_{10}\rangle}{V_{00} + V_{01} + V_{10} + V_{11}} \tag{10.1}$$

where $\langle I_{ij}\rangle$ is the average intensity within the logic state 'ij' and V_{ij}=$\langle I_{ij} - \langle I_{ij}\rangle^2\rangle$. η calculated for the first and second condensation sites according to the learning set were approximately 14 and 9, respectively. The same procedure was implemented on the testing set where $\eta \simeq 11$ and $\eta \simeq 13$. The differences between the values in the teaching and testing sets were mainly due to noise, which was effectively having a greater impact on the teaching data set collected over a longer time. Despite the noise present in the system, it is clear that the proposed system was nonlinear. It should be reminded that at this point we demonstrated two-dimensional nonlinearities on a basis written as a linear combination of the excitation power of the first and second laser beams.

The accuracy rate of the constructed XOR gate operation is presented in Figure. 10.5(a). We performed a linear classification on the learning data set and then verified the accuracy rate of the XOR operation on the testing set. This procedure was performed on a computer. For this particular system, we obtained 100% accuracy (orange point). The same procedure was used to create logic gates based on different arrangements of condensation sites with different Josephson tunneling, potential distribution (as discussed in chapter 5), laser stability, and hence degree of nonlinearity.

The same procedure was used to create logic gates based on different arrangements of condensation sites with different degree of nonlinearity. We observed that the accuracy rate (or the ratio of correct predictions) of the XOR gate increases with an increasing degree of nonlinearity. The perfect accuracy was reached for data sets that had η larger than 5. We noticed that for sufficiently small nonlinearities (or substantially large noise) the accuracy of the constructed gate can be smaller than 75% which is even worse than the best results expected for raw linear classification.

The constructed opto-electronic XOR gates were used to create a single hidden layer in a binary neural network. We performed handwritten digit recognition from the MNIST dataset, which consists of 60,000 training samples and 10,000 testing samples [148]. The network scheme is presented in Figure. 10.5(c). We converted each 28×28 grayscale image into a binary bitmap and assigned a random pair of

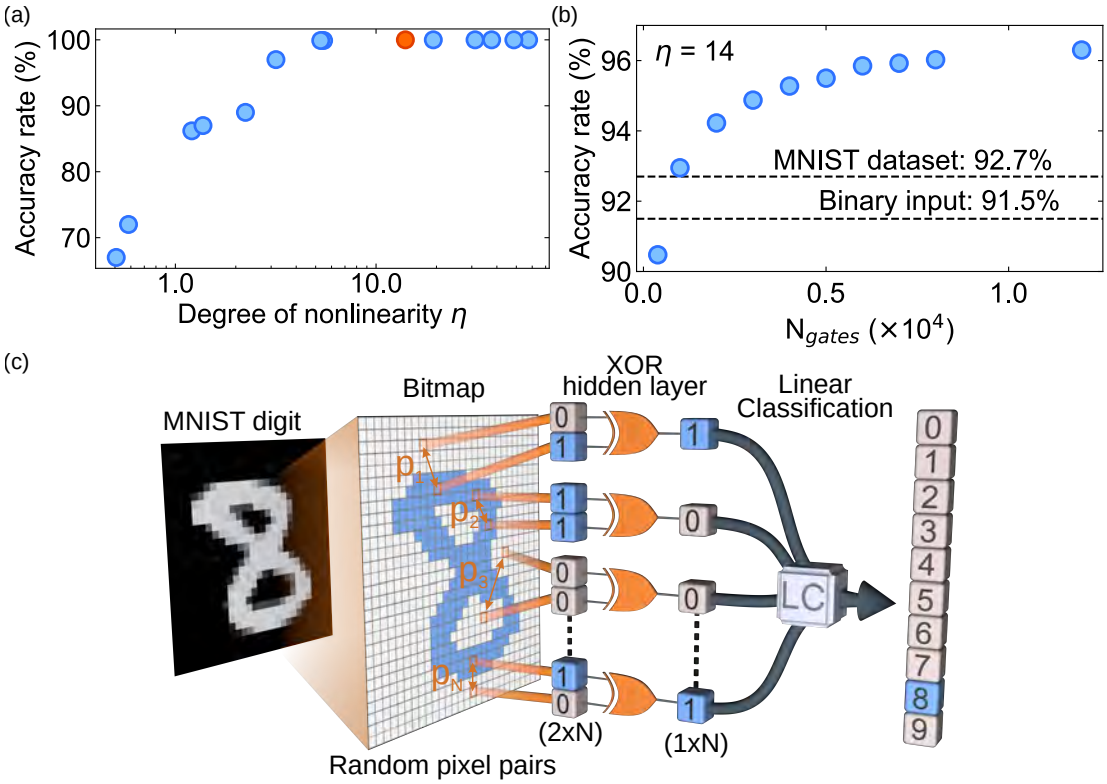

Figure 10.5: **Opto-electronic machine learning.** (a) Accuracy rate of the XOR gate as a function of the degree of nonlinearity η. Orange point corresponds to the realization presented in Figure 10.3 and Figure 10.4 (b) Accuracy of the MNIST handwritten digit prediction for different number of XOR gates in a hidden layer. Dashed lines show the accuracy rates of software linear classification for the full and binarized MNIST input. (c) Schematic illustration of the network with a single hidden layer of XOR gates. Illustration of the network produced by Dr. Mateusz Król.

pixels to the inputs of each XOR gate. To resolve the correlations between pixels, we assigned the same pairs of pixels $p_1 \ldots p_n$ to the same gates $1 \ldots n$ for all digits. We used time multiplexing to create a hidden layer of all the gates constructed and performed logistic regression. We used a supervised learning method based on softmax regression that handles problems containing multiple classes. In the MNIST classification problem, softmax regression returned the probabilities for each class of digits (0–9). To perform classification, we used a linear mapping method: $f(\mathbf{x}_i, \mathbf{W}, \mathbf{b}) = \mathbf{x}_i\mathbf{W} + \mathbf{b}$, where $\mathbf{x}_i$ is a vector of input states, $\mathbf{W}$ is the weights matrix, and $\mathbf{b}$ is a bias vector. Weights were randomly distributed prior to the training process. Minimizing the loss function given by the cross-entropy resulted in the obtaining of the weights. The minimization of the loss function was implemented using the Adam optimizer. The software algorithms were implemented on the Tensorflow [149] platform on a computer with a GeForce RTX 2070 GPU. The above approach was performed for networks with different numbers of XOR gates in a hidden layer. The accuracy rate of inference in the MNIST classification for a different number of XOR logic gates N_{gates} in a hidden layer is shown in Figure. 10.5(b). The accuracy rate increases with the number of XOR gates used and reaches a plateau above 96%. To reach this value, we used about 10,000 gates in the network. The accuracy obtained is comparable to or higher than modern

neuromorphic implementations [129, 141, 150–152], and significantly higher than the accuracy of the linear classification of pure software of the grayscale MNIST dataset (92.7%) or its binarized version (91.5%), obtained with the logistic regression algorithm. This procedure was implemented on a computer by Dr. Andrzej Opala, from Institute of Physics in the Polish Academy of Sciences.

10.3 All optical XOR gate

In the neural network presented previously, linear classification was performed on a computer, similarly to most photonic realizations [150, 153–155]. Speed and energy efficiency are limited in this approach, and the solution of this issue is to perform an all-optical device. We will show that it is possible to create exciton polariton based all-optical XOR logic gates, which brings us closer to the construction of an ultra-fast and efficient neural network. It can be thought of as the photonic realization of neural network accelerator previously reported in [156–159].

The XOR logic gate can be performed all optically through the mixing of the input and output signals. The realization scheme is presented in Figure. 10.6. In this approach, we used two pulsed laser beams that excite one condensation site. Similarly to the previous realization, the encoding of the logic state was performed by changing the excitation power of the nonresonant excitation with the 14 ps delay between the pulses. Each of the laser beam was additionally split using beam splitter before reaching the sample. One split part was pumping the condensate, and another part was weighted by a neutral density (ND) filter (w_1 or w_2, respectively) and then mixed with the nonlinear emission from the sample. The output of the constructed gate was the total intensity of the weighted auxiliary beam paths and the condensate emission.

The detailed experimental setup adopted for the realization of the all-optical XOR logic gate is presented in Figure 10.7. We used a mode locked Ti:Sapphire laser MIRA 900 from Coherent. The laser beam was split into two beams marked in red and orange. One of the beams passed through the delay line to control the delay time between the pulses originating from different beams. These two beams were split into two more beams each. In this way, we obtained two beams that

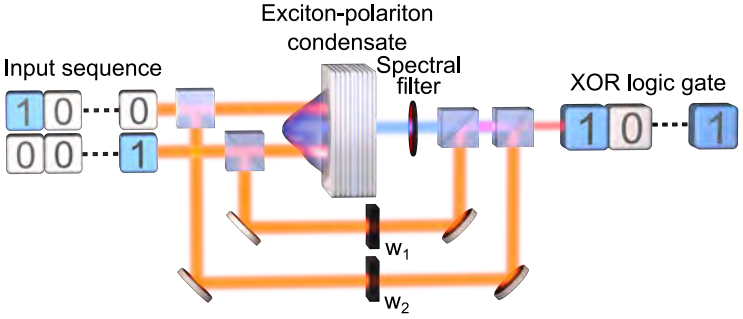

Figure 10.6: **Experimental setup for performing nonlinear classification.** Scheme of the experimental setup, in which the linear classification with a two-dimensional plane is implemented. Weights w_1 and w_2 were realized using neutral density filters. Illustration produced by Dr. Król.

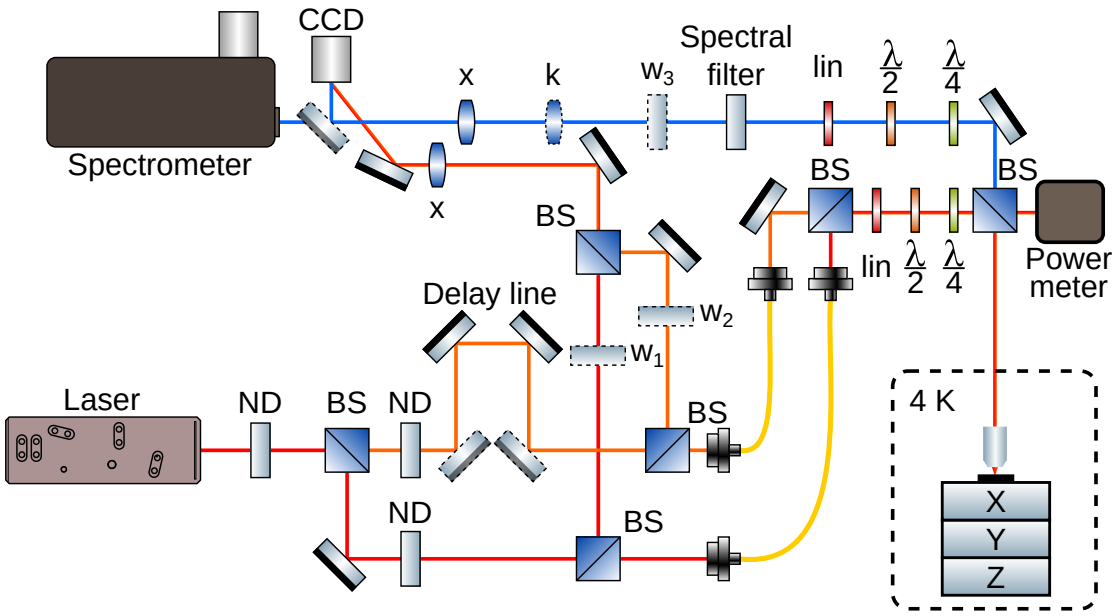

Figure 10.7: **Experimental setup for the realization of all-optical XOR gate.** Two input laser beams and emission from the sample are marked using red, orange and blue color, respectively. Continuously variable neutral density filters used for weighting.

excited the sample and two beams directed directly at the CCD camera. The laser beams focused on a camera were modified in intensity by neutral density filters w_1 and w_2 and then overlapped in space using a beam splitter. The delay time between the beam pulses was held above 4 ps to avoid interference effects. The other two beams passed through polarization maintaining optical fibers. Polarization optics was used to excite the sample with σ^+ polarized light. The power meter was placed behind the 50:50 beam splitter to control the pulse energies of the laser beams. The sample MC-S was kept in a cryostat at liquid helium temperature. The three piezo stages allowed for movement of the sample in three orthogonal directions. The excitation beams were focused on the sample using an objective of high numerical aperture of NA = 0.68. The emission was collected within the same objective. Polarization optics was set to pass only the σ^+ component. The spectral filter on the detection side was assuring the negative response. The experimental setup allowed for measurements of the emission in real and reciprocal space depending on the lenses used. We used a spectrometer for basic characterizations and a CCD camera for realization of a logic gate. All four beams were focused on the same spot on a CCD camera. In the presented configuration, we were able to control and measure both inputs and outputs. The all-optical linear classification of the output data was realized through the mixing of the weighted input signals with the output signal.

The essence of the whole approach was to merge two inputs with the output to obtain distinct states that mimic the XOR operation. Our idea can be written in the form of linear equations:

$$\begin{cases} w_1 \cdot I_{1h} + w_2 \cdot I_{2h} + w_3 \cdot o_{11} = A \\ w_1 \cdot I_{1h} + w_2 \cdot I_{2l} + w_3 \cdot o_{10} = B \\ w_1 \cdot I_{1l} + w_2 \cdot I_{2h} + w_3 \cdot o_{01} = B \\ w_1 \cdot I_{1l} + w_2 \cdot I_{2l} + w_3 \cdot o_{00} = A \end{cases} \tag{10.2}$$

where I_{xy} is the intensity of the x-th input with low ($y = l$) or high ($y = h$) excitation power and o_{ij} is the output intensity of the state 'ij'. In this scheme, both inputs and output were modulated with well-defined weights w_i and then focused on the same position on the CCD camera, giving a total intensity A or B. The coefficients w_1, w_2 were realized by neutral density filters. The laser intensity was much larger than the output intensity, so we did not use a neutral density filter for the emission, and the w_3 coefficient was set to 1.

Note that ND filters ensured weight values only between 0 and 1. There was no passive optical element that could extend this range. This led to a problem of solving a set of linear equations given in equation 10.2. Solutions with weights in the range mentioned above exist only for systems with a negative differential response. The studied condensate manifested a large blue shift. We put a notch filter on the detection side of the setup to cut the blue-shifted condensate, which resulted in negative response in the high laser power region. The influence of the notch filter on the emission is illustrated in Figure 10.8. The emission map in reciprocal space revealed the dispersion of the lower polariton with many localized states. We excited the condensation site with two beams of 1.18 pJ pulses delayed in time by 14 ps. We compared the emission for the setup without (panel (a)) and with (panel (b)) notch filter on the detection side and observed that the notch filter not only cuts the signal from higher energetic states, but also decreases the

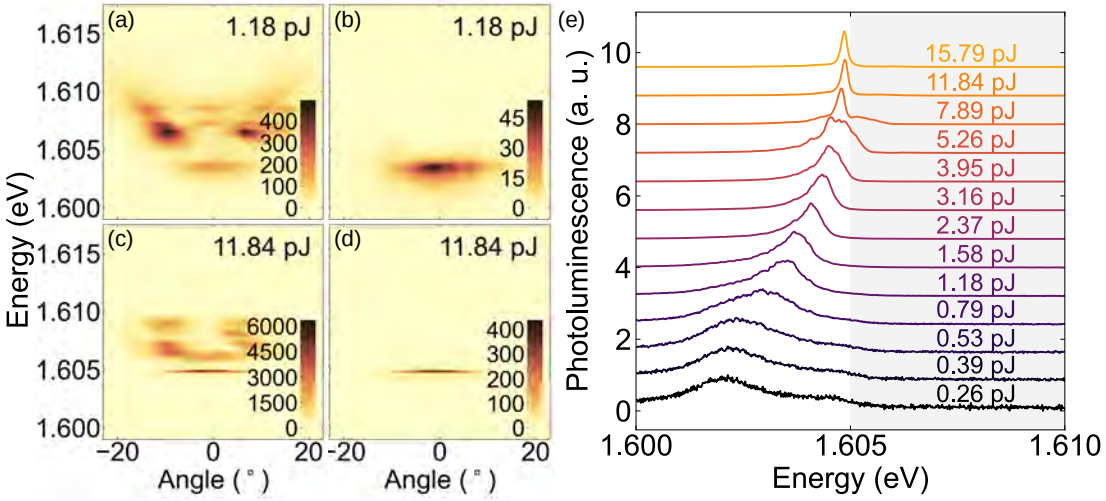

Figure 10.8: **Characterization of a spectral filter.** Real-space maps of emission for excitation (a,b) below and (c,d) above condensation threshold. Left (right) panels correspond to the spectra measured without (with) the spectral filter on the detection. The pulse energy of exciting beams is marked in the top right corner. Color scales give information about the emission intensity. (e) Waterfall plot of the filtered emission at incident angle for different excitation power. The region filtered by spectral filter is marked with the gray background.

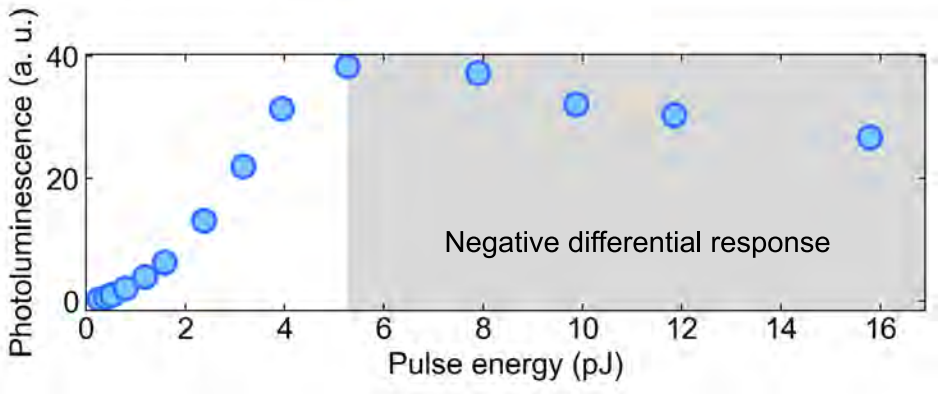

Figure 10.9: **Negative differential response.** Emission intensity for different pulse energy of beams exciting the condensation site. The region of negative differential response realized by the spectral filter is marked with the gray background.

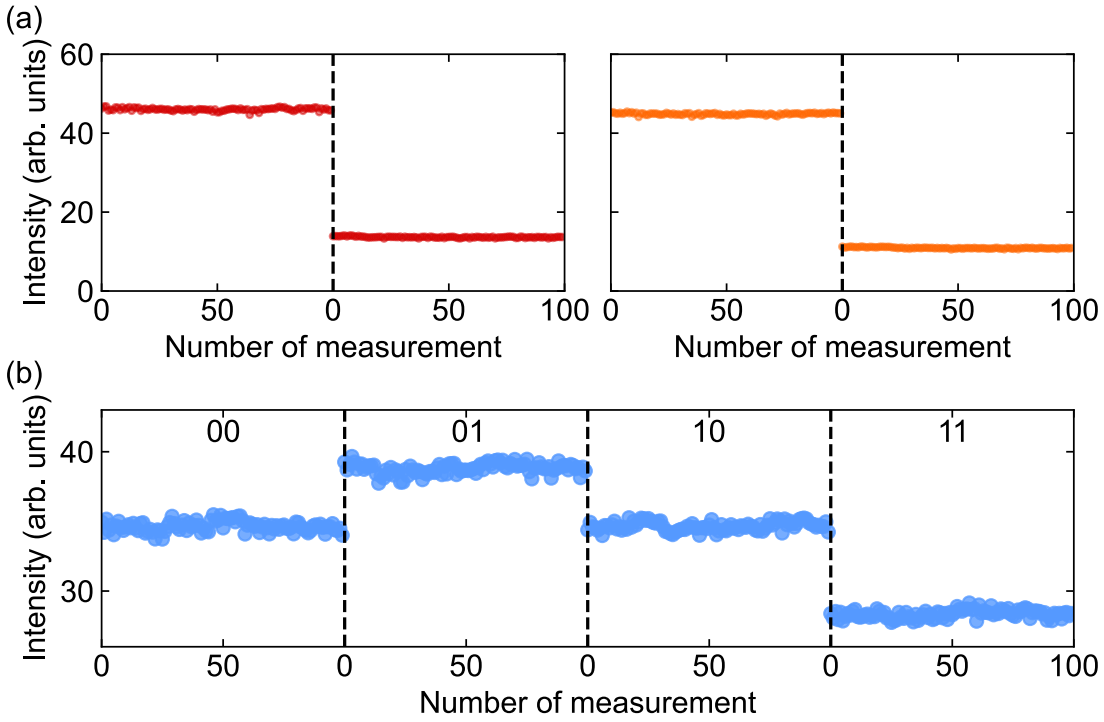

Figure 10.10: **Input and emission characterization.** (a) Intensity of the signal on the CCD camera for a beams of pulses encoding first (red) and second (orange) bit of an input state. Both high and low states were measured one hundred times. (b) Filtered intensity of the emission from the sample for four configurations of pulse energies of the exciting beams corresponding to four input states. Input states are marked on top.

emission from the ground state. This was due to the non-ideal steepness of the filter stop band. Similarly, above the condensation threshold, on a setup without the notch filter, we observed numerous states of different occupation. The ground state was of the highest intensity. The use of a notch filter resulted in a decrease of the observed condensate intensity and an almost complete suppression of the emission from the higher states. We extracted the cross sections at zero emission angle and presented the pulse energy for each of the exciting beams in panel (e). With increasing excitation power, the emission maximum was shifting towards higher energies. The gray area marked on a waterfall plot shows the region cut by the notch filter. We observed that the blueshift reaches the cutoff energy and does not increase further. At the highest pulse energies, the emission line dramatically narrowed because of the filtered higher energy region.

We recovered the emission intensity from the excited condensation site for different excitation power in a setup with a spectral filter on the detection side (Figure 10.9). For pulse energies below 5 pJ the photoluminescence increased nonlinearly with increasing excitation power. In this region, the condensate was energetically below the cutoff of the spectral filter. At higher excitation power, the condensate was significantly suppressed by the notch filter, and we observed a decrease in the photoluminescence intensity. In this region, the negative differential response was achieved. To make use of negative response and nonlinearities in a XOR gate construction, the pulse energies of 2.0 pJ and 7.9 pJ were chosen for encoding the low and high input states in an all-optical XOR.

The experimental realization of an all-optical XOR gate was divided into three stages. In the first stage, the inputs were characterized to obtain the coefficients I_{xy}. We focused the first and second beam on a CCD camera for high and low logic states and obtained the intensities together with the present noise [Figure. 10.10(a)]. Then both lasers were focused on the sample to obtain an output characterized in the same way for four realizations o_{ij} [Figure. 10.10(b)]. We observed a negative differential response in the output signal; the '11' logic state

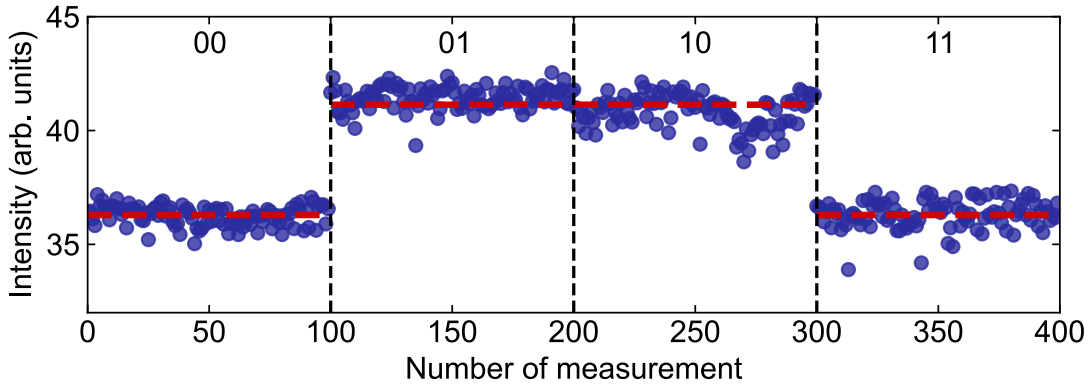

Figure 10.11: **All-optical implementation of XOR gate.** Output intensity of the all-optical XOR gate realized by combining the emission with the weighted inputs. Black dashed lines separate realizations of different inputs. Red dashed lines indicate the gate output intensity levels corresponding low and high states. Single bit of the input state is encoded by the pulse energy of the exciting laser beam: 2.0 pJ for low state ('0') and 7.9 pJ for high state ('1').

excited with the highest energy of the pulses had the weakest intensity. Based on the determined input and output intensities, w_1 and w_2 were calculated (with the assumption of $w_3 = 1$) and used to modify the signals. In the third stage, the weighted inputs were combined with the output on the CCD camera and realized for four configurations that gave the logic states of XOR gate (Figure. 10.11). We observed two distinct levels with low intensity for the logic states '00' and '11' and high intensity for the logic states '01' and '10'. The discrepancy between the expected values (marked with red dashed lines) and the measured result is negligible (less than 2% of the total signal). The created all-optical XOR gate required less than 16 pJ for an operation.

10.4 Summary

This chapter introduced the concept of binarized neural network. Such network was realized experimentally with the use of nonlinearities present in exciton polaritons. We created an opto-electronic binarized neural network and all-optical XOR logic gate.

In Sec. 10.1 we discussed the concept of two-dimensional nonlinearities. We showed, that even for nonlinear systems it is possible to not fullfill the two-dimensional nonlinear response. Then we presented the system having nonlinearities dependent on the two independent inputs.

In Sec. 10.2, we realized an opto-electronic neural network on exciton polaritons. We used response from the system of two spatially separated condensation sites to create nonlinearities. We performed the linear classification on nonlinear data and created millions of XOR logic gates. Then we built a binarized neural network with single hidden layer made of constructed nonlinear logic gates and performed classification of handwritten digits from the MNIST database with 96% accuracy rate.

In Sec. 10.3 we constructed an all-optical XOR gate. We used nonlinearities created in a single condensation site with a negative differential response and the two auxilliary paths to perform logic operations with high energy efficiency.

The above results show a huge potential for exciton polariton systems in performing energy efficient computation or information processing.

Chapter 11

Neural network based on time-delayed effects

In this chapter, we will demonstrate that the input can also be provided in a time-coded domain. This approach is likely to be very efficient in signal processing and speech recognition, but also requires a smaller number of nodes in a spatial dimension [160]. Time-delayed interactions, required for time encoding, have been realized in photonic systems [39, 161, 162] including the exciton polariton platform [96, 126].

We create a binarized neural network using time-dependent interactions. We show that the energy efficiency can be improved by using the system having larger nonlinearities. We make use of the nonequilibrium character of the polariton condensate. We use laser pulses delayed in time to create a condensate that coexists with the excitonic reservoir. The constructed neural network is used to perform speech recognition task.

11.1 Time delayed nonlinearities

In this chapter, we used two nonresonant pulsed laser beams, with pulses delayed in time, to create two condensates linked by interactions with a single excitonic reservoir. The scheme of the idea is presented in Figure 11.1. The excitation consisted of two pulses delayed in time. Both pulses excited nonresonantly the same position on the sample. The laser energy was tuned to the first higher energy Bragg minimum. The first pulse created a long-lived excitonic reservoir that depleted over time but still remained populated when the second pulse approached the sample. The exciton reservoir provided a time-dependent gain for the polaritons. The resulting emission consisted of two peaks, the second of which was modified by interactions via the reservoir. For the experiments presented in this chapter, we used the same experimental setup as in Figure 10.7. We were able to independently change the delay time between the pulses and the excitation power of each laser pulse.

The nonlinearities existing in the proposed approach are presented in Figure 11.2. We used two single pulses delayed in time and nonresonantly excited the sample. The emission at zero wave vector was collected on a streak camera. We observed two emission peaks (brown curve), with the second one much larger than the first one, despite the twice smaller power of the second pulse. To prove the

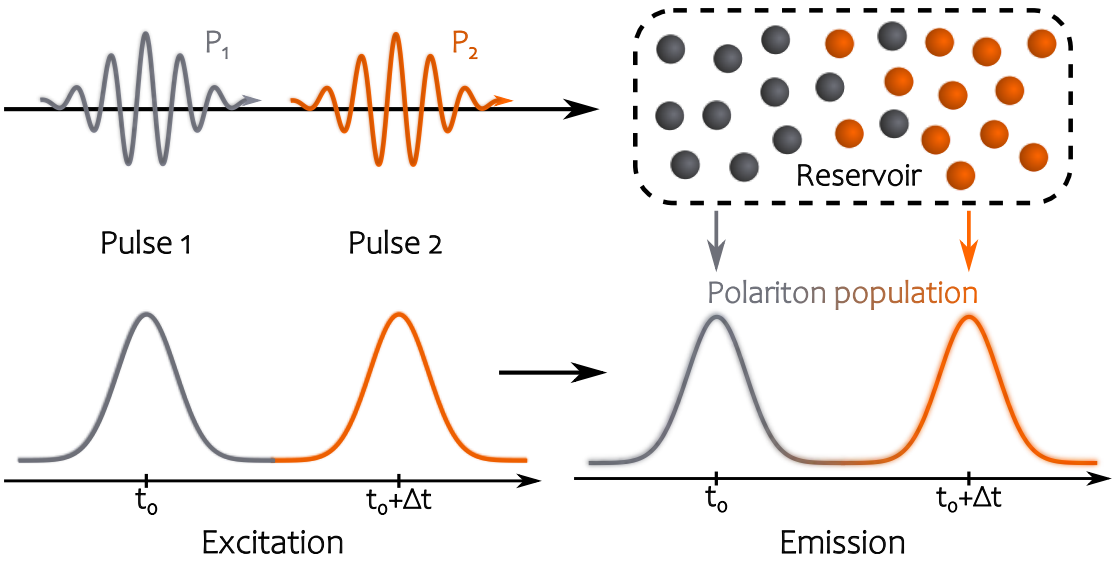

Figure 11.1: **Time-delayed interactions.** Schematic illustration of the time-delayed nonlinearities. Two laser pulses P_1 and P_2 delayed in time create a long-living excitonic reservoir. Relaxation from the reservoir leads to a nonlinear polariton population delayed in time.

nonlinear behavior, we excited the sample with the same pulses separately. The emission corresponding to the first pulse (blue curve) was the same in single- and two-pulse realizations. We observed a slow build-up of the emission in time and then a slow decay, suggesting that the condensation threshold was not reached. The observed polariton emission depends only on the excitation power of the first pulse. However, the emission assigned to the second pulse was much larger in the two-pulse realization. In the single pulse excitation, we created the excitonic reservoir that was depleting, leading to the creation of polaritons that decayed over time. In the two-pulse excitation, we created the excitonic reservoir within the first pulse and increased its population within the second pulse, exceeding the condensation threshold. This resulted in a nonlinear increase of the emission and decrease of the decay time because of more efficient depletion of the reservoir. The maximum intensity of the second emission peak depends not only on the excitation power but also on the delay time between the pulses. We performed the same experiment for different delays between the pulses and observed a nonlinear increase in the emission intensity from the second peak as presented in the inset of Figure 11.2. The highest nonlinear response was expected to occur when there was no delay between the pulses and there was no time to deplete the exciton reservoir. Indeed, the highest intensity was observed for the smallest time delay. For a very long delay between the pulses, there was no increase in the second peak intensity. This was due to the finite lifetime of the exciton reservoir. We reached the regime where the first pulse created a reservoir that was completely empty at the moment when the second pulse arrived. It created a second, independent reservoir that provided gain for the polaritons. Nevertheless, for time delays below 200 ps the intensity of the emission was enhanced.

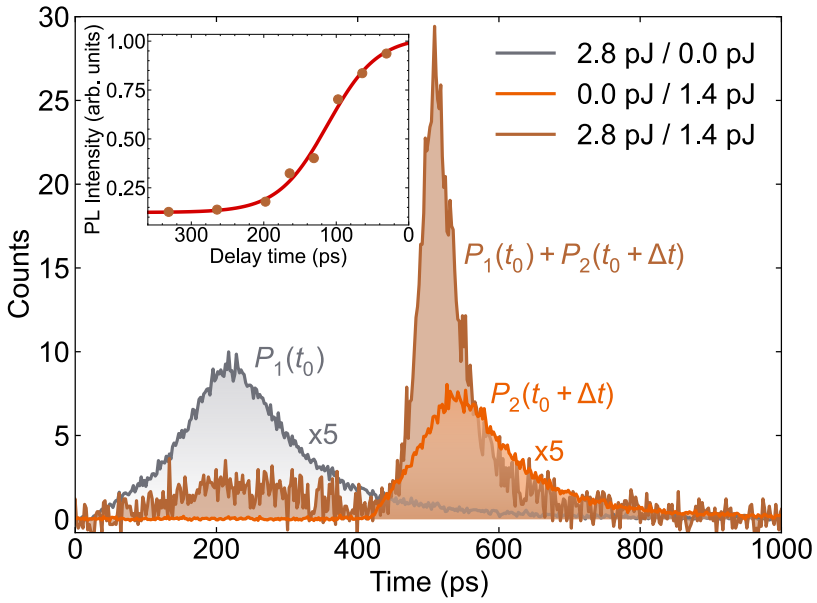

Figure 11.2: **Time-delayed nonlinearities.** Time-resolved emission from the single condensation-site excited with first pulse P_1 (gray), second pulse P_2 (orange) and both pulses P_1 and P_2 (brown) delayed in time. The single pulse responses were multiplied by 5 for better visibility. Inset shows the photoluminescence intensity of the second peak in the two-pulse excitation experiment for different delay time between the pulses.

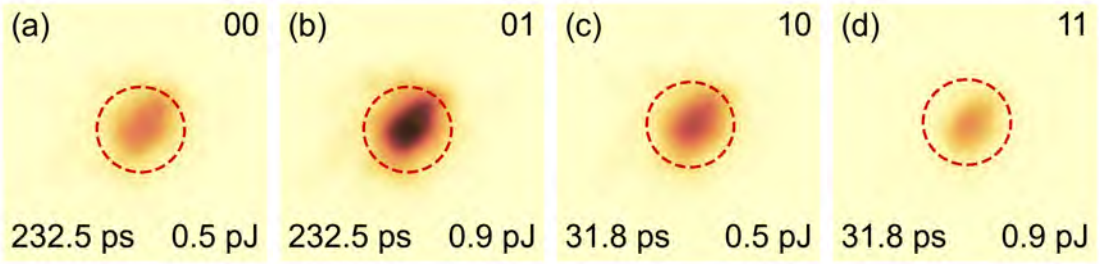

Figure 11.3: **Emission from single condensation site.** Real-space emission of a single polariton condensate excited with (a) long/low, (b) long/high, (c) short/low and (d) short/high pulses delay time/excitation power encoding '00', '01', '10' and '11' input states, respectively. Bottom annotations in the panels describe the delay time between the pulses (left) and pulse energy applied with each pulse to the condensation site.

11.2 XOR logic gate

The discussed time-delayed nonlinearities can be controlled using two parameters: the time delay between pulses and the excitation power. We constructed an opto-electronic XOR gate where the input space was created using these two parameters. In our approach, the two delayed pulses were focused on a single spot on a sample. The integrated time emission (60 ms) was measured using a CCD camera. To ensure the differential negative response, we excited the sample with a σ^+ polarized laser and measured the σ^- polarized emission. We expected a strong build-up of circular polarization above the condensation threshold and, at the same time, a decrease in the σ^- polarized emission signal. For this polarisation configuration, we obtained the highest nonlinearities. We realized four input

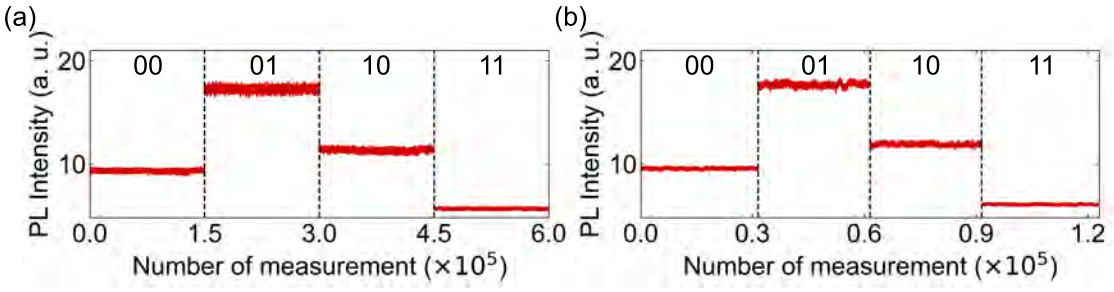

Figure 11.4: **Intensity of emission from single condensation site.** Intensity of emission from a condensation site excited with two pulses delayed in time. (a) Training and (b) testing set of data with four logic realizations marked on the top.

configurations '00', '01', '10', and '11' by changing the pulse energy and delay between the pulses. The first bit was encoded by the delay time between the pulses (31.8 ps for '1' and 232.5 ps for '0') and the second bit was encoded by the pulse energy of each pulse (0.9 pJ for '1' and 0.5 pJ for '0'). The exemplary emission observed for each realization was presented in Figure 11.3. For each configuration, we observed emission from a single excited spot. The emission was the lowest for the highest pulse energy (0.9 pJ per pulse) and the shortest time delay (31.8 ps). Here, the condensation threshold was reached and polaritons started to occupy the polarized condensate state σ^+ because of the σ^+ polarized laser. This resulted in a lower σ^- polarized emission compared to the other configurations. The condensate was observed also for the '10' state. The highest emission was reached for the '01' configuration realized by the pulse energy of 0.9 pJ and the time delay of 232.5 ps. Note that the pulse energies were lower than those used in an opto-electronic XOR gate realized in Section 10.2.

The experiment was repeated multiple times to produce data for the training and testing of a neural network and to determine the degree of nonlinearities. We calculated the mean intensity for the regions marked with dashed circles and presented in Figure 11.4. Collected data consisted of over 600,000 points in the training set and 120,000 points in the testing set. Both the training and the test data evidenced a negative differential response. We calculated the degree of nonlinearities and obtained $\eta_{train} \approx 62$ for training and $\eta_{test} \approx 57$ for test data. The lower degree of nonlinearities for the test data set was due to a larger data set, and therefore a greater variance. Nonlinearities were large enough to obtain the opto-electronic XOR gate with 100% accuracy. What is interesting is that the degree of nonlinearities was substantial despite the time integration of the signal on a CCD camera.

11.3 Ultrafast XOR gate operation

To test the time scale of the XOR gate operations, we performed an experiment with time-resolved detection on a streak camera. The two-dimensional input space was encoded by pulse energies of two beams focused on the same position on the sample and the delay time between them. We performed a realization in which the condensation was achieved only for the '11' state, and for other states, the system was in a linear regime. This was obtained by keeping the same detec-

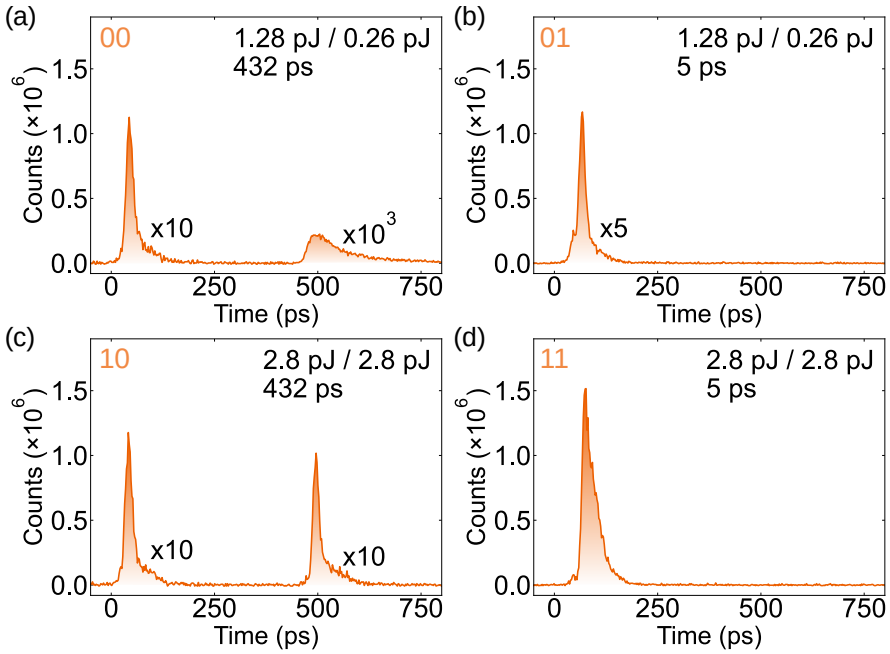

Figure 11.5: **Ultrafast XOR operation.** Time-resolved emission from the single condensation-site excited with two pulses delayed in time. The delay time between the pulses and their pulse energies are marked on top right. The input states encoded by the two pulses are marked on each panel on top left. Signal on panels (a-c) was multiplied by marked factors for better visibility.

tion polarization (σ^+) as the polarization of the excitation laser. In this way, we were able to estimate the time scales of the XOR operation when the excitonic reservoir is slowly depleted, providing gain for polaritons, or rapidly reduced by polariton condensate. The time-resolved emission for four input configurations is illustrated in Figure 11.4. The '00' state was encoded by a low excitation power (1.28 pJ/0.26 pJ) and a long delay (432 ps) between pulses. For this input state, we observed two emission peaks of small intensity and a long decay time indicating the formation of low density exciton polaritons. Similarly, the two emission peaks, but of higher intensity, were observed for a '10' state realized by the large excitation power (2.8 pJ/2.8 pJ) and the long delay (432 ps) between the pulses. For input states '01' and '11', the second bit was encoded by the small delay time (5 ps) between the pulses. For these states, we observed a single emission peak. The output for the '11' input state was significantly more intense than for the other states. In this state, the polariton condensation was achieved, which resulted in a nonlinear increase of the emission. We calculated the integral of the first peak for each input configuration and used it to determine the degree of nonlinearities. The obtained η was approximately 70, which is essentially higher than the value needed to obtain a 100% accuracy rate of the XOR logic gate.

11.4 Speech recognition task

The time-delayed phenomena-based XOR logic gates were used to perform a speech recognition task. The whole procedure was implemented on a computer by Dr. Andrzej Opala. The binarized neural network scheme used for speech recog-

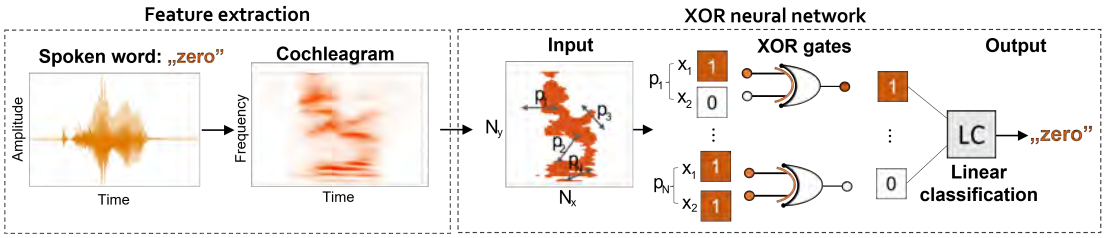

Figure 11.6: **Speech recognition task.** Scheme of the process of speech recognition. Input is prepared by transformation of the audio signal into a cochleagram and binarization. The randomly selected pixel pairs p_i are given as inputs to consecutive XOR logic gates forming a single hidden layer. The output of the logic gates is linearly classified in the output layer. Illustration produced by Dr Andrzej Opala.

nition is presented in Figure 11.6. We implemented the spoken words from the TI 46-Word data set (provided by the Linguistic Data Consortium) [163]. In this data set, the training input data consist of ten digits (0 to 9) and twenty words spoken by five female voices. The testing set contains the same words spoken by 8 other women. In our analysis, we used 500 training and 1275 testing samples in the form of audio waveform files. We transformed the audio signal from an amplitude change in time into a frequency change into cochleagrams using two different methods. The first method was to use the Fourier transform (FT) to change the amplitude into the frequency. Another was a Lyon cochlear-ear model (LCM), which is a nonlinear transformation that mimics the processes taking place in the biological cochlear. Then the cochleagram was binarized, and the intensities of random pairs of pixels were encoding the inputs in the single XOR layer. The output of the XOR logic gates was linearly classified to obtain the weigths in the training process. We considered time-frequency maps of size (16×16), (32×32) and (64×64). Since the transformations from the time-amplitude to frequency-time map were nonlinear, we compared the classification accuracy for both transformation methods while using a single hidden layer made of 5000 XOR logic gates (XOR) and while using linear classification only (LC). The obtained accuracies are given in Table 11.1. The nonlinearities implemented electronically by creating a cochleagram allowed us to obtain the classification accuracies above 75% for the Fourier transform and above 86% for the Lyon cochlear-ear model. An improvement in classification was observed for an increase in the size of the cochleagram. The obtained accuracies give little room for improvement, making the task even more difficult. However, with the use of the single hidden layer made of XOR logic gates, we were able to progress in speech recognition. In the best case, we improved the classification by 4.84%.

11.5 Summary

In this chapter, we created a neural network based on time-delayed effects. We created a strongly nonlinear system and used it to construct a binarized network.

In Sec. 11.1 we discussed the nonlinearities created through the time-delayed interactions. We showed the mechanism behind the nonlinear response in a constructed system.

In Sec. 11.2, we used the time-delayed nonlinearities to create an opto-electronic

Table 11.1: Classification accuracy determined using a network with a linear classifier only (LC) and with a network including a hidden layer of 5000 XOR gates (XOR). Parameter Δ is the improvement of the classification accuracy achieved by transforming the binarized data by the XOR layer. Each value is an average of five different realizations of neural network teaching. Each realization corresponds to a different selection of randomly selected pixel pairs.

Size of time-frequency map			(16×16)	(32×32)	(64×64)
Methods	XOR	FT (%)	76.08	87.16	94.06
		LCM (%)	90.96	95.50	96.44
	LC	FT (%)	75.50	86.12	92.72
		LCM (%)	86.12	94.40	95.50
Δ (%)		Δ_{FT} (%)	0.58	1.04	1.34
		Δ_{LCM} (%)	4.84	1.10	0.94

XOR logic gate. We performed linear classification on a computer using the nonlinear data collected on an optical table. We obtained 100% accuracy of XOR operation and an energy efficiency below 2 pJ.

In Sec. 11.3 was dedicated to the operation time of the XOR gate. Using the time-resolved measurements we confirmed the XOR operation in a time below 450 ps.

In Sec. 11.4 we created a XOR gates based neural network and performed a speech recognition task. We obtained the classification accuracy up to 96%.

The introduced system manifests strong nonlinear effects allowing for a drastic reduction of energy consumption of the neural network. Apart from that, it operates on sub-nanosecond timescales with potential to improve even two orders of magnitude.

Chapter 12

Outlook

Strong nonlinearities and small effective mass together with a short lifetime make exciton polaritons a very promising system for ultrafast and energy efficient computing. Presented in this thesis binarized opto-electronic neural networks already compete with the state-of-the-art hardware implementations. We compared the energy efficiencies and performance densities of our device with other systems in Figure. 12.1. The energy efficiency of the realized all-optical XOR was of 16 pJ per bit. The created opto-electronic exciton polariton network performance is marked with the yellow dot. The network is distinguished by an exceptional performance density that is orders of magnitude higher than other realizations. In terms of energy efficiency, our exciton polariton network is placed in a region similar to that of other state-of-the-art neural networks. However, in our case, there are many areas where improvements can be made. The experiment was performed with nonresonant excitation, which is associated with large energy losses. Performing exactly the same experiment with resonant excitation should increase the energy efficiency by orders of magnitude. As discussed in [112], two cases can be distinguished. In case A, a large neural network with idealized parameters possible with the use of the best available optical elements has been assumed. In case B, the more realistic case with a smaller neural network and easily accessible optical elements has been considered. As presented in Figure. 12.1 both energy efficiency and performance density can be substantially improved.

Neural networks require nonlinearities that can be implemented in many ways. In this thesis, we proved that strong nonlinearities can be produced using many different phenomena. The neural network can be constructed on the basis of magnetic effects. Importantly, because of the artificial field that exists in the microcavity, exciton polariton condensates do not require an external magnetic field to manifest extraordinary spin properties. These properties can be used to create two-dimensional nonlinearities resulting from the nonlinear change in emission intensity in a selected circular polarization.

Another very promising approach is to process time-coded data by neural networks realizing time-delayed phenomena. Our idea to create a reservoir-mediated neural network allows for energy efficient and ultrafast operation. Such a solution does not require a large number of nodes in space because they can be created in a time domain [160]. Dynamical neural networks can also be realized with the use of a feedback loop, which is a source of strong nonlinearities. This approach can be easily scalable and energetically efficient because of the reuse of emission in excitation.

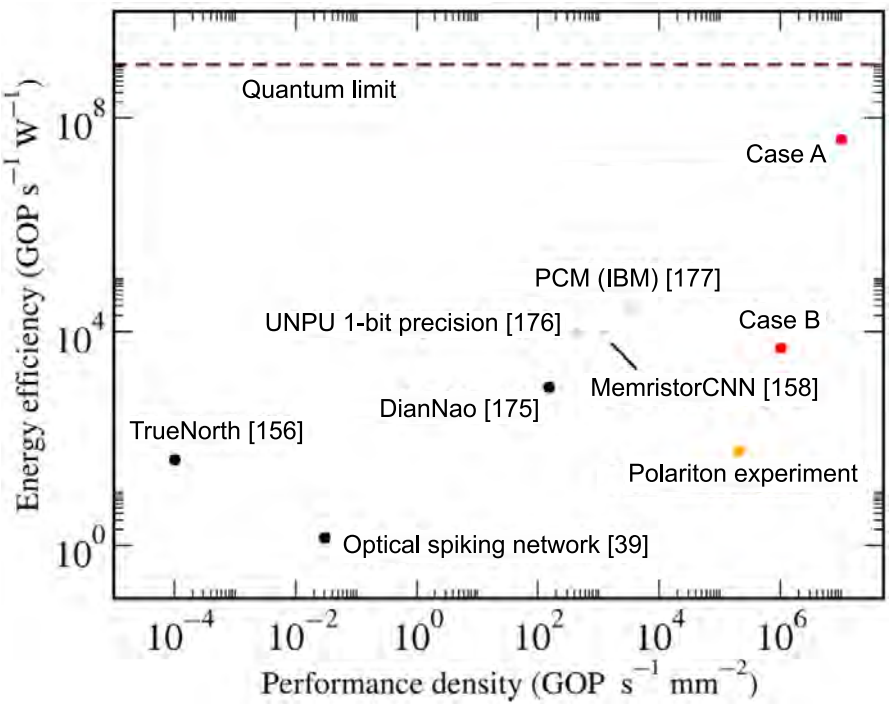

Figure 12.1: **Energy efficiency and performance density of neural networks.** Comparison of energy-efficiency and performance density of polariton neural networks (red dots) with non-polariton systems [39, 156, 158, 175–177].Gray points correspond to systems with estimations of only a specific part of the network [158, 176], or the inference partly realized by software [176, 177]. The orange dot corresponds to the experiment realized in chapter 10. The dashed line is the single-photon quantum limit for optics. OP on the axes stands for operation. Figure reprinted from [112].

The short-term challenge at this moment is to achieve operation at room temperature. This can be easily achieved by replacing CdTe-based quantum wells with perovskites [164], polymers [165], proteins [166], dyes [167], or semiconductors with large exciton binding energy such as ZnO [168] or GaN [169]. However, it is still unclear how to make connections between the nonlinear nodes in polariton neural networks despite many possibilities such as optically realized vector-matrix multiplication [43, 170–174]. The scalability problem can also be resolved by implementing convolutional operations [40, 148, 172]. Despite the challenges, the field is very interesting and promising, as shown by the results achieved in terms of speed and energy efficiency.

Chapter 13

Publications of the author

Publications and patents as part of this work

1. **R. Mirek**, M. Furman, M. Król, B. Seredyński, K. Łempicka-Mirek, K. Tyszka, J. Suffczyński, W. Pacuski, M. Matuszewski, J. Szczytko, and B. Piętka, Spin polarization of exciton-polariton condensate in a photonic synthetic effective magnetic field, to be submitted.

2. **R. Mirek**, A. Opala, M. Furman, M. Król, K. Tyszka, B. Seredyński, W. Pacuski, J. Suffczyński, J. Szczytko, M. Matuszewski, and B. Piętka, Neural networks based on ultrafast time-delayed effects in exciton-polaritons, Physical Review Applied **17,** 054037 (2022).

3. **R. Mirek**, A. Opala, P. Comaron, M. Furman, M. Król, K. Tyszka, B. Seredyński, D. Ballarini, D. Sanvitto, T. C. H. Liew, W. Pacuski, J. Suffczyński, J. Szczytko, M. Matuszewski, and B. Piętka, Neuromorphic Binarized Polariton Networks, Nano Letters **21,** 9, 3715–3720 (2021).

4. M. Matuszewski, B. Piętka, A. Opala, J. Szczytko, **R. Mirek**, K. Tyszka, M. Król, M. Furman, J. Suffczyński, W. Pacuski and B. Seredyński, Urządzenie implementujące polarytonową optyczną sieć neuronową oraz polarytonowa optyczna sieć neuronowa. Polish patent application, No. P.438170, 15 June 2021.

Further publications and patents

5. M. Matuszewski, A. Opala, **R. Mirek**, M. Furman, M. Król, K. Tyszka, T. C. H. Liew, D. Ballarini, D. Sanvitto, J. Szczytko, B. Piętka, Energy-Efficient Neural Network Inference with Microcavity Exciton Polaritons, Physical Review Applied **16,** 024045 (2022).

6. K. Tyszka, M. Furman, **R. Mirek**, M. Król, A. Opala, B. Seredyński, J. Suffczyński, W. Pacuski, M. Matuszewski, J. Szczytko, B. Piętka, Leaky Integrate-and-Fire Mechanism in Exciton-Polariton Condensates for Photonic Spiking Neurons Laser & Photonics Reviews, 2100660 (2022).

7. K. Rechcińska, M. Król, R. Mazur, P. Morawiak, **R. Mirek**, K. Łempicka, W. Bardyszewski, M. Matuszewski, P. Kula, W. Piecek, P. G. Lagoudakis,

B. Piętka,J. Szczytko, Engineering Spin-Orbit Synthetic Hamiltonians in Liquid Crystal Optical Cavities, Science **366,** 6466 (2019).

8. M. Król, K. Rechcińska, K. Nogajewski, M. J. Grzeszczyk, K. Łempicka, **R. Mirek**, S. Piotrowska, K. Watanabe, T. Taniguchi, M. Molas, M. Potemski, J. Szczytko, B. Pietka, Exciton-polaritons in multilayer WSe_2 in a planar microcavity, 2D Materials **7,** 015006 (2019)

9. M. Król, K. Lekenta, **R. Mirek**, K. Łempicka, D. Stephan, K. Nogajewski, M. R. Molas, A. Babiński, M. Potemski, J. Szczytko, B. Piętka, Valley polarization of exciton-polaritons in monolayer WSe_2 in a tunable microcavity, Nanoscale **11,** 9574 (2019).

10. M. Król, **R. Mirek**, D. Stephan, K. Lekenta, J.-G. Rousset, W. Pacuski, A. V. Kavokin, M. Matuszewski, J. Szczytko, B. Piętka, Giant spin Meissner effect in a nonequilibrium exciton-polariton gas, Physical Review B **99,** 115318 (2019).

11. K. Lekenta, M. Król, **R. Mirek**, K. Łempicka, D. Stephan, R. Mazur, P. Morawiak, P. Kula, W. Piecek, P. G. Lagoudakis, B. Piętka, J. Szczytko, Tunable optical-spin Hall effect in a liquid crystal microcavity, Light: Science & Applications **7,** 74 (2018).

12. J. M. Braun, H. Schneider, M. Helm, **R. Mirek**, L. A. Boatner, R. E. Marvel, R. F. Haglund Jr, A. Pashkin, Ultrafast response of photoexcited carriers in VO_2 at high-pressure, New Journal of Physics **20,** 083003 (2018).

13. M. Król, **R. Mirek**, K. Lekenta, J.-G. Rousset, D. Stephan, M. Nawrocki, M. Matuszewski, J. Szczytko, W. Pacuski, B. Piętka, Spin polarized semimagnetic exciton-polariton condensate in magnetic field, Scientific Reports **8,** 6694 (2018).

14. B. Seredyński, M. Król, P. Starzyk, **R. Mirek**, M. Ściesiek, K. Sobczak, J. Borysiuk, D. Stephan, J.-G. Rousset, J. Szczytko, B. Pietka, W. Pacuski, (Cd,Zn,Mg)Te based microcavity on MgTe sacrificial buffer: Growth, lift-off and transmission studies of polaritons, Physical Review Materials **2,** 043406 (2018).

15. J-G. Rousset, B. Piętka, M. Król, **R. Mirek**, K. Lekenta, J. Szczytko, W. Pacuski, M. Nawrocki, Magnetic field effect on the lasing threshold of a semimagnetic polariton condensate, Physical Review B **96,** 125403 (2017).

16. B. Piętka, N. Bobrovska, D. Stephan, M. Teich, M. Król, S. Winnerl, A. Pashkin, **R. Mirek**, K. Lekenta, F. Morier-Genoud, H. Schneider, B. Deveaud, M. Helm, M. Matuszewski, J. Szczytko, Doubly Dressed Bosons: Exciton Polaritons in a Strong Terahertz Field, Physical Review Letters **119,** 077403 (2017).

17. B. Piętka, M. Molas, N. Bobrovska, M. Król, **R. Mirek**, K. Lekenta, P. Stepnicki, F. Morier-Genoud, J. Szczytko, B. Deveaud, M. Matuszewski, M. Potemski, 2s exciton-polariton revealed in an external magnetic field, Physical Review B **96,** 081402 (2017).

18. **R. Mirek**, M. Król, K. Lekenta, J-G. Rousset, M. Nawrocki, M. Kulczykowski, M. Matuszewski, J. Szczytko, W. Pacuski, B. Piętka, Angular dependence of giant Zeeman effect for semimagnetic cavity polaritons, Physical Review B **95,** 085429 (2017).

19. J-G. Rousset, B. Piętka, M. Król, **R. Mirek**, K. Lekenta, J. Szczytko, J. Borysiuk, J. Suffczyński, T. Kazimierczuk, M. Goryca, T. Smoleński, P. Kossacki, M. Nawrocki, W. Pacuski, Strong coupling and polariton lasing in Te based microcavities embedding (Cd, Zn)Te quantum wells, Applied Physics Letters **107,** 201109 (2015).

20. J. Szczytko, K. Lekenta, B. Piętka, M. Król, **R. Mirek**, D. Stephan, W. Piecek, R. Mazur, P. Morawiak, Tunable optical microcavity for modulation and generation of specific radiation. Polish patent application, No. P.427131, 17 September 2019.

List of Figures

References

[1]G. H. Wannier, "The structure of electronic excitation levels in insulating crystals", Phys. Rev. **52**, 191–197 (1937).

[2]J. Rarity and C. Weisbuch, eds., *Microcavities and photonic bandgaps: physics and applications* (Springer Netherlands, 1996).

[3]V. Savona, L. Andreani, P. Schwendimann, and A. Quattropani, "Quantum well excitons in semiconductor microcavities: unified treatment of weak and strong coupling regimes", Solid State Communications **93**, 733–739 (1995).

[4]J. J. Hopfield, "Theory of the contribution of excitons to the complex dielectric constant of crystals", Physical Review **112**, 1555–1567 (1958).

[5]C. Ciuti, V. Savona, C. Piermarocchi, A. Quattropani, and P. Schwendimann, "Role of the exchange of carriers in elastic exciton-exciton scattering in quantum wells", Phys. Rev. B **58**, 7926–7933 (1998).

[6]S. Schumacher, N. H. Kwong, and R. Binder, "Influence of exciton-exciton correlations on the polarization characteristics of polariton amplification in semiconductor microcavities", Phys. Rev. B **76**, 245324 (2007).

[7]M. Wouters, "Resonant polariton-polariton scattering in semiconductor microcavities", Phys. Rev. B **76**, 045319 (2007).

[8]B. Sermage, S. Long, I. Abram, J. Y. Marzin, J. Bloch, R. Planel, and V. Thierry-Mieg, "Time-resolved spontaneous emission of excitons in a microcavity: behavior of the individual exciton-photon mixed states", Phys. Rev. B **53**, 16516–16523 (1996).

[9]Y. Sun, Y. Yoon, M. Steger, G. Liu, L. N. Pfeiffer, K. West, D. W. Snoke, and K. A. Nelson, "Direct measurement of polariton–polariton interaction strength", Nature Physics **13**, 870–875 (2017).

[10]D. Langer and S. Ibuki, "Zero-Phonon Lines and Photon Coupling in ZnS:Mn", Physical Review **138** (1965).

[11]J. M. Baranowski, J. W. Allen, and P. G. L., "Crystal-Field Spectra of $3d^n$ Impurities in II-VI and III-V Compound Semiconductors", Physical Review **160**, 627–632 (1967).

[12]H. A. Weakliem, "Optical Spectra of Ni^{2+}, Co^{2+}, and Cu^{2+} in Tetrahedral Sites in Crystals", The Journal of Chemical Physics **36**, 2117–2140 (1962).

[13]R. T. Holm and J. K. Furdyna, "Observation of helicon-excited Electron Paramagnetic Resonance in a high-mobility semiconductor", Solid State Communications **15**, 1459–1462 (1974).

[14]R. T. Holm and J. K. Furdyna, "Microwave helicon propagation and helicon-excited electron paramagnetic resonance in $Hg_{1-x}Mn_xTe$", Physical Review B **15** (1977).

[15]G. Bastard, C. Rigaux, and A. Mycielski, "Giant spin splitting induced by exchange interactions in $Hg_{1-k}Mn_kTe$ mixed crystals", Physica Status Solidi (B) **79**, 585–593 (1977).

[16]A. Komarov, S. M. Ryabchenko, and O. V. Terletskii, "Magneto-optical investigations of the exciton band in CdTe: Mn2+", Journal of Experimental and Theoretical Physics **46**, 606–618 (1977).

[17]J. Gaj, R. R. Gałązka, and M. Nawrocki, "Giant exciton Faraday rotation in $Cd_{1-x}Mn_xTe$ mixed crystals", Solid State Communications **25**, 193–195 (1978).

[18]J. Gaj, R. Planel, and G. Fishman, "Relation of magneto-optical properties of free excitons to spin alignment of Mn^{2+} ions in $Cd_{1-x}Mn_xTe$", Solid State Communication **29**, 435–438 (1979).

[19]M. Goryca, T. Kazimierczuk, M. Nawrocki, A. Golnik, J. A. Gaj, P. Kossacki, P. Wojnar, and G. Karczewski, "Optical manipulation of a single Mn spin in a cdte-based quantum dot", Phys. Rev. Lett. **103**, 087401 (2009).

[20]C. Le Gall, L. Besombes, H. Boukari, R. Kolodka, J. Cibert, and H. Mariette, "Optical spin orientation of a single manganese atom in a semiconductor quantum dot using quasiresonant photoexcitation", Phys. Rev. Lett. **102**, 127402 (2009).

[21]A. Brunetti, M. Vladimirova, D. Scalbert, R. André, D. Solnyshkov, G. Malpuech, I. A. Shelykh, and A. V. Kavokin, "Coherent spin dynamics of exciton-polaritons in diluted magnetic microcavities", Phys. Rev. B **73**, 205337 (2006).

[22]B. Piętka, D. Zygmunt, M. Król, M. R. Molas, A. A. L. Nicolet, F. Morier-Genoud, J. Szczytko, J. Łusakowski, P. Zięba, I. Tralle, P. Stępnicki, M. Matuszewski, M. Potemski, and B. Deveaud, "Magnetic field tuning of exciton-polaritons in a semiconductor microcavity", Phys. Rev. B **91**, 075309 (2015).

[23]B. Piętka, M. R. Molas, N. Bobrovska, M. Król, R. Mirek, K. Lekenta, P. Stępnicki, F. Morier-Genoud, J. Szczytko, B. Deveaud, M. Matuszewski, and M. Potemski, "2s Exciton-polariton revealed in an external magnetic field", Phys. Rev. B **96**, 081402 (2017).

[24]A. V. Larionov, V. D. Kulakovskii, S. Höfling, C. Schneider, L. Worschech, and A. Forchel, "Polarized nonequilibrium Bose-Einstein condensates of spinor exciton polaritons in a magnetic field", Phys. Rev. Lett. **105**, 256401 (2010).

[25]P. Walker, T. C. H. Liew, D. Sarkar, M. Durska, A. P. D. Love, M. S. Skolnick, J. S. Roberts, I. A. Shelykh, A. V. Kavokin, and D. N. Krizhanovskii, "Suppression of zeeman splitting of the energy levels of exciton-polariton condensates in semiconductor microcavities in an external magnetic field", Phys. Rev. Lett. **106**, 257401 (2011).

[26]J. Fischer, S. Brodbeck, A. V. Chernenko, I. Lederer, A. Rahimi-Iman, M. Amthor, V. D. Kulakovskii, L. Worschech, M. Kamp, M. Durnev, C. Schneider, A. V. Kavokin, and S. Höfling, "Anomalies of a Nonequilibrium Spinor Polariton Condensate in a Magnetic Field", Physical Review Letters **112**, 1–5 (2014).

[27]C. Sturm, D. Solnyshkov, O. Krebs, A. Lemaítre, I. Sagnes, E. Galopin, A. Amo, G. Malpuech, and J. Bloch, "Nonequilibrium polariton condensate in a magnetic field", Phys. Rev. B **91**, 155130 (2015).

[28]J. Kasprzak, M. Richard, S. Kundermann, A. Baas, P. Jeambrun, J. M. J. Keeling, F. M. Marchetti, M. H. Szymańska, R. André, J. L. Staehli, V. Savona, P. B. Littlewood, B. Deveaud, and Le Si Dang, "Bose-Einstein condensation of exciton polaritons", Nature **443**, 409–414 (2006).

[29]S. Kéna-Cohen and S. R. Forrest, "Room-temperature polariton lasing in an organic single-crystal microcavity", Nature Photonics **4**, 371–375 (2010).

[30]W. S. McCulloch and W. Pitts, "A logical calculus of the ideas immanent in nervous activity", The Bulletin of Mathematical Biophysics **5**, 115–133 (1943).

[31]F. Rosenblatt, *The perceptron - a perceiving and recognizing automaton*, tech. rep. 85-460-1 (Cornell Aeronautical Laboratory, Ithaca, New York, Jan. 1957).

[32]M. Minsky and S. Papert, *Perceptrons: an introduction to computational geometry* (MIT Press, Cambridge, MA, USA, 1969).

[33]J. Fürnkranz, P. K. Chan, S. Craw, C. Sammut, W. Uther, A. Ratnaparkhi, X. Jin, J. Han, Y. Yang, K. Morik, M. Dorigo, M. Birattari, T. Stützle, P. Brazdil, R. Vilalta, C. Giraud-Carrier, C. Soares, J. Rissanen, R. A. Baxter, I. Bruha, R. A. Baxter, G. I. Webb, L. Torgo, A. Banerjee, H. Shan, S. Ray, P. Tadepalli, Y. Shoham, R. Powers, Y. Shoham, R. Powers, G. I. Webb, S. Ray, S. Scott, H. Blockeel, and L. De Raedt, "Mean squared error", in *Encyclopedia of machine learning* (Springer US, 2011), pp. 653–653.

[34]H. Sharma, J. Park, N. Suda, L. Lai, B. Chau, V. Chandra, and H. Esmaeilzadeh, "Bit fusion: bit-level dynamically composable architecture for accelerating deep neural network", in 2018 ACM/IEEE 45th annual international symposium on computer architecture (ISCA) (June 2018).

[35]M. Rastegari, V. Ordonez, J. Redmon, and A. Farhadi, "Xnor-net: imagenet classification using binary convolutional neural networks", in Computer vision - eccv 2016, edited by B. Leibe, J. Matas, N. Sebe, and M. Welling (2016), pp. 525–542.

[36]A. Mehonic and A. J. Kenyon, "Brain-inspired computing needs a master plan", Nature **604**, 255–260 (2022).

[37]M. M. Waldrop, "The chips are down for Moore's law", Nature **530**, 144–147 (2016).

[38]Y. Shen, N. C. Harris, S. Skirlo, M. Prabhu, T. Baehr-Jones, M. Hochberg, X. Sun, S. Zhao, H. Larochelle, D. Englund, and M. Soljačić, "Deep learning with coherent nanophotonic circuits", Nature Photonics **11**, 441–446 (2017).

[39]J. Feldmann, N. Youngblood, C. D. Wright, H. Bhaskaran, and W. H. P. Pernice, "All-optical spiking neurosynaptic networks with self-learning capabilities", Nature **569**, 208–214 (2019).

[40]J. Feldmann, N. Youngblood, M. Karpov, H. Gehring, X. Li, M. Stappers, M. L. Gallo, X. Fu, A. Lukashchuk, A. S. Raja, J. Liu, C. D. Wright, A. Sebastian, T. J. Kippenberg, W. H. P. Pernice, and H. Bhaskaran, "Parallel convolutional processing using an integrated photonic tensor core", Nature **589**, 52–58 (2021).

[41]X. Lin, Y. Rivenson, N. T. Yardimci, M. Veli, Y. Luo, M. Jarrahi, and A. Ozcan, "All-optical machine learning using diffractive deep neural networks", Science **361**, 1004–1008 (2018).

[42]Z. Chen, A. Sludds, R. Davis, I. Christen, L. Bernstein, T. Heuser, N. Heermeier, J. A. Lott, S. Reitzenstein, R. Hamerly, and D. Englund, *Deep learning with coherent VCSEL neural networks*, 2022.

[43]J. Bueno, S. Maktoobi, L. Froehly, I. Fischer, M. Jacquot, L. Larger, and D. Brunner, "Reinforcement learning in a large-scale photonic recurrent neural network", Optica **5**, 756–760 (2018).

[44]B. Seredyński, M. Król, P. Starzyk, R. Mirek, M. Ściesiek, K. Sobczak, J. Borysiuk, D. Stephan, J.-G. Rousset, J. Szczytko, B. Pi ętka, and W. Pacuski, "(Cd,Zn,Mg)Te-based microcavity on MgTe sacrificial buffer: Growth, lift-off, and transmission studies of polaritons", Phys. Rev. Materials **2**, 043406 (2018).

[45]N. Y. Kim, K. Kusudo, C. Wu, N. Masumoto, A. Löffler, S. Höfling, N. Kumada, L. Worschech, A. Forchel, and Y. Yamamoto, "Dynamical d-wave condensation of exciton–polaritons in a two-dimensional square-lattice potential", Nature Physics **7**, 681–686 (2011).

[46]A. Amo and J. Bloch, "Exciton-polaritons in lattices: a non-linear photonic simulator", Comptes Rendus Physique **17**, 934–945 (2016).

[47]N. G. Berloff, M. Silva, K. Kalinin, A. Askitopoulos, J. D. Töpfer, P. Cilibrizzi, W. Langbein, and P. G. Lagoudakis, "Realizing the classical XY Hamiltonian in polariton simulators", Nat. Mater. **16**, 1120 (2017).

[48]D. Ballarini, A. Gianfrate, R. Panico, A. Opala, S. Ghosh, L. Dominici, V. Ardizzone, M. D. Giorgi, G. Lerario, G. Gigli, T. C. H. Liew, M. Matuszewski, and D. Sanvitto, "Polaritonic neuromorphic computing outperforms linear classifiers", Nano Letters **20**, 3506–3512 (2020).

[49]J. D. Töpfer, I. Chatzopoulos, H. Sigurdsson, T. Cookson, Y. G. Rubo, and P. G. Lagoudakis, "Engineering spatial coherence in lattices of polariton condensates", Optica **8**, 106 (2021).

[50]J. Sadowski, H. Mariette, A. Wasiela, R. André, Y. Merle d'Aubigné, and T. Dietl, "Magnetic tuning in excitonic bragg structures of (Cd,Mn)Te/(Cd,Zn,Mg)Te", Phys. Rev. B **56**, R1664–R1667 (1997).

[51]H. Ulmer-Tuffigo, F. Kany, G. Feuillet, R. Langer, J. Bleuse, and J. Pautrat, "Magnetic tuning of resonance in semimagnetic semiconductor microcavities", Journal of Crystal Growth **159**, Proceedings of the seventh international conference on II-VI compouds and devices, 605–608 (1996).

[52]M. Haddad, R. André, R. Frey, and C. Flytzanis, "Enhanced Faraday rotation in an asymmetric semiconductor microcavity", Solid State Communications **111**, 61–65 (1999).

[53]R. Mirek, M. Król, K. Lekenta, J.-G. Rousset, M. Nawrocki, M. Kulczykowski, M. Matuszewski, J. Szczytko, W. Pacuski, and B. Piętka, "Angular dependence of giant Zeeman effect for semimagnetic cavity polaritons", Phys. Rev. B **95**, 085429 (2017).

[54]J.-G. Rousset, B. Piętka, M. Król, R. Mirek, K. Lekenta, J. Szczytko, W. Pacuski, and M. Nawrocki, "Magnetic field effect on the lasing threshold of a semimagnetic polariton condensate", Phys. Rev. B **96**, 125403 (2017).

[55]M. Król, R. Mirek, D. Stephan, K. Lekenta, J.-G. Rousset, W. Pacuski, A. V. Kavokin, M. Matuszewski, J. Szczytko, and B. Piętka, "Giant spin Meissner effect in a nonequilibrium exciton-polariton gas", Phys. Rev. B **99**, 115318 (2019).

[56]M. Król, R. Mirek, K. Lekenta, J.-G. Rousset, D. Stephan, M. Nawrocki, M. Matuszewski, J. Szczytko, W. Pacuski, and B. Piętka, "Spin polarized semimagnetic exciton-polariton condensate in magnetic field", Scientific Reports **8**, 10.1038/s41598-018-25018-2 (2018).

[57]J.-G. Rousset, B. Piętka, M. Król, R. Mirek, K. Lekenta, J. Szczytko, J. Borysiuk, J. Suffczyński, T. Kazimierczuk, M. Goryca, T. Smoleński, P. Kossacki, M. Nawrocki, W. Pacuski, B. Piętka, M. Król, R. Mirek, K. Lekenta, J. Szczytko, J. Borysiuk, J. Suffczyński, T. Kazimierczuk, M. Goryca, T. Smoleński, P. Kossacki, M. Nawrocki, and W. Pacuski, "Strong coupling and polariton lasing in te based microcavities embedding (Cd,Zn)Te quantum wells", Appl. Phys. Lett. **107**, 201109 (2015).

[58]I. A. Shelykh, A. V. Kavokin, Y. G. Rubo, T. C. H. Liew, and G. Malpuech, "Polariton polarization-sensitive phenomena in planar semiconductor microcavities", Semiconductor Science and Technology **25**, 013001 (2010).

[59]V. G. Sala, F. Marsault, M. Wouters, E. Galopin, I. Sagnes, A. Lemaître, J. Bloch, and A. Amo, "Stochastic precession of the polarization in a polariton laser", Phys. Rev. B **93**, 115313 (2016).

[60]F. P. Laussy, I. A. Shelykh, G. Malpuech, and A. Kavokin, "Effects of Bose-Einstein condensation of exciton polaritons in microcavities on the polarization of emitted light", Phys. Rev. B **73**, 035315 (2006).

[61]I. A. Shelykh, T. C. H. Liew, and A. V. Kavokin, "Interplay between superfluidity and magnetic self-trapping of exciton polaritons", Phys. Rev. B **80**, 201306 (2009).

[62]H. Ohadi, A. Dreismann, Y. G. Rubo, F. Pinsker, Y. del Valle-Inclan Redondo, S. I. Tsintzos, Z. Hatzopoulos, P. G. Savvidis, and J. J. Baumberg, "Spontaneous spin bifurcations and ferromagnetic phase transitions in a spinor exciton-polariton condensate", Phys. Rev. X **5**, 031002 (2015).

[63]A. Askitopoulos, K. Kalinin, T. C. H. Liew, P. Cilibrizzi, Z. Hatzopoulos, P. G. Savvidis, N. G. Berloff, and P. G. Lagoudakis, "Nonresonant optical control of a spinor polariton condensate", Phys. Rev. B **93**, 205307 (2016).

[64]L. Pickup, K. Kalinin, A. Askitopoulos, Z. Hatzopoulos, P. G. Savvidis, N. G. Berloff, and P. G. Lagoudakis, "Optical bistability under nonresonant excitation in spinor polariton condensates", Phys. Rev. Lett. **120**, 225301 (2018).

[65]M. Klaas, O. A. Egorov, T. C. H. Liew, A. Nalitov, V. Marković, H. Suchomel, T. H. Harder, S. Betzold, E. A. Ostrovskaya, A. Kavokin, S. Klembt, S. Höfling, and C. Schneider, "Nonresonant spin selection methods and polarization control in exciton-polariton condensates", Phys. Rev. B **99**, 115303 (2019).

[66]K. G. Lagoudakis, T. Ostatnický, A. V. Kavokin, Y. G. Rubo, R. André, and B. Deveaud-Plédran, "Observation of half-quantum vortices in an exciton-polariton condensate", Science **326**, 974–976 (2009).

[67]B. König, I. A. Merkulov, D. R. Yakovlev, W. Ossau, S. M. Ryabchenko, M. Kutrowski, T. Wojtowicz, G. Karczewski, and J. Kossut, "Energy transfer from photocarriers into the magnetic ion system mediated by a two-dimensional electron gas in (Cd,Mn)Te/(Cd,Mg)Te quantum wells", Phys. Rev. B **61**, 16870–16882 (2000).

[68]A. Golnik, P. Kossacki, K. Kowalik, W. Maślana, J. Gaj, M. Kutrowski, and T. Wojtowicz, "Microphotoluminescence study of local temperature fluctuations in n-type (Cd,Mn)Te quantum well", Solid State Communications **131**, 283–288 (2004).

[69]R. Mirek, "Nierównowagowy kondensat polarytonów ekscytonowych w obecności zewnętrznego pola magnetycznego", MA thesis (University of Warsaw, Warsaw, Poland, 2017).

[70]W. H. Meiklejohn and C. P. Bean, "New magnetic anisotropy", Phys. Rev. **102**, 1413–1414 (1956).

[71]W. Szuszkiewicz, B. Hennion, M. Jouanne, J. Morhange, E. Dynowska, E. Janik, and T. Wojtowicz, "Selected properties of AFM-III structures — cubic MnTe and diluted magnetic semiconductors: CdMnTe and MgMnTe", Journal of Magnetism and Magnetic Materials **196-197**, 425–427 (1999).

[72]L. S. Dang, D. Heger, R. André, F. Bœuf, and R. Romestain, "Stimulation of polariton photoluminescence in semiconductor microcavity", Phys. Rev. Lett. **81**, 3920–3923 (1998).

[73]E. Estrecho, T. Gao, N. Bobrovska, D. Comber-Todd, M. D. Fraser, M. Steger, K. West, L. N. Pfeiffer, J. Levinsen, M. M. Parish, T. C. H. Liew, M. Matuszewski, D. W. Snoke, A. G. Truscott, and E. A. Ostrovskaya, "Direct measurement of polariton-polariton interaction strength in the thomas-fermi regime of exciton-polariton condensation", Phys. Rev. B **100**, 035306 (2019).

[74]M. Pieczarka, O. Bleu, E. Estrecho, M. Wurdack, M. Steger, D. W. Snoke, K. West, L. N. Pfeiffer, A. G. Truscott, E. A. Ostrovskaya, J. Levinsen, and M. M. Parish, "Bogoliubov excitations of a polariton condensate in dynamical equilibrium with an incoherent reservoir", Phys. Rev. B **105**, 224515 (2022).

[75]J. Kasprzak, M. Richard, A. Baas, B. Deveaud, R. André, J.-P. Poizat, and L. S. Dang, "Second-order time correlations within a polariton Bose-Einstein condensate in a cdte microcavity", Phys. Rev. Lett. **100**, 067402 (2008).

[76]E. G. Loewen, M. Nevière, and D. Maystre, "Grating efficiency theory as it applies to blazed and holographic gratings", Applied Optics **16**, 2711 (1977).

[77]M. Martinelli, "Time reversal for the polarization state in optical systems", Journal of Modern Optics **39**, 451–455 (1992).

[78]B. Guha, F. Marsault, F. Cadiz, L. Morgenroth, V. Ulin, V. Berkovitz, A. Lemaítre, C. Gomez, A. Amo, S. Combrié, B. Gérard, G. Leo, and I. Favero, "Surface-enhanced gallium arsenide photonic resonator with quality factor of 6×10^6", Optica **4**, 218 (2017).

[79]H. Suchomel, M. Klaas, S. Betzold, P. Gagel, J. Beierlein, S. Klembt, C. Schneider, and S. Höfling, "Spatio-temporal coherence in vertically emitting GaAs-based electrically driven polariton lasers", Applied Physics Letters **116**, 171103 (2020).

[80]J.-G. Rousset, J. Kobak, E. Janik, T. Jakubczyk, R. Rudniewski, P. Piotrowski, M. Ściesiek, J. Borysiuk, T. Slupinski, A. Golnik, P. Kossacki, M. Nawrocki, and W. Pacuski, "MBE grown microcavities based on selenium and tellurium compounds", Journal of Crystal Growth **401**, 499–503 (2014).

[81]G. Tosi, G. Christmann, N. G. Berloff, P. Tsotsis, T. Gao, Z. Hatzopoulos, P. G. Savvidis, and J. J. Baumberg, "Sculpting oscillators with light within a nonlinear quantum fluid", Nature Physics **8**, 190–194 (2012).

[82]M. Aßmann, F. Veit, M. Bayer, A. Löffler, S. Höfling, M. Kamp, and A. Forchel, "All-optical control of quantized momenta on a polariton staircase", Phys. Rev. B **85**, 155320 (2012).

[83]D. Sanvitto, A. Amo, D. Ballarini, M. D. Martin, L. Vinã, D. Solnyshkov, G. Malpuech, R. André, M. Caldas, and N. Studart, "Effects of disorder on the polariton condensates in CdTe microcavities", in AIP conference proceedings (2010).

[84]F. Manni, K. G. Lagoudakis, R. André, M. Wouters, and B. Deveaud, "Penrose-onsager criterion validation in a one-dimensional polariton condensate", Phys. Rev. Lett. **109**, 150409 (2012).

[85]K. G. Lagoudakis, B. Piętka, M. Wouters, R. André, and B. Deveaud-Plédran, "Coherent oscillations in an exciton-polariton Josephson junction", Phys. Rev. Lett. **105**, 120403 (2010).

[86]M. Abbarchi, A. Amo, V. G. Sala, D. D. Solnyshkov, H. Flayac, L. Ferrier, I. Sagnes, E. Galopin, A. Lemaítre, G. Malpuech, and J. Bloch, "Macroscopic quantum self-trapping and Josephson oscillations of exciton polaritons", Nature Physics **9**, 275–279 (2013).

[87]S. R. K. Rodriguez, A. Amo, I. Sagnes, L. L. Gratiet, E. Galopin, A. Lemaítre, and J. Bloch, "Interaction-induced hopping phase in driven-dissipative coupled photonic microcavities", Nature Communications **7**, 10.1038/ncomms11887 (2016).

[88]S. Alyatkin, J. D. Töpfer, A. Askitopoulos, H. Sigurdsson, and P. G. Lagoudakis, "Optical control of couplings in polariton condensate lattices", Phys. Rev. Lett. **124**, 207402 (2020).

[89]L. Pickup, J. D. Töpfer, H. Sigurdsson, and P. G. Lagoudakis, "Polariton spin jets through optical control", Phys. Rev. B **103**, 155302 (2021).

[90]D. Sanvitto, F. M. Marchetti, M. H. Szymańska, G. Tosi, M. Baudisch, F. P. Laussy, D. N. Krizhanovskii, M. S. Skolnick, L. Marrucci, A. Lemaître, J. Bloch, C. Tejedor, and L. Viña, "Persistent currents and quantized vortices in a polariton superfluid", Nature Physics **6**, 527–533 (2010).

[91]C. Antón, T. C. H. Liew, J. Cuadra, M. D. Martín, P. S. Eldridge, Z. Hatzopoulos, G. Stavrinidis, P. G. Savvidis, and L. Viña, "Quantum reflections and shunting of polariton condensate wave trains: implementation of a logic and gate", Phys. Rev. B **88**, 245307 (2013).

[92]T. Gao, P. S. Eldridge, T. C. H. Liew, S. I. Tsintzos, G. Stavrinidis, G. Deligeorgis, Z. Hatzopoulos, and P. G. Savvidis, "Polariton condensate transistor switch", Phys. Rev. B **85**, 235102 (2012).

[93]E. Wertz, L. Ferrier, D. D. Solnyshkov, R. Johne, D. Sanvitto, A. Lemaître, I. Sagnes, R. Grousson, A. V. Kavokin, P. Senellart, G. Malpuech, and J. Bloch, "Spontaneous formation and optical manipulation of extended polariton condensates", Nature Physics **6**, 860–864 (2010).

[94]H. Ohadi, Y. del Valle-Inclan Redondo, A. Dreismann, Y. G. Rubo, F. Pinsker, S. I. Tsintzos, Z. Hatzopoulos, P. G. Savvidis, and J. J. Baumberg, "Tunable magnetic alignment between trapped exciton-polariton condensates", Phys. Rev. Lett. **116**, 106403 (2016).

[95]H. Ohadi, A. J. Ramsay, H. Sigurdsson, Y. del Valle-Inclan Redondo, S. I. Tsintzos, Z. Hatzopoulos, T. C. H. Liew, I. A. Shelykh, Y. G. Rubo, P. G. Savvidis, and J. J. Baumberg, "Spin order and phase transitions in chains of polariton condensates", Phys. Rev. Lett. **119**, 067401 (2017).

[96]J. D. Töpfer, H. Sigurdsson, L. Pickup, and P. G. Lagoudakis, "Time-delay polaritonics", Communications Physics **3**, 10.1038/s42005-019-0271-0 (2020).

[97]C. Huang, V. J. Sorger, M. Miscuglio, M. Al-Qadasi, A. Mukherjee, L. Lampe, M. Nichols, A. N. Tait, T. F. de Lima, B. A. Marquez, J. Wang, L. Chrostowski, M. P. Fok, D. Brunner, S. Fan, S. Shekhar, P. R. Prucnal, and B. J. Shastri, "Prospects and applications of photonic neural networks", Advances in Physics: X **7**, 1981155 (2022).

[98]J. Bloch, F. Boeuf, J. Gérard, B. Legrand, J. Marzin, R. Planel, V. Thierry-Mieg, and E. Costard, "Strong and weak coupling regime in pillar semiconductor microcavities", Physica E: Low-dimensional Systems and Nanostructures **2**, 915–919 (1998).

[99]G. Dasbach, M. Schwab, M. Bayer, and A. Forchel, "Parametric polariton scattering in microresonators with three-dimensional optical confinement", Physical Review B **64**, 10.1103/physrevb.64.201309 (2001).

[100]D. Bajoni, P. Senellart, E. Wertz, I. Sagnes, A. Miard, A. Lemaître, and J. Bloch, "Polariton laser using single micropillar GaAs−GaAlAs semiconductor cavities", Phys. Rev. Lett. **100**, 047401 (2008).

[101]M. Klaas, H. Flayac, M. Amthor, I. G. Savenko, S. Brodbeck, T. Ala-Nissila, S. Klembt, C. Schneider, and S. Höfling, "Evolution of temporal coherence in confined exciton-polariton condensates", Phys. Rev. Lett. **120**, 017401 (2018).

[102]H. Suchomel, S. Klembt, T. H. Harder, M. Klaas, O. A. Egorov, K. Winkler, M. Emmerling, R. Thomale, S. Höfling, and C. Schneider, "Platform for electrically pumped polariton simulators and topological lasers", Phys. Rev. Lett. **121**, 257402 (2018).

[103]S. Klembt, T. H. Harder, O. A. Egorov, K. Winkler, R. Ge, M. A. Bandres, M. Emmerling, L. Worschech, T. C. H. Liew, M. Segev, C. Schneider, and S. Höfling, "Exciton-polariton topological insulator", Nature **562**, 552–556 (2018).

[104]A. Amo, J. Lefrère, S. Pigeon, C. Adrados, C. Ciuti, I. Carusotto, R. Houdré, E. Giacobino, and A. Bramati, "Superfluidity of polaritons in semiconductor microcavities", Nature Physics **5**, 805–810 (2009).

[105]A. Amo, D. Sanvitto, F. P. Laussy, D. Ballarini, E. del Valle, M. D. Martin, A. Lemaître, J. Bloch, D. N. Krizhanovskii, M. S. Skolnick, C. Tejedor, and L. Viña, "Collective fluid dynamics of a polariton condensate in a semiconductor microcavity", Nature **457**, 291–295 (2009).

[106]K. G. Lagoudakis, M. Wouters, M. Richard, A. Baas, I. Carusotto, R. André, L. S. Dang, and B. Deveaud-Plédran, "Quantized vortices in an exciton–polariton condensate", Nature Physics **4**, 706–710 (2008).

[107]G. Roumpos, M. D. Fraser, A. Löffler, S. Höfling, A. Forchel, and Y. Yamamoto, "Single vortex–antivortex pair in an exciton-polariton condensate", Nature Physics **7**, 129–133 (2010).

[108]Y. G. Rubo, "Half vortices in exciton polariton condensates", Phys. Rev. Lett. **99**, 106401 (2007).

[109]F. Manni, K. G. Lagoudakis, T. C. H. Liew, R. André, V. Savona, and B. Deveaud, "Dissociation dynamics of singly charged vortices into half-quantum vortex pairs", Nature Communications **3**, 10.1038/ncomms2310 (2012).

[110]L. Dominici, G. Dagvadorj, J. M. Fellows, D. Ballarini, M. D. Giorgi, F. M. Marchetti, B. Piccirillo, L. Marrucci, A. Bramati, G. Gigli, M. H. Szymańska, and D. Sanvitto, "Vortex and half-vortex dynamics in a nonlinear spinor quantum fluid", Science Advances **1**, 10.1126/sciadv.1500807 (2015).

[111]E. L. Bolda and D. F. Walls, "Detection of vorticity in Bose-Einstein condensed gases by matter-wave interference", Phys. Rev. Lett. **81**, 5477–5480 (1998).

[112]M. Matuszewski, A. Opala, R. Mirek, M. Furman, M. Król, K. Tyszka, T. Liew, D. Ballarini, D. Sanvitto, J. Szczytko, and B. Piętka, "Energy-efficient neural network inference with microcavity exciton polaritons", Physical Review Applied **16**, 10.1103/physrevapplied.16.024045 (2021).

[113]Á. Cuevas, J. C. L. Carreño, B. Silva, M. D. Giorgi, D. G. Suárez-Forero, C. S. Muñoz, A. Fieramosca, F. Cardano, L. Marrucci, V. Tasco, G. Biasiol, E. del Valle, L. Dominici, D. Ballarini, G. Gigli, P. Mataloni, F. P. Laussy, F. Sciarrino, and D. Sanvitto, "First observation of the quantized exciton-polariton field and effect of interactions on a single polariton", Science Advances **4**, 10.1126/sciadv.aao6814 (2018).

[114]T. Kuriakose, P. M. Walker, T. Dowling, O. Kyriienko, I. A. Shelykh, P. St-Jean, N. C. Zambon, A. Lemaítre, I. Sagnes, L. Legratiet, A. Harouri, S. Ravets, M. S. Skolnick, A. Amo, J. Bloch, and D. N. Krizhanovskii, "Few-photon all-optical phase rotation in a quantum-well micropillar cavity", Nature Photonics **16**, 566–569 (2022).

[115]P. G. Lagoudakis and N. G. Berloff, "A polariton graph simulator", New Journal of Physics **19**, 125008 (2017).

[116]H. Ohadi, R. L. Gregory, T. Freegarde, Y. G. Rubo, A. V. Kavokin, N. G. Berloff, and P. G. Lagoudakis, "Nontrivial phase coupling in polariton multiplets", Phys. Rev. X **6**, 031032 (2016).

[117]I. Y. Chestnov, A. V. Kavokin, and A. V. Yulin, "The optical control of phase locking of polariton condensates", New Journal of Physics **21**, 113009 (2019).

[118]A. Baas, J. P. Karr, H. Eleuch, and E. Giacobino, "Optical bistability in semiconductor microcavities", Physical Review A **69**, 023809 (2004).

[119]D. Bajoni, E. Semenova, A. Lemaître, S. Bouchoule, E. Wertz, P. Senellart, S. Barbay, R. Kuszelewicz, and J. Bloch, "Optical bistability in a GaAs-based polariton diode", Physical review letters **101**, 266402 (2008).

[120]C. Antón, T. C. H. Liew, G. Tosi, M. D. Martin, T. Gao, Z. Hatzopoulos, P. S. Eldridge, P. G. Savvidis, and L. Viña, "Dynamics of a polariton condensate transistor switch", Applied Physics Letters **101**, 261116 (2012).

[121]J. Feng, J. Wang, A. Fieramosca, R. Bao, J. Zhao, R. Su, Y. Peng, T. C. H. Liew, D. Sanvitto, and Q. Xiong, "All-optical switching based on interacting exciton polaritons in self-assembled perovskite microwires", Science Advances **7**, 10.1126/sciadv.abj6627 (2021).

[122]A. V. Zasedatelev, A. V. Baranikov, D. Sannikov, D. Urbonas, F. Scafirimuto, V. Y. Shishkov, E. S. Andrianov, Y. E. Lozovik, U. Scherf, T. Stöferle, R. F. Mahrt, and P. G. Lagoudakis, "Single-photon nonlinearity at room temperature", Nature **597**, 493–497 (2021).

[123]D. G. Suárez-Forero, F. Riminucci, V. Ardizzone, A. Gianfrate, F. Todisco, M. De Giorgi, D. Ballarini, G. Gigli, K. Baldwin, L. Pfeiffer, and D. Sanvitto, *Ultrafast, low-energy, all-optical switch in polariton waveguides*, 2021.

[124]F. Chen, H. Li, H. Zhou, S. Luo, Z. Sun, Z. Ye, F. Sun, J. Wang, Y. Zheng, X. Chen, H. Xu, H. Xu, T. Byrnes, Z. Chen, and J. Wu, "Optically controlled femtosecond polariton switch at room temperature", Phys. Rev. Lett. **129**, 057402 (2022).

[125]A. Schiffrin, T. Paasch-Colberg, N. Karpowicz, V. Apalkov, D. Gerster, S. Mühlbrandt, M. Korbman, J. Reichert, M. Schultze, S. Holzner, J. V. Barth, R. Kienberger, R. Ernstorfer, V. S. Yakovlev, M. I. Stockman, and F. Krausz, "Optical-field-induced current in dielectrics", Nature **493**, 70–74 (2012).

[126]K. Tyszka, M. Furman, R. Mirek, M. Król, A. Opala, B. Seredyński, J. Suffczyński, W. Pacuski, M. Matuszewski, J. Szczytko, and B. Piętka, "Leaky integrate-and-fire mechanism in exciton-polariton condensates for photonic spiking neurons", Laser & Photonics Reviews, 2100660 (2022).

[127]D. Brunner and D. Psaltis, "Competitive photonic neural networks", Nature Photonics **15**, 323–324 (2021).

[128]Y. Shen, N. C. Harris, S. Skirlo, M. Prabhu, T. Baehr-Jones, M. Hochberg, X. Sun, S. Zhao, H. Larochelle, D. Englund, and M. Soljacic, "Deep learning with coherent nanophotonic circuits", Nature Photonics **11**, 441–446 (2017).

[129]X. Lin, Y. Rivenson, N. T. Yardimci, M. Veli, Y. Luo, M. Jarrahi, and A. Ozcan, "All-optical machine learning using diffractive deep neural networks", Science **361**, 1004–1008 (2018).

[130]A. N. Tait, M. A. Nahmias, B. J. Shastri, and P. R. Prucnal, "Broadcast and weight: an integrated network for scalable photonic spike processing", J. Lightwave Technol. **32**, 3427–3439 (2014).

[131]P. Antonik, N. Marsal, D. Brunner, and D. Rontani, "Human action recognition with a large-scale brain-inspired photonic computer", Nature Machine Intelligence **1**, 530–537 (2019).

[132]G. Wetzstein, A. Ozcan, S. Gigan, S. Fan, D. Englund, M. Soljačić, C. Denz, D. A. Miller, and D. Psaltis, "Inference in artificial intelligence with deep optics and photonics", Nature **588**, 39–47 (2020).

[133]B. J. Shastri, A. N. Tait, T. F. de Lima, W. H. Pernice, H. Bhaskaran, C. D. Wright, and P. R. Prucnal, "Photonics for artificial intelligence and neuromorphic computing", Nature Photonics **15**, 102–114 (2021).

[134]X. Xu, M. Tan, B. Corcoran, J. Wu, A. Boes, T. G. Nguyen, S. T. Chu, B. E. Little, D. G. Hicks, R. Morandotti, A. Mitchell, and D. J. Moss, "11 TOPS photonic convolutional accelerator for optical neural networks", Nature **589**, 44–51 (2021).

[135]T. Wang, S.-Y. Ma, L. G. Wright, T. Onodera, B. C. Richard, and P. L. McMahon, "An optical neural network using less than 1 photon per multiplication", Nature Communications **13**, 123 (2022).

[136]A. Delteil, T. Fink, A. Schade, S. Höfling, C. Schneider, and A. Imamoglu, "Towards polariton blockade of confined exciton-polaritons", Nature Materials **18**, 219–222 (2019).

[137]A. Dreismann, H. Ohadi, Y. del Valle-Inclan Redondo, R. Balili, Y. G. Rubo, S. I. Tsintzos, G. Deligeorgis, Z. Hatzopoulos, P. G. Savvidis, and J. J. Baumberg, "A sub-femtojoule electrical spin-switch based on optically trapped polariton condensates", Nature Materials **15**, 1074–1078 (2016).

[138]D. Ballarini, M. D. Giorgi, E. Cancellieri, R. Houdré, E. Giacobino, R. Cingolani, A. Bramati, G. Gigli, and D. Sanvitto, "All-optical polariton transistor", Nature Communications **4**, 1778 (2013).

[139]A. V. Zasedatelev, A. V. Baranikov, D. Urbonas, F. Scafirimuto, U. Scherf, T. Stöferle, R. F. Mahrt, and P. G. Lagoudakis, "A room-temperature organic polariton transistor", Nature Photonics **13**, 378–383 (2019).

[140]H. Xu, S. Ghosh, M. Matuszewski, and T. C. Liew, "Universal self-correcting computing with disordered exciton-polariton neural networks", Phys. Rev. Applied **13**, 064074 (2020).

[141]D. Ballarini, A. Gianfrate, R. Panico, A. Opala, S. Ghosh, L. Dominici, V. Ardizzone, M. De Giorgi, G. Lerario, G. Gigli, T. C. H. Liew, M. Matuszewski, and D. Sanvitto, "Polaritonic neuromorphic computing outperforms linear classifiers", Nano Letters **20**, 3506–3512 (2020).

[142]A. Opala, R. Panico, V. Ardizzone, B. Pi ętka, J. Szczytko, D. Sanvitto, M. Matuszewski, and D. Ballarini, "Training a neural network with exciton-polariton optical nonlinearity", Phys. Rev. Applied **18**, 024028 (2022).

[143]Q. Liu, Z. Ouyang, C. J. Wu, C. P. Liu, and J. C. Wang, "All-optical half adder based on cross structures in two-dimensional photonic crystals", Optics Express **16**, 18992 (2008).

[144]Y. Ishizaka, Y. Kawaguchi, K. Saitoh, and M. Koshiba, "Design of ultra compact all-optical XOR and AND logic gates with low power consumption", Optics Communications **284**, 3528–3533 (2011).

[145]G. Filho, D. Correia, W. de Fraga, and G. Guimarães, "Obtaining optical logic gates – OR, XOR, AND and logic functions using asymmetric mach-zehnder interferometer based on photonic crystal fiber", Optics & Laser Technology **97**, 370–378 (2017).

[146]J. Xie, X. Niu, X. Hu, F. Wang, Z. Chai, H. Yang, and Q. Gong, "Ultracompact all-optical full-adder and half-adder based on nonlinear plasmonic nanocavities", Nanophotonics **6**, 1161–1173 (2017).

[147]H. J. Caulfield and S. Dolev, "Why future supercomputing requires optics", Nature Photonics **4**, 261–263 (2010).

[148]Y. LeCun, L. Bottou, Y. Bengio, and P. Haffner, "Gradient-based learning applied to document recognition", Proceedings of the IEEE **86**, 2278–2324 (1998).

[149]M. Abadi, P. Barham, J. Chen, Z. Chen, A. Davis, J. Dean, M. Devin, S. Ghemawat, G. Irving, M. Isard, M. Kudlur, J. Levenberg, R. Monga, S. Moore, D. G. Murray, B. Steiner, P. Tucker, V. Vasudevan, P. Warden, M. Wicke, Y. Yu, and X. Zheng, "Tensorflow: a system for large-scale machine learning", in 12th USENIX symposium on operating systems design and implementation (OSDI 16) (Nov. 2016), pp. 265–283.

[150]T. Chen, J. van Gelder, B. van de Ven, S. V. Amitonov, B. de Wilde, H.-C. Ruiz Euler, H. Broersma, P. A. Bobbert, F. A. Zwanenburg, and W. G. van der Wiel, "Classification with a disordered dopant-atom network in silicon", Nature **577**, 341–345 (2020).

[151]P. Yao, H. Wu, B. Gao, J. Tang, Q. Zhang, W. Zhang, J. J. Yang, and H. Qian, "Fully hardware-implemented memristor convolutional neural network", Nature **577**, 641–646 (2020).

[152]C. Du, F. Cai, M. A. Zidan, W. Ma, S. H. Lee, and W. D. Lu, "Reservoir computing using dynamic memristors for temporal information processing", Nature Communications **8**, 2204 (2017).

[153]D. Brunner, M. C. Soriano, C. R. Mirasso, and I. Fischer, "Parallel photonic information processing at gigabyte per second data rates using transient states", Nature Communications **4**, 1364 (2013).

[154]K. Vandoorne, P. Mechet, T. Van Vaerenbergh, M. Fiers, G. Morthier, D. Verstraeten, B. Schrauwen, J. Dambre, and P. Bienstman, "Experimental demonstration of reservoir computing on a silicon photonics chip", Nature Communications **5**, 3541 (2014).

[155]J. Torrejon, M. Riou, F. A. Araujo, S. Tsunegi, G. Khalsa, D. Querlioz, P. Bortolotti, V. Cros, K. Yakushiji, A. Fukushima, H. Kubota, S. Yuasa, M. D. Stiles, and J. Grollier, "Neuromorphic computing with nanoscale spintronic oscillators", Nature **547**, 428–431 (2017).

[156]T. Chen, Z. Du, N. Sun, J. Wang, C. Wu, Y. Chen, and O. Temam, "Diannao: a small-footprint high-throughput accelerator for ubiquitous machine-learning", in Proceedings of the 19th international conference on architectural support for programming languages and operating systems, ASPLOS '14 (2014), pp. 269–284.

[157]H. Komkov, A. Restelli, B. Hunt, L. Shaughnessy, I. Shani, and D. P. Lathrop, "The Recurrent Processing Unit: Hardware for High Speed Machine Learning", arXiv:1912.07363, 1912.07363. *arXiv*. http://arxiv.org/abs/1912.07363 (accessed February 22, 2021) (2019).

[158]J. Lee, C. Kim, S. Kang, D. Shin, S. Kim, and H. Yoo, "Unpu: an energy-efficient deep neural network accelerator with fully variable weight bit precision", IEEE Journal of Solid-State Circuits **54**, 173–185 (2019).

[159]C. Farabet, B. Martini, B. Corda, P. Akselrod, E. Culurciello, and Y. LeCun, "Neuflow: a runtime reconfigurable dataflow processor for vision", in Cvpr 2011 workshops (June 2011), pp. 109–116.

[160]L. Appeltant, M. Soriano, G. Van der Sande, J. Danckaert, S. Massar, J. Dambre, B. Schrauwen, C. Mirasso, and I. Fischer, "Information processing using a single dynamical node as complex system", Nat. Commun. **2**, 468 (2011).

[161]D. Brunner, M. C. Soriano, C. R. Mirasso, and I. Fischer, "Parallel photonic information processing at gigabyte per second data rates using transient states", Nat. Commun. **4**, 1364 (2013).

[162]J. Robertson, M. Hejda, J. Bueno, and A. Hurtado, "Ultrafast optical integration and pattern classification for neuromorphic photonics based on spiking VCSEL neurons", Sci. Rep. **10**, 6098 (2020).

[163]M. Liberman, R. Amsler, K. Church, E. Fox, C. Hafner, J. Klavans, M. Marcus, B. Mercer, J. Pedersen, P. Roossin, D. Walker, S. Warwick, and A. Zampolli, *TI 46-Word*, `https://catalog.ldc.upenn.edu/LDC93S9`, 1993.

[164]R. Su, C. Diederichs, J. Wang, T. C. H. Liew, J. Zhao, S. Liu, W. Xu, Z. Chen, and Q. Xiong, "Room-temperature polariton lasing in all-inorganic perovskite nanoplatelets", Nano Letters **17**, 3982–3988 (2017).

[165]J. D. Plumhof, T. Stöferle, L. Mai, U. Scherf, and R. F. Mahrt, "Room-temperature bose–einstein condensation of cavity exciton–polaritons in a polymer", Nature Materials **13**, 247–252 (2013).

[166]M. Dusel, S. Betzold, O. A. Egorov, S. Klembt, J. Ohmer, U. Fischer, S. Höfling, and S. C., "Room temperature organic exciton–polariton condensate in a lattice", Nature Communications **11**, 2863 (2020).

[167]T. Cookson, K. Georgiou, A. Zasedatelev, R. T. Grant, T. Virgili, M. Cavazzini, F. Galeotti, C. Clark, N. G. Berloff, D. G. Lidzey, and P. G. Lagoudakis, "A yellow polariton condensate in a dye filled microcavity", Advanced Optical Materials **5**, 1700203 (2017).

[168]J. J. Baumberg, A. V. Kavokin, S. Christopoulos, A. J. D. Grundy, R. Butté, G. Christmann, D. D. Solnyshkov, G. Malpuech, G. B. H. von Högersthal, E. Feltin, J.-F. Carlin, and N. Grandjean, "Spontaneous polarization buildup in a room-temperature polariton laser", Physical Review Letters **101**, `10.1103/physrevlett.101.136409` (2008).

[169]G. Malpuech, A. D. Carlo, A. Kavokin, J. J. Baumberg, M. Zamfirescu, and P. Lugli, "Room-temperature polariton lasers based on GaN microcavities", Applied Physics Letters **81**, 412–414 (2002).

[170]J. W. Goodman, A. R. Dias, and L. M. Woody, "Fully parallel, high-speed incoherent optical method for performing discrete Fourier transforms", Optics Letters **2**, 1 (1978).

[171]M. Gruber, J. Jahns, and S. Sinzinger, "Planar-integrated optical vector-matrix multiplier", Applied Optics **39**, 5367 (2000).

[172]J. Chang, V. Sitzmann, X. Dun, W. Heidrich, and G. Wetzstein, "Hybrid optical-electronic convolutional neural networks with optimized diffractive optics for image classification", Scientific Reports **8**, 12324 (2018).

[173]Y. Zuo, B. Li, Y. Zhao, Y. Jiang, Y.-C. Chen, P. Chen, G.-B. Jo, J. Liu, and S. Du, "All-optical neural network with nonlinear activation functions", Optica **6**, 1132–1137 (2019).

[174]J. Spall, X. Guo, T. D. Barrett, and A. I. Lvovsky, "Fully reconfigurable coherent optical vector–matrix multiplication", Optics Letters **45**, 5752 (2020).

[175]P. A. Merolla, J. V. Arthur, R. Alvarez-Icaza, A. S. Cassidy, J. Sawada, F. Akopyan, B. L. Jackson, N. Imam, C. Guo, Y. Nakamura, B. Brezzo, I. Vo, S. K. Esser, R. Appuswamy, B. Taba, A. Amir, M. D. Flickner, W. P. Risk, R. Manohar, and D. S. Modha, "A million spiking-neuron integrated circuit with a scalable communication network and interface", Science **345**, 668–673 (2014).

[176]P. Yao, H. Wu, B. Gao, J. Tang, Q. Zhang, W. Zhang, J. J. Yang, and H. Qian, "Fully hardware-implemented memristor convolutional neural network", Nature **577**, 641–646 (2020).

[177]S. Ambrogio, P. Narayanan, H. Tsai, R. M. Shelby, I. Boybat, C. di Nolfo, S. Sidler, M. Giordano, M. Bodini, N. C. P. Farinha, B. Killeen, C. Cheng, Y. Jaoudi, and G. W. Burr, "Equivalent-accuracy accelerated neural-network training using analogue memory", Nature **558**, 60–67 (2018).